The Impact of Environmental Conditions on Internal Waves and Mixing in Two Distinct Ocean Basins

Tamara Barriquand

▶ To cite this version:

HAL Id: tel-01196580
https://theses.hal.science/tel-01196580

Submitted on 10 Sep 2015

THÈSE DE DOCTORAT DE L'UNIVERSITÉ PIERRE ET MARIE CURIE

École Doctorale de Sciences de l'Environnement d'Ile de France

Spécialité
Océanographie, Météorologie et Environnement

présentée par

Tamara Beitzel Barriquand

The Impact of Environmental Conditions on Internal Waves and Mixing in Two Distinct Ocean Basins

---

Soutenue le 11 décembre 2014 devant le jury composé de :

M. Alain SALIOT	président
M. Robert PINKEL	rapporteur
M. Bruno FERRON	rapporteur
M. Thierry DAUXOIS	examinateur
Mme Caroline MULLER	examinateur
Mme Pascale BOURUET-AUBERTOT	directrice
M. Yannis CUYPERS	directeur
Mme Jennifer MACKINNON	co-directrice
M. Frédéric VIVIER	co-directeur

Laboratoire d'Océanographie et du Climat : Expérimentaions et Approches Numériques, Institut Pierre Simon Laplace (LOCEAN-IPSL)
Sorbonnes Universités, UPMC Univ. Paris 06
Paris, France

UPMC
Ecole Doctorale de Sciences
de l'Environnement d'Ile de France
4 place Jussieu
75252 Paris Cedex 05

Cette thèse est dédiée à mon fils,
This thesis is dedicated to my son,
Théodore James Barriquand.

Le mélange fait tourner le monde.
Mixing makes the world go round.

Remerciements

Remerciements

Je voudrais remercier mes directeurs de thése au LOCEAN, Pascale Bouruet-Aubertot, Yannis Cuypers, et Frédéric Viviers, pour leur soutenance pendant ses derniéres trois années. Je voudrais aussi remercier les membres de mon comité de thése, Gilles Reverdin, Ilker Fer, Theo Gerkema, Jennifer MacKinnon, et Bruno Ferron. Et mon jury, Alain Sabiot, Rob Pinkel, Thierry Dauxios, et Caroline Muller. Je voudrais remercier aussi mes collégues au LOCEAN, particuliérement mes comrades de bureau, Ivia, Simon, Gaelle, Pierre, Ramiro, Anna, Adéle, Nico, Zoe, Laurent, et Thomas.

Je veux remercier aussi mon mari et meilleure ami, Joanny, pour tout sa soutenance et compréhension pendant ce longue processus.

Acknowledgments

I would like to thank my advisor and mentor, Jennifer MacKinnon, for all her advice, both scientific and in life. I'd also like to thank Rob Pinkel for all his guidance and advice. I'd like to thank my professors, Clint Winant, Myrl Henderschott, Lynne Talley, Dan Rudnick, Sarah Gille, Ken Melville, and Bill Kuperman. I'd also like to thank all my colleagues at Scripps Institution of Oceanography for all their continued support through this long process, particularly, Jessica Kleiss, Tyler Helble, Stephanie Fried, Gordy Stephenson, Guangming Zheng, Kauchik Srinivasan, Aneesh Subramanian, Ben Reineman, Anais Orsi, Peter Sutherland, and Tara Sayuri.

I'd also like to thank my family for all their help and support. I'd like to thank my elementary school teacher and friend, Sharon Grant, who pushed and encouraged me to do the best at everything I did. I'd also like to thank my college professors at Colorado College, Val Veirs, Barbara Whitten, and Dick Hilt, whose continued support has been so important to me over the years. I'd like to thank my friends and colleagues in the Air Force who supported and encouraged me through the accident and my recovery. I'd also like to thank my friends and colleagues at Quisqueya Christian School in Port-au-Prince, Haiti, for their continued love and support.

Résumé

Résumé

Les ondes internes sont omniprésentes dans les océans. Cette thèse analyse le cycle de vie des ondes internes et l'impact du déferlement de ces ondes sur le mélange turbulent dans deux bassins océaniques, aux caractéristiques contrastées, l'Arctique et l'Indien. Ces deux régions sont en effet aux antipodes de la circulation thermohaline avec l'océan Arctique lieu de formations d'eaux denses et l'Océan Indien région d'upwelling d'eaux denses. L'analyse de données de mouillage recueillies dans le Sud-Ouest de l'Océan Indien au niveau d'une dorsale océanique révèlent la présence d'une forte marée interne. Cette marée interne montre une focalisation de l'énergie sous forme de 'rayons' dont la propagation est fortement influencée par les structures de méso-échelle. Malgré ce fort signal de marée interne, nous mettons en évidence la contribution majeure des ondes internes de fréquence proche-inertielle au mélange turbulent. Aux hautes latitudes l'analyse des séries temporelles recueillies au cours de trois printemps consécutifs dans le Storfjord, un fjord Arctique dans l'archipel Svalbard, montre la forte variabilité des ondes en fonction de la stratification et par conséquent un impact variable de ces ondes en terme de mélange turbulent. Les flux de chaleur diffusifs induits par le déferlement de ces ondes sont enfin estimés dans ces deux régions, permettant ainsi de replacer ces résultats dans le contexte global de la circulation thermohaline.

Mots-clefs

ondes internes, mélange, turbulence, stratification, topographie rugueuse

The Impact of Environmental Conditions on Internal Waves and Mixing in Two Distinct Ocean Basins

Abstract

Internal waves are ubiquitous in the ocean, and play a key role in the global overturning circulation. This thesis analyzes the life cycle of internal waves in two distinct ocean basins: the Arctic and Indian Oceans. Hydrographic and velocity data are used to study the generation, propagation, and dissipation of internal waves in these two ocean basins. In the Indian Ocean, an area of mixing-driven upwelling, mooring data reveal the presence of a strong internal tide propagating as tidal beams above the Southwest Indian Ridge in the Indian Ocean basin. These tidal beams show a strong vertical structure, and their path of propagation is highly dependent on the mesoscale activity in the region. Despite this strong internal tide signal, however, mixing in the region is dominated by inertial internal waves. On the other side of the globe, in a region of deep water formation, shipboard data from four short time series from three consecutive springs in Storfjorden, an Arctic fjord in the Svalbard Archipelago, reveal a link between the vertical structure of the stratification profile and mixing in the Arctic. These environmental conditions, the changing mesoscale in the Indian Ocean, and the changing stratification in the Arctic Ocean, greatly impact the generation, propagation, and dissipation of internal waves, and subsequent turbulent mixing in theses two ocean basins.

Keywords

Table des matières

Introduction

The Meridional Overturning Circulation (MOC) transports water, heat, and salt around the globe, and thus plays a key role in controlling the earth's climate (Figures 1 and 2). This large-scale deep overturning circulation can only be maintained, according to Sandstrom's Theorem (Sandstrom, 1908), if the heat source is beneath the cold source, or, in the case of the oceans, warm water must be at a lower geopotential height relative to the colder waters (Figure 3). The warm tropical waters of the Earth, however, are at an equal if not greater geopotential height than the colder polar waters, and, according to Sandstrom (1908), could only drive a surface circulation, not the deep overturning circulation that we in fact observe. One way to get the large-scale overturning circulation that is observed in the earth's oceans, is through wind-driven upwelling, but this by itself is insufficient (Kuhlbrodt et al., 2007). To obtain this deep abyssal density distribution, the warm surface waters must be transported to a lower geopotential height, which, as pointed out by Jeffreys (1925), can be accomplished through turbulent mixing, which advects surface waters lower in the water column. Turbulent mixing, therefore, is a key component in maintaining the global overturning circulation, and is thus a key player in the global climate system. The role of turbulent mixing, along with that of wind-driven upwelling in the Southern Ocean, in maintaining the Meridional Overturning Circulation, are illustrated in Figure 2.

According to Munk & Wunsch (1998), and Wunsch & Ferrari (2004), 1-2 TW of energy are required to maintain the abyssal density distribution. The required energy must come from some source of external mechanical energy input to the oceans. While there exist multiple possible sources of mechanical energy, the only mechanical energy sources great enough to result in enough mixing to drive the MOC are the winds, which provide 0.3-1.5 TW, and the tides, which provide 0.7-1.3 TW of mechanical power input to the ocean (i.e. Waterhouse et al., 2014; D'Asaro, 1985, 1995; Watanabe & Hibiya, 2002; Alford, 2003a; Jiang et al., 2005; Furuichi et al., 2008; Munk & Wunsch, 1998). While the winds and tides may provide enough mechanical energy, the scale of mechanical energy required for this mixing is micro-scale turbulent overturns (on the order of 1 - 10mm), and the scale of the winds and tides is far too large (on the order of 100-1000 km) for these micro-scale processes. The only way to arrive at the micro-scale energy necessary to mix the oceans is for the energy to cascade from the large-scale winds and tides to the micro-scale turbulence that mixes the ocean. The intermediary between the large-scale winds and tides and the small-scale turbulence is internal waves, which are ubiquitous throughout the ocean (Garrett & Munk, 1979).

Internal waves are waves that oscillate between different density surfaces in the ocean. The frequency at which they oscillate ranges between the inertial ($f = 2\Omega \sin latitude$) and the Brunt-Vaisala, or buoyancy, frequency, $N^2 = -g/\rho_0 \frac{d\rho}{dz}$, and is determined by their generating source. When the tide advects a stratified water column above the bottom topography, for example, it generates internal waves that oscillate at the tidal frequency, or, the "internal tide." Internal tide generation occurs anywhere the tide interacts with the ocean bottom, but is intensified in regions with topographic features such as mid-ocean
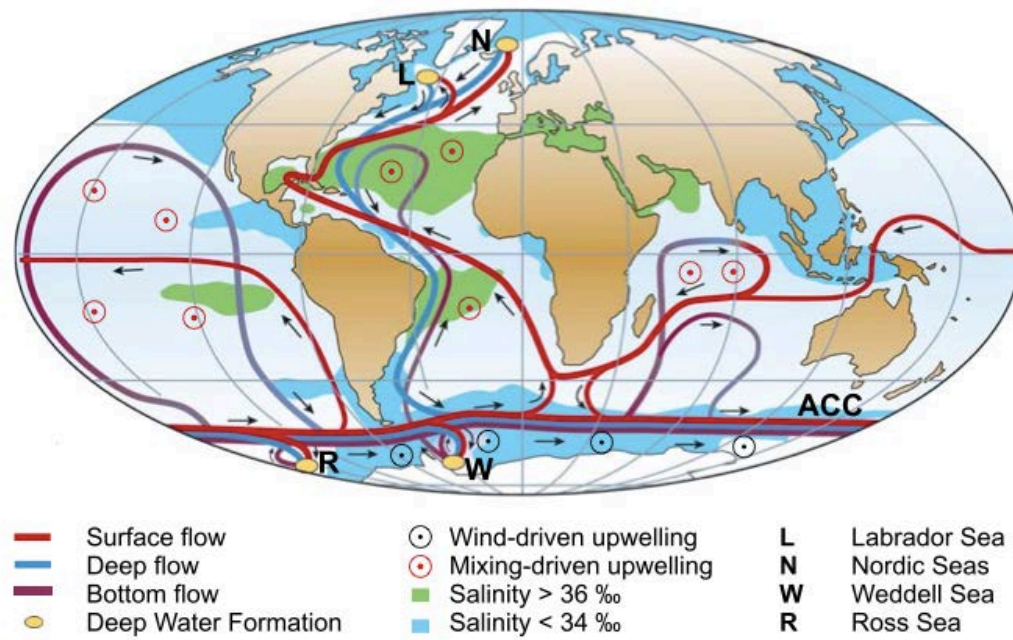
FIGURE 1 – Simplified sketch of the Meridional Overturning Circulation from Kuhlbrodt et al. (2007). Note the deepwater formation in the Arctic, and the mixing-driven upwelling in the Indian Ocean.
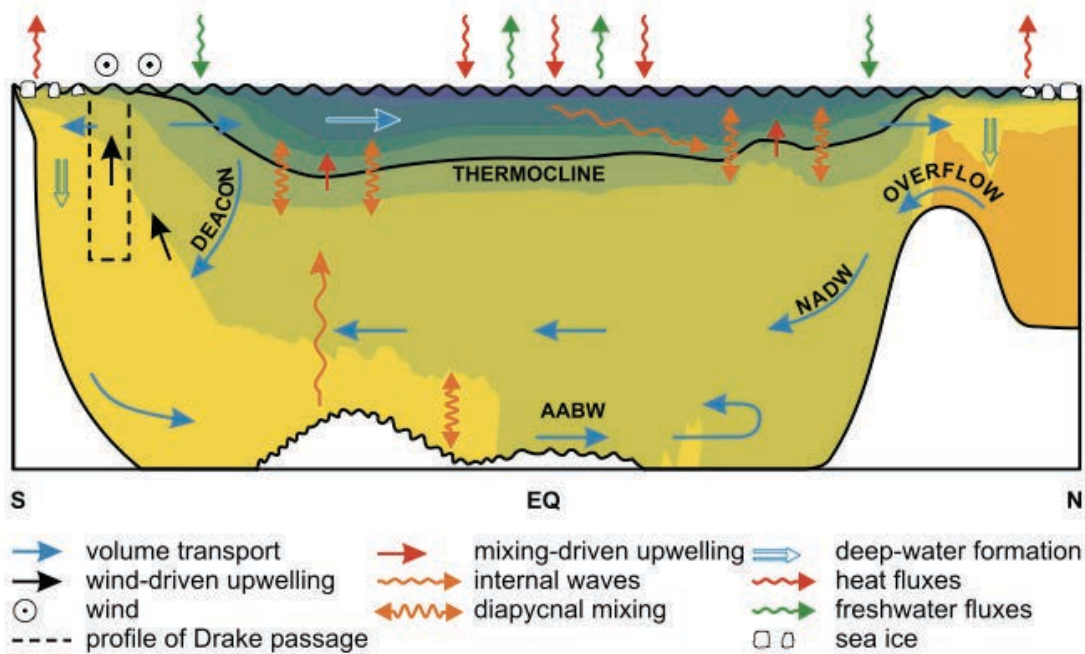
FIGURE 2 – A meridional slice of the Atlantic ocean presenting a simplified Meridional Overturning Circulation from Kuhlbrodt et al. (2007). Note the mixing-driven upwelling at mid-latitudes, and the mixing- and wind-driven upwelling and deepwater formation at high latitudes.

ridges, as can be seen in the high-resolution (2 minute) linear M_2 semidiurnal internal tide generation model in Figure 4. The linear model that created Figure 4 gives insight into regions of expected internal tide generation, but not on the propagation nor dissipation of the internal tide. To simulate the propagation of the internal tide, Simmons et al. (2004) ran a global two-layer M_2 generation simulation, whose output can be seen in Figure 5. While the model which produced the plots in Figure 5 gives insight into the propagation of the internal tide, it does not resolve (one-eighth degree resolution) the details of the small scale topography which impact internal tide generation (Melet et al., 2013), nor does it resolve the highest modes of the internal tide, which are most responsible for its dissipation.

Winds can also generate internal waves. Winds blowing on the surface of the ocean drive inertial currents in the mixed layer. The winds blow stronger in some regions than others, which leads to divergence or convergence of the inertial currents, inducing a horizontal pressure gradient, which generates internal waves at the bottom of the mixed layer. Internal waves generated by the winds propagate at the inertial, or near-inertial frequency. Near-inertial internal waves and the internal tide are the two most energetic portions of the internal wave band, and have the greatest impact on abyssal mixing. Unlike the internal tide, however, near-inertial internal waves are intermittent in space and time, as can be seen in Figure 6.

To get a better understanding of how internal waves, the conduits of mechanical energy in the oceans, impact ocean mixing, and hence ocean circulation and the global climate system, we look at internal waves in two distinct ocean basins, the Arctic and Indian Oceans (Figure 7), two regions where mixing and deep-water formation contribute to the MOC (Figure 1). The goal of studying internal waves in two very different ocean basins is to understand the effects of various environmental conditions on the life cycle of
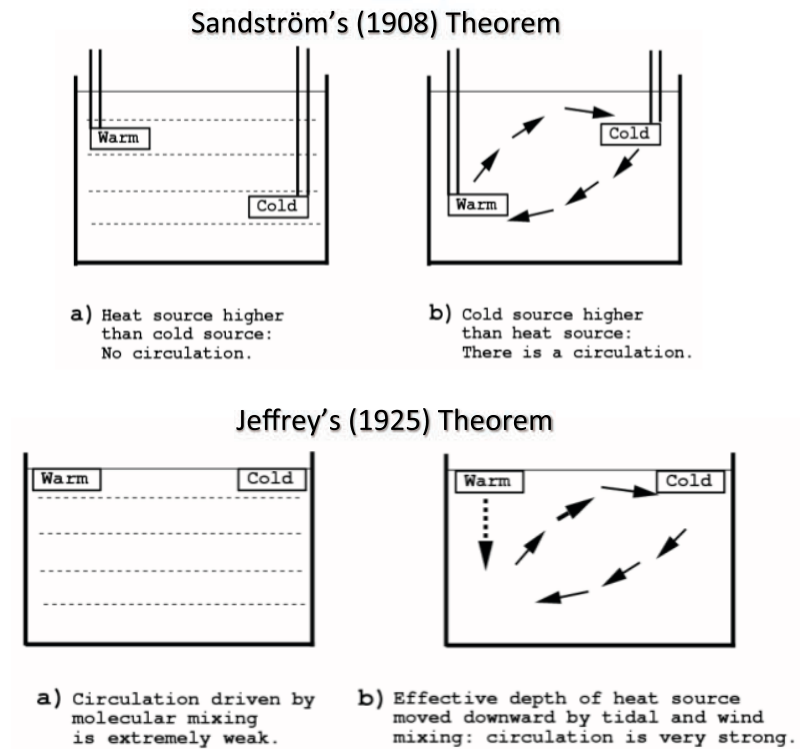
FIGURE 3 – Visual depiction of Sandstrom's Theorem (above) and Jeffreys' modification (below).
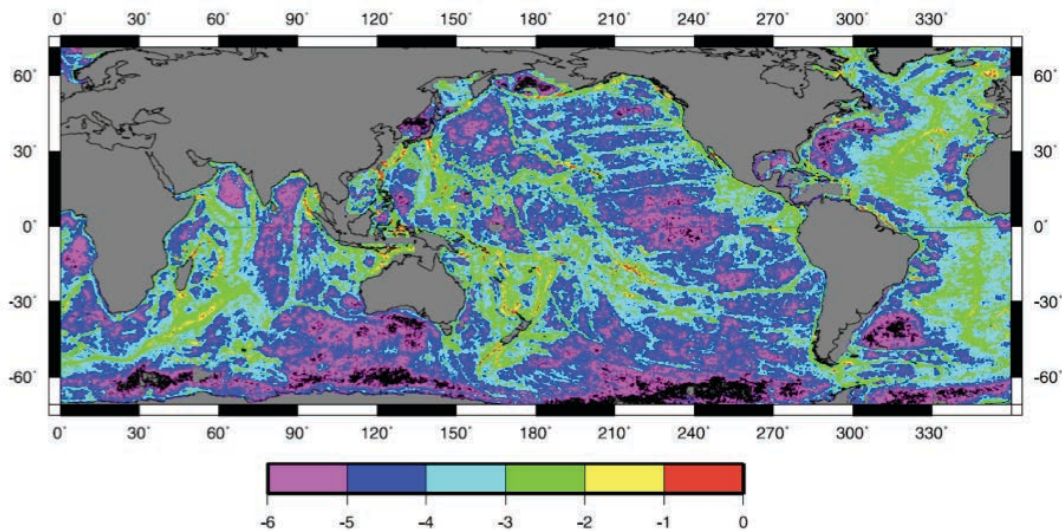
FIGURE 4 – Global energy flux (W/m^2) distribution from M_2 semidiurnal tide to internal waves from a numerical model by Nycander (2005)

the internal waves. How do different environmental conditions, such as stratification and mesoscale eddies, in the Arctic and Indian Oceans affect the generation, propagation, and dissipation of internal waves ? If we can understand the effects of varying environmental conditions on the life cycle of internal waves, we can better parameterize the mixing in large-scale models, and thus better understand their impact on the MOC and the global climate system.

While mixing occurs throughout the ocean, it is not uniform, but rather concentrated in areas of rough topography and ocean boundaries. To better understand what occurs in these areas of elevated mixing, we look at an area of rough topography where mixing, based on data acquired during the World Ocean Circulation Experiment (WOCE), was parameterized to be elevated orders of magnitude above the surroundings, extending all the way to the surface (Kunze et al., 2006). The study region is above the Southwest Indian Ridge in the Indian Ocean, where mixing-driven upwelling contributes to the MOC (Figure 1). One of the goals of studying internal waves in this region is to understand what happens when the barotropic tide interacts with the rough, corrugated topography, producing the internal tide. While there have been numerous studies of internal tide generation and propagation in areas of relatively simple topography, such as the Hawaiian Ridge (e.g. Rudnick et al., 2003; Merrifield & Holloway, 2002; Rainville & Pinkel, 2006; Nash et al., 2006; Klymak et al., 2008; Cole et al., 2009), very few studies of the internal wave field above areas of rough topography have been conducted. This study seeks to determine the effects of environmental conditions on the generation and propagation of the internal tide in regions of rough topography and elevated mixing.

In order to determine the source of the elevated mixing in this region of rough to-pography, we must look at the dissipation of the internal waves in the region. In order to determine what is responsible for this elevated turbulence, an analysis of the finescale shear and strain spectra is conducted. Studying mixing in areas of elevated mixing gives insight into the question of whether there is enough mixing to drive the MOC and if so what is the source of that mixing.

After analyzing internal waves and mixing in an area of mixing-driven upwelling, we then look at internal waves and mixing at high latitudes, in the Arctic Ocean, where deep
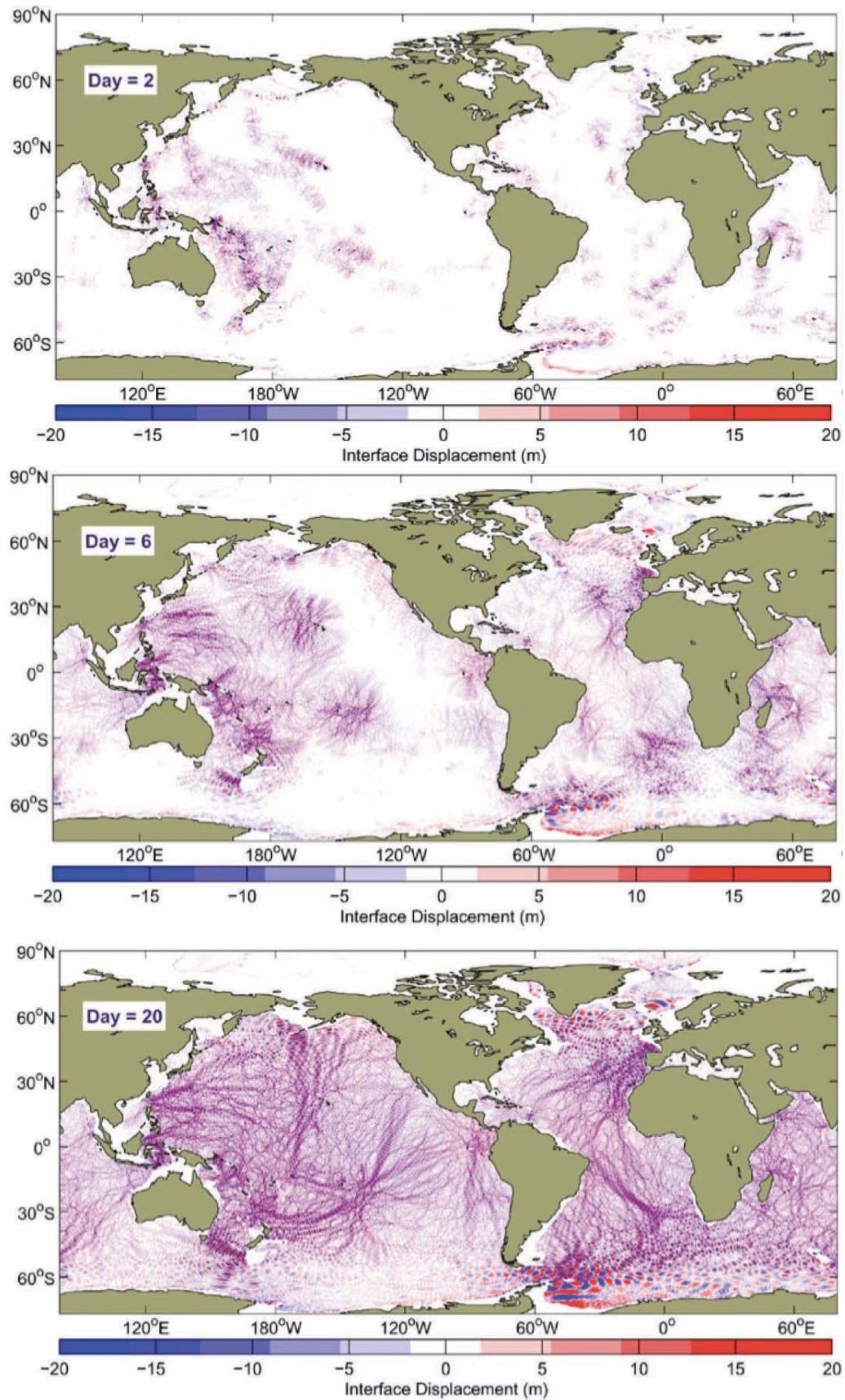
FIGURE 5 – Progression from Day 2 (top) to Day 6 (middle) to Day 20 (bottom) of internal M_2 semidiurnal tide generation in a global two-layer M_2 simulation by Simmons et al. (2004)
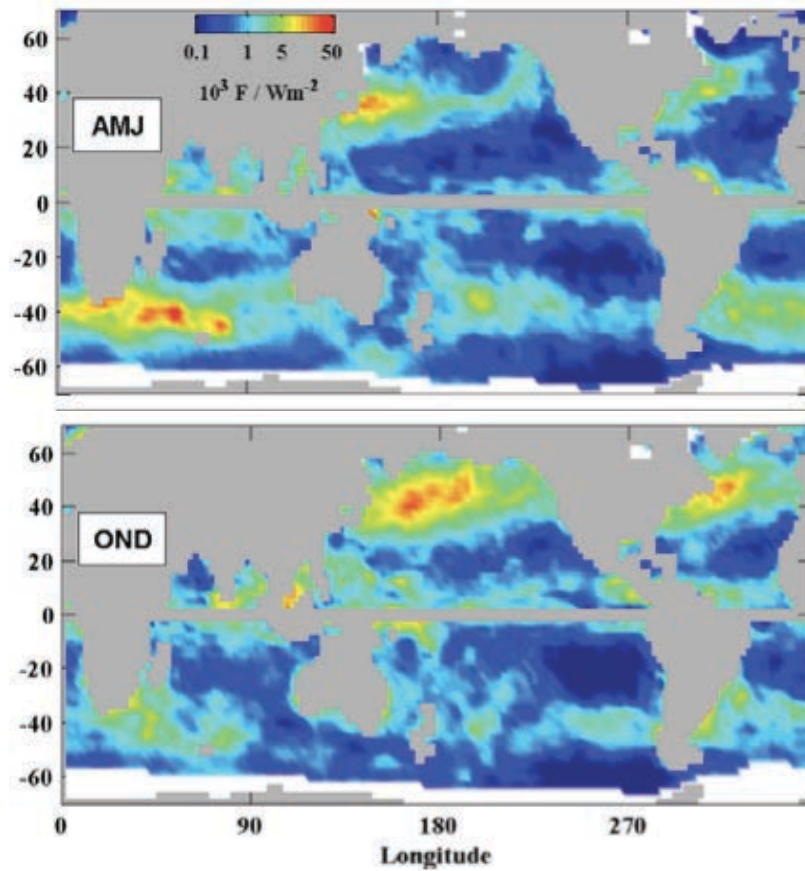
Figure 6 – The work done by the wind on the ocean, generating near-inertial waves, during April-May-June (above) and October-November-December (below) 1992, from Alford (2003b).
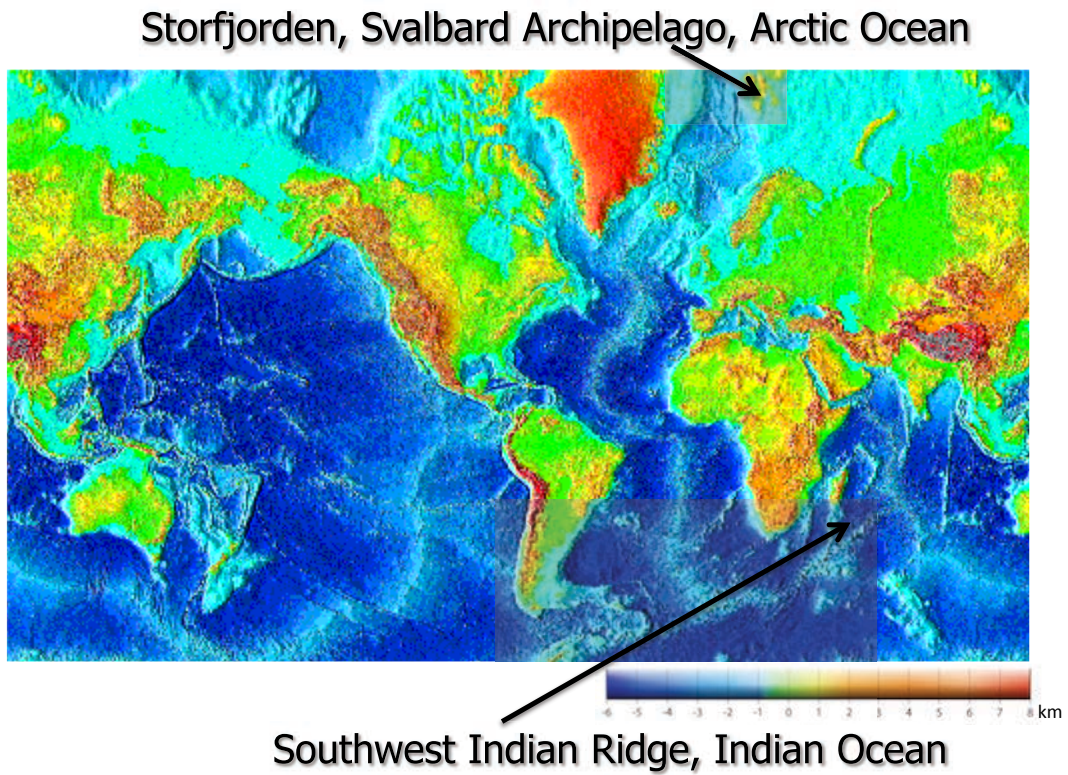
FIGURE 7 – Two study areas : Storfjorden, Svalbard Archipelago, Arctic Ocean, and the Southwest Indian Ridge, Indian Ocean.

water formation closes the MOC loop (Figure 1). Internal waves and mixing are highly affected by the environmental conditions in this Arctic region. The study in the Arctic took place in Storfjorden, a large fjord in the Svalbard Archipelago, and a site of deep water formation, responsible for nearly 5-10% of all Arctic Deep Water (Quadfasel et al., 1988). During these deep water formation events, mixing can be elevated orders of magnitude above the background level, and the stratification profile can change rapidly. The goal of this study is to understand how changing the stratification profile impacts the life cycle of the internal waves. In order to answer this question, this study looks at four time series from three consecutive springs in Storfjorden to see how differences in the stratification profile impact the dynamics and dissipation of the internal waves. If we can determine what factors control internal wave dynamics and dissipation under these conditions, we can get a better picture of how the ocean mixes at high latitudes.

This thesis begins with an analysis of the generation and propagation of the internal tide above the Southwest Indian Ridge (Chapter 2). The dissipation of the internal wave field and subsequent mixing in this region are then explored in Chapter 3. The fourth chapter looks at the lifecycle of internal waves at high latitudes, in an Arctic fjord, and specifically how changing the vertical structure of the stratification profiles impacts the dissipation of the internal waves and the subsequent mixing.

Chapitre 1

The State of the Art

In this chapter, we look at the fundamental background that serves as a basis for this research, as well as the previous research in the field. We start with an overview of the properties of internal waves, derive the dispersion relation, as well as the phase and group velocities. We then look at the energetics of internal waves, including their mechanical energy and the energy flux. Next we look at a specific case of internal waves, those that propagate at tidal frequencies, or the "internal tide," its generation, and propagation. We then look at what happens when these internal waves dissipate, and the subsequent turbulent mixing, evaluated by dimensional analysis and finescale parameterizations.

1.1 Properties of Internal Waves

1.1.1 Density

The density ρ of a fluid is a function of its temperature T, salinity S, and pressure p. In the case of seawater, which is a solution of dissolved salts, the salinity S is the mass of dissolved solids per unit mass of sea water. The density of seawater is determined by empirical approximations of the relative influence of these different thermodynamical properties in its equation of state

$$\rho = \rho(p, T, S)$$

Cold, salty water is denser than warmer, fresher water at the same pressure. The differences in temperature and salinity in the ocean lead to a stratified ocean interior with the density varying by a few parts per thousand over the ocean depth. The density can be broken down into its referenced value, ρ_o, it's average value, $\bar{\rho}$, and perturbations ρ' from the referenced state

$$\rho = \rho_o + \bar{\rho}(z) + \rho'(x, y, z, t).$$

Since the changes in density in the ocean are so small, $\rho'/\rho = O(10^{-3})$, we can apply the Boussinesq approximation to flows in the ocean, which allows us to ignore the perturbation densities except in the gravitational term, when the perturbation is multiplied with g, the acceleration due to gravity, and becomes too large to be ignored.

In a stable stratification, the denser waters lie below the lighter waters. The degree of stability can be inferred by the change in density with depth, $\frac{d\bar{\rho}}{dz}$. When a fluid element is displaced vertically, it is lighter or heavier than the surrounding fluid, and is no longer stable, so it will move back to its original position. The force which tries to return a fluid element to its reference position is the buoyancy force, $-\rho'\mathbf{g}$. The fluid element will not return to its exact reference position, but rather will overshoot, and oscillate about this position. The frequency at which it oscillates is the Brunt-Vaisala, or buoyancy, frequency,

$N = \sqrt{-\frac{g}{\rho_0}\frac{d\bar{\rho}}{dz}}$, which typically ranges from $10^{-2}s^{-1}$ at the pycnocline to $10^{-3}s^{-1}$ in the deep ocean (Gill, 1982). This "restoring force" leads to the propagation of internal waves in the stratified ocean, which propagate at a frequency up to the buoyancy frequency, $\omega \leq N$.

1.1.2 Dispersion Relation

To find the dispersion relation for small-scale internal waves, we begin with several approximations. We have already made the Boussinesq approximation assuming small changes in density. Along with the Bousinesq approximation, we also assume an equilibrium state where the mean state of the water is at rest relative to the earth, and is thus in hydrostatic balance, i.e. the gravitational force is balanced by a pressure gradient force. In order to consider the significant components of the pressure gradient force that contribute to the hydrostatic balance, we separate the pressure components in the same way we did for the density (equation 1.1.1). Hence,

$$p = p_o + \bar{p}(z) + p'(x, y, z, t).$$

Now, the hydrostatic balance can be written

$$\frac{d\bar{p}}{dz} = -\bar{\rho}g.$$

Another assumption is that the ocean is incompressible, which yields

$$\frac{\partial \rho'}{\partial t} + \nabla \cdot \rho\mathbf{u} = 0$$

We will first look at internal waves without taking into account the rotation of the earth. In this case, the Navier-Stokes equation for incompressible fluids reduces to

$$\rho_0 \frac{D\mathbf{u}}{Dt} = -\nabla p + \rho'g + \mu\nabla^2\mathbf{u}$$

which, far from boundaries where viscous effects are negligible, reduces to the Euler Equation (Kundu, 1990):

$$\rho_0 \frac{D\mathbf{u}}{Dt} = -\nabla p + \rho'g$$

Neglecting the product of perturbation quantities, the equations for density and momentum become:

$$\frac{\partial u}{\partial t} = -\frac{1}{\rho_o}\frac{\partial p'}{\partial x} \tag{1.1}$$

$$\frac{\partial v}{\partial t} = -\frac{1}{\rho_o}\frac{\partial p'}{\partial y} \tag{1.2}$$

$$\frac{\partial w}{\partial t} = -\frac{1}{\rho_o}\frac{\partial p'}{\partial z} - \frac{1}{\rho_o}g\rho' \tag{1.3}$$

$$\frac{\partial \rho'}{\partial t} - w\frac{N^2\rho_o}{\mathbf{g}} = 0 \tag{1.4}$$

$$\nabla \cdot \mathbf{u} = 0 \tag{1.5}$$

$$\tag{1.6}$$

In order to find a wave equation for an internal wave in terms of w, we differentiate the continuity equation 1.5 with respect to t and substitute from the horizontal momentum equations 1.1 and 1.2, which yields

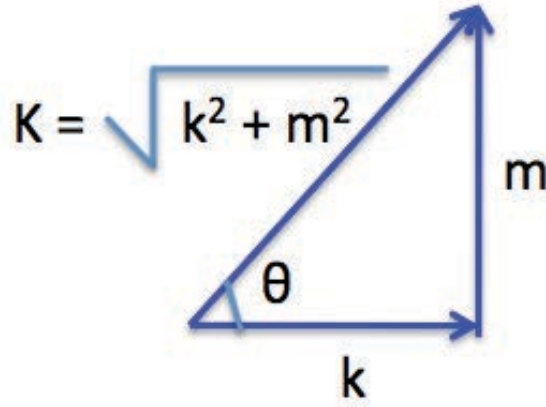$$\frac{1}{\rho_o}\nabla_H^2 p' = \frac{\partial^2 w}{\partial z \partial t}.$$

Figure 1.1 – Wavenumber vector **K** of an internal wave in the x-z plane, with l, the y component, set equal to 0. θ is the angle the wavenumber vector makes with the horizontal.

Next, we differentiate the vertical momentum equation with respect to t 1.3 and substitute from the density perturbation equation 1.4, which yields

$$\frac{1}{\rho_o}\frac{\partial^2 p'}{\partial t \partial z} = -\frac{\partial^2 w}{\partial t^2} - N^2 w.$$

We eliminate p' by taking ∇_H^2 of this equation to obtain

$$\frac{\partial^2}{\partial t \partial z}(\frac{\partial^2 w}{\partial t \partial z}) = -\nabla_H^2(\frac{\partial^2 w}{\partial t^2} + N^2 w), \tag{1.7}$$

which can be written

$$\frac{\partial^2}{\partial t^2}(\nabla^2 w) + N^2 \nabla_H^2 w = 0. \tag{1.8}$$

Since we are looking for wave-like solutions to the momentum equations, we assume w can be represented by

$$w = w_0 e^{i(kx+ly+mz-\omega t)}, \tag{1.9}$$

where w_0 is the amplitude, and k, l, and m are the x, y, and z components respectively of the wavenumber vector **K**. Plugging equation 1.9 into equation 1.8, yields the dispersion relationship for internal waves

$$\omega^2 = \frac{k^2 + l^2}{(k^2 + l^2 + m^2)}N^2. \tag{1.10}$$

To more clearly see some of the wave properties due to this dispersion relation, we orient the wavenumber vector so that the wave is propagating in the $x-z$ plane, so $l = 0$,

$$\omega = \frac{kN}{\sqrt{(k^2 + m^2)}}, \tag{1.11}$$

which, as can be seen in the simple depiction in Figure 1.1, is equivalent to

$$\omega = N\cos\theta, \tag{1.12}$$

where θ is the angle from the horizontal of the wavenumber vector. This shows us that the frequency of an internal wave does not depend on the magnitude of $\mathbf{K}$, but only its direction.

If we take into account the rotation of the earth, the horizontal momentum equations become:

$$
\begin{aligned}
\frac{\partial u}{\partial t} - fv &= -\frac{1}{\rho_o}\frac{\partial p'}{\partial x} \\
\frac{\partial v}{\partial t} + fu &= -\frac{1}{\rho_o}\frac{\partial p'}{\partial y}
\end{aligned}
$$

Still assuming the form of equation 1.9 for the solution, this yields the rotational internal wave dispersion relation

$$
\omega^2 = \frac{f^2 m^2 + N^2 k^2}{(k^2 + m^2)}, \tag{1.13}
$$

which is equivalent to

$$
\omega^2 = f^2 sin^2\theta + N^2 cos^2\theta \tag{1.14}
$$

The dispersion relation frequency v. phase propagation angle θ for internal waves is shown in Figure 1.2.

The dispersion relation for internal waves shows us that the frequency of internal waves does not depend on wavelength, but rather on the angle of the waves to the horizontal, θ. As can be seen in Figure 1.3, which shows internal waves produced by a vertical disturbance in a linearly stratified fluid, the internal waves propagate at a fixed angle to the horizontal, determined by the ratio of their frequency to that of the Brunt-Vaisala frequency.

The internal wave dispersion relation sets the bounds on the possible positive real frequencies of the internal wave spectrum. When an internal wave propagates directly along the horizontal, its wavenumber vector points in the direction of the horizontal, $\theta = 0$, and the frequency is equivalent to the buoyancy frequency, $\omega = N$. When an internal wave propagates purely in the vertical, $\theta = \pi/2$, and $\omega = f$. Thus, the frequency of internal waves are bounded by the inertial frequency f as a minimum and the Brunt-Vaisala, or buoyancy, frequency N as a maximum.

$$
f \leq \omega \leq N. \tag{1.15}
$$

1.1.3 Velocity

The velocity of the fluid displaced by an internal wave is given by

$$
\mathbf{u} = (u_0, v_0, w_0)e^{i(kx+ly+mz-\omega t)},
$$

where u_0, v_0, w_0 are complex amplitudes. If we take the dot product of the wavenumber vector and the fluid velocity, the continuity equation 1.5 tells us that

$$
\mathbf{K} \cdot \mathbf{u} = 0, \tag{1.16}
$$

which indicates that the wavenumber vector, which points in the direction of propagation of the internal wave, is orthogonal to the fluid velocity, and that internal waves are therefore transverse waves.
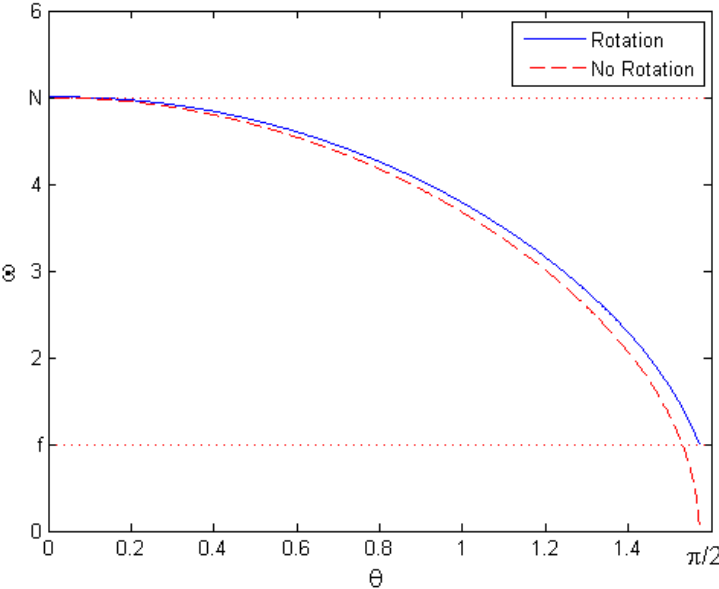
Figure 1.2 – Internal wave dispersion relation with rotation (solid blue line) and without rotation (dashed red line). When rotation is taken into account ω is bounded in the domain $[f_0, N]$. The frequency and wavenumber are given in non-dimensional form by dividing by a reference inertial frequency f_0. We choose $N = 5f_0$ to show the distinction between the rotational and non-rotational cases. This low N:f ratio corresponds to a rather low stratification environment.

The phase velocity has a magnitude $|\mathbf{C}| = \frac{|\omega|}{|\mathbf{K}|}$, and points in the direction of propagation. For internal waves, the phase velocity is given by:

$$\mathbf{C} = \frac{\omega}{|\mathbf{K}|}\hat{K} = \frac{[f^2 m^2 + N^2(k^2 + l^2)]^{\frac{1}{2}}}{k^2 + l^2 + m^2}\hat{k} \tag{1.17}$$

The group velocity, or the velocity at which the energy is conveyed along a wave is $\mathbf{C_g} = \nabla_k \omega$, which for internal waves becomes:

$$\mathbf{C_g} = \nabla_k \omega = \frac{N^2 - w^2}{|\mathbf{K}|^2}\left(\frac{k}{\omega}; \frac{l}{\omega}; \frac{m}{\omega}\frac{w^2 - f^2}{N^2 - \omega^2}\right) \tag{1.18}$$

If we take the dot product of the phase and group velocities,

$$\mathbf{C} \cdot \mathbf{C_g} = 0.$$

So, the phase and group velocities are in fact perpendicular, and the energy transport of an internal wave is orthogonal to the direction of phase propagation. As can be seen in Figure 1.3, which is a photo of the internal wave disturbance in a stratified fluid made by a vertically-oscillating elliptical object, the propagation of internal waves moves at right angles to the energy propagation.
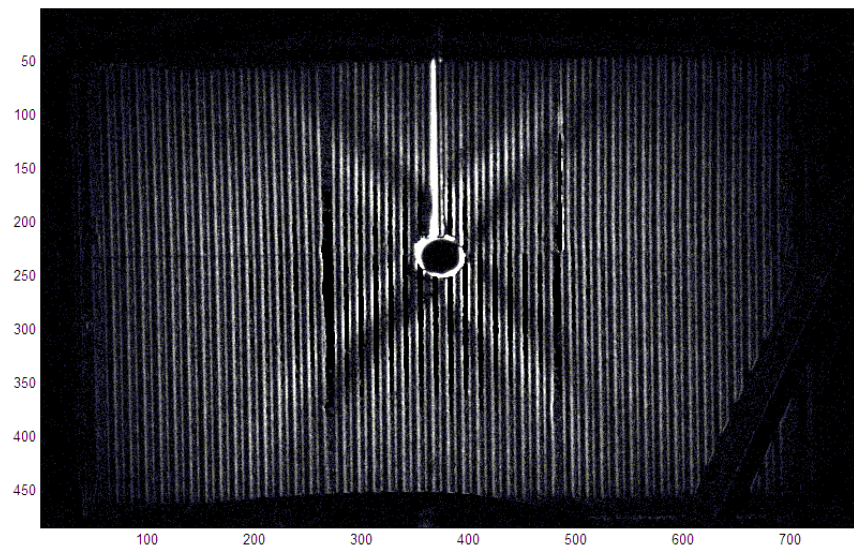
Figure 1.3 – Internal waves generated by a vertically-oscillating elliptical cylinder in a fluid of constant stratification ($N = 0.64 rad/s$). Internal waves propagate at approximately 59° to the horizontal, creating a pattern known as St. Andrew's Cross due to its unique shape. Figure provided by Jessica Kleiss.

1.2   Energetics of Linear Internal Waves

To find the equation for the rate of change of the energy density of internal waves, we take the dot product of the velocity $\mathbf{u}$ with the momentum equations 1.1 and 1.2, which yields

$$\frac{1}{2}\rho_0\frac{\partial \mathbf{u}^2}{\partial t} + \rho' gw + \nabla \cdot (p'\mathbf{u}) = 0.$$

The first term is the rate of change of the kinetic energy density, $KE = \frac{1}{2}\rho_0\mathbf{u}^2$, and the last term is the divergence of the energy flux, $F = <p'\mathbf{u}'>$. The second term can be rewritten as the rate of change of available potential energy. If we consider an isopycnal displacement η from the equilibrium, then $\rho' = \bar{\rho}(z_0+\eta) - \bar{\rho}(z_0)$. If η is small enough (or if N is constant) then the first order of the the Taylor expansion gives $\rho' = \frac{d\bar{\rho}}{dz}\eta = -\frac{g}{\rho_0}N^2\eta$. The available potential energy PE is the opposite of the work of the buoyancy force $\rho' g$ necessary to displace a fluid particle from z_0 to $z_0 + \eta$ which reads:

$$PE = \int_{z_0}^{z_0+\eta} \rho' gdz = \frac{1}{2}\rho_0 N^2\eta^2 = \frac{\bar{\rho'^2}g^2}{2\rho_0 N^2} \tag{1.19}$$

The result of the integral gives a term with a cross product $z_0\eta$. This term, however, has a null contribution over one wave period T since $<\eta>_T= 0$, and we therefore do not consider it in the expression of PE. Considering that the vertical velocity is the time derivative of the isopycnal displacement $w = \partial\eta/\partial t$ it follows that $\frac{\partial PE}{\partial t} = \rho' gw$ and equation 1.2 can be rewritten

$$\frac{\partial}{\partial t}E + \nabla \cdot (p'\mathbf{u}) = 0. \tag{1.20}$$

where $E = PE + KE = (\frac{1}{2}\rho_0\mathbf{u}^2 + \frac{\rho'^2 g^2}{2\rho_0 N^2})$ is the total mechanical energy density.

1.2.1   Mechanical Energy

The total average internal wave energy is the sum of the average kinetic and potential energies over one wave period T. Since multiple wave frequencies are present in observations, we average over an integer number of the longest wave period, i.e. the inertial period $2\pi/f$ (Nash et al., 2005).

$$\overline{E} = \overline{KE} + \overline{PE}, \tag{1.21}$$

Where the average kinetic energy per unit volume, $\overline{KE}$, is given by

$$\overline{KE} = \frac{1}{2}\rho_0(\overline{u^2 + v^2 + w^2}) \tag{1.22}$$

and the average available potential energy per volume,

$$\overline{PE} = \frac{\bar{\rho'^2}g^2}{2\rho_0 N^2}. \tag{1.23}$$

To find the mechanical energy of a linear internal wave, we consider an internal wave in the $x-z$ plane, without rotation, i.e. $f = 0$. The variables can be defined by the wave-like solution

$$[u, w, p', \rho'] = [u_0, w_0, p_0, \rho_0]e^{i(kx+mz-\omega t)}. \tag{1.24}$$

Using the continuity equation 1.5, the solution for u can be expressed in terms of w

$$u = -\frac{m}{k}w_0 e^{i(kx+mz-\omega t)}. \tag{1.25}$$

Similarly, from equation 1.1, p' can also be expressed in terns of w

$$p' = -\frac{\rho_0 \omega m}{k^2} w_0 e^{i(kx+mz-\omega t)}. \qquad (1.26)$$

From the equation for the density perturbation 1.4, the solution for ρ' can also be expressed in terms of w

$$\rho' = \frac{i\rho_0 N^2}{\omega g} w_0 e^{i(kx+mz-\omega t)}.$$

Since the average of sine and cosine over one period is $\frac{1}{2}$, and the average energies become

$$\overline{KE} = \frac{1}{4}\rho_0(1 + m^2/k^2)w_0^2$$

$$\overline{PE} = \frac{1}{4}\frac{\rho_0 N^2}{\omega^2}w_0^2,$$

Substituting from the dispersion relation in the x-z plane, equation 1.11, $\overline{PE}$ becomes

$$\overline{PE} = \frac{1}{4}\rho_0(1 + m^2/k^2)w_0^2,$$

which is equivalent to the average kinetic energy, $\overline{KE}$. So, when we do not take into account the rotation of the earth, there is an equipartition of energy for internal waves. The total average internal wave energy then becomes

$$\overline{E} = \overline{KE} + \overline{PE} = \frac{1}{2}\rho_0(1 + m^2/k^2)w_0^2. \qquad (1.27)$$

or equivalently, as a function of θ,

$$\overline{E} = \frac{1}{2}\rho_0(w_0^2/cos\theta^2).$$

The same computation can be made with rotation, and in this case there is no equipartition of energy, but rather the ratio KE to PE reads:

$$\frac{KE}{PE} = 1 + \frac{2f^2}{N^2}\tan^2(\theta).$$

when the propagation angle $\theta = \pi/2$, which corresponds to a pure inertial wave, $\omega = f$, (equation 1.13), the ratio of KE to PE goes to infinity, and thus all the mechanical energy for an inertial wave is purely kinetic. At the opposite limit $\theta = 0$, corresponding to $\omega = N$, rotational effects collapse and we recover the equipartition of energy for internal waves in a non-rotating fluid. Since a large part of the energy in the ocean comes from atmospheric forcing, there is a large near-inertial frequency component to the oceanic internal wave field. Also, a typical energy spectrum has a slope of approximately -2, indicating a rapid decrease in energy density with increasing frequency, indicating that there is more internal wave energy near f than near N (see section 1.2.2). Thus, most of the internal wave energy observed in the ocean has a large ratio of KE/PE.

1.2.2 The Garrett-Munk Spectrum

One way to look at the overall energy level of an internal wave field is to look at its energy spectra. The frequency spectra of the velocity yields its kinetic energy power spectrum, while that of the isopycnal displacements, η, yields its potential energy power spectrum. In order to compare the relative power spectra from various internal wave fields, a reference spectrum is often used.

The internal wave field in the ocean is a superposition of numerous waves with various frequencies and wavenumbers. The repartition of the spectral energy density in wavenumber and frequency, however, was found to have a remarkable universal shape when observed in the deep open ocean far from boundaries. This universal shape was found by taking an empirical fit to numerous data sets of internal wave spectra at midlatitudes, yielding the canonical Garrett-Munk spectrum. First proposed by Garrett & Munk (1972), and later modified by Garrett & Munk (1975), the latest version of the Garrett-Munk spectrum, as described by Garrett & Munk (1979), hereafter $GM79$, has become the reference spectrum for all internal wave spectra. In situ data are commonly compared to $GM79$ to compare the relative energy level of the internal wave field.

The empirical model spectrum $GM79$ was based on several dimensional considerations. The internal wave field used to define the $GM79$ spectrum consists of a random combination of linear waves with random phases assumed to be horizontally isotropic, and thus $GM79$ employs only a single horizontal wavenumber, $k = (k_1^2 + k_2^2)^{\frac{1}{2}}$ (Munk, 1981). The spectra of vertical displacement and energy per unit mass, from Munk (1981), are:

$$F_\zeta(\omega) = \frac{2}{\pi} r \frac{f}{N} \frac{(\omega^2 - f^2)^{\frac{1}{2}}}{\omega^3} \tag{1.28}$$

$$F_E(\omega) = \frac{2}{\pi} r \frac{f}{\omega} \frac{N}{(\omega^2 - f^2)^{\frac{1}{2}}} \tag{1.29}$$

Finally the corresponding energy or mean-square quantities from 1.28 and 1.29 are,

$$\left\langle \zeta^2 \right\rangle = \frac{1}{2} b^2 E_o N_o N^{-1} = 53 \frac{N_o}{N} m^2 \tag{1.30}$$

$$\hat{E}(z) = b^2 E_o N_o N = 30 \frac{N}{N_o} m^2 s^{-2} \tag{1.31}$$

where $E_o = 6.3 \times 10^{-5}$ is the non dimensional energy level, $b = 1300m$, the vertical scale of N variations, $N_o = 3cph$, the reference buoyancy frequency, and $r = E_0 b^2 N_0$.

From this model it can be easily inferred that the vertical displacement and energy spectral levels are proportional to $1/N$ and N, respectively and that at high frequencies, $\omega >> f$, the frequency dependence is ω^{-2}.

1.2.3   Energy Flux

Another important value when assessing the energetics of an internal wave field is its energy flux, which indicates the direction and magnitude of the energy of the internal waves. To simplify the equations, the energy flux is shown here in the x-z plane in the absence of rotation (i.e. $f, l = 0$). From equation 1.2, the average energy flux per unit area is

$$\overline{F} = \overline{p'\mathbf{u}'},$$

where the average is taken over several inertial periods (Nash et al., 2005). Using the form of the velocity in equation 1.25,

$$\overline{F} = \frac{\rho_0 \omega m}{2k^2} w_0^2 (m/k, 0, -1)$$

Taking the product of the group velocity for an internal wave in the $x - z$ plane, from equation 1.18, and the total average internal wave energy from equation 1.27, yields

$$\overline{E} c_g = \frac{\rho_0}{2} (1 + \frac{m^2}{k^2}) \frac{Nm}{K^3} w_0^2,$$
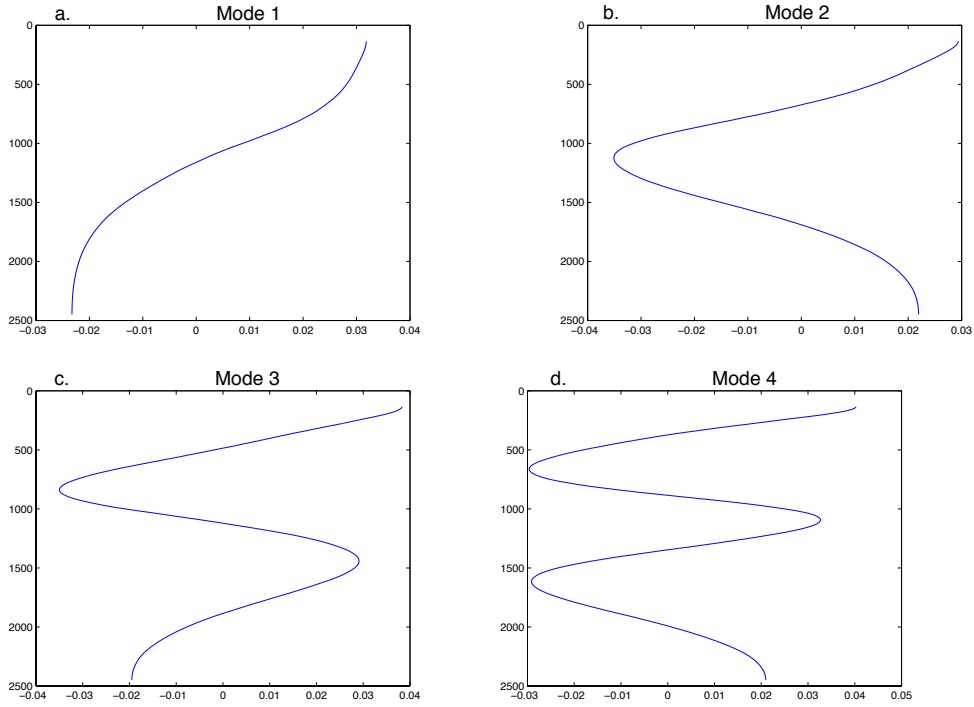
Figure 1.4 – The first four vertical modes of the horizontal velocity of an internal wave determined from a stratification profile in the Indian Ocean.

which, after applying the dispersion relation equation 1.11,

$$\overline{E}c_g = \frac{\rho_0 \omega m}{2k^2} w_0^2.$$

So, the energy flux for linear internal waves can be defined as

$$\overline{F} = \overline{p'\mathbf{u'}} = \overline{E}c_g.$$

The energy flux of a group of internal waves is thus the product of the total average wave energy E and its group velocity $\mathbf{c_g}$.

1.3   Internal Wave Modes

One way to describe the motion of internal waves, is to break it down into waves that only propagate in the horizontal and have fixed vertical structure, i.e. the different vertical modes. The mode number corresponds to the number of zero crossings in the vertical profile of the horizontal velocity or pressure, as can be see in Figure 1.4. As can be see in Figure1.4, mode 1 has one zero crossing where the velocity changes sign in the water column. In this case, the horizontal motion changes by 180° at the zero crossing, so while fluid particle displacements are positive in the upper water column, they are negative in the lower water column and vice versa. The number of zero crossings increases with the mode number, so higher modes have more changes in horizontal velocity throughout the water column.

The vertical modes depend on the stratification of the system, as defined by the Brunt-Vaisala frequency N. To find the modes, we start with equation 1.8. We then assume a

wave-like solution of the form

$$\mathbf{w} = W(z)e^{i(kx+ly-\omega t)},$$

which, substituted into equation 1.8, yields

$$\frac{d^2W}{dz^2} + \frac{N^2(z) - \omega^2}{\omega^2}(k^2 + l^2)W = 0.$$

Assuming no flux through the bottom, $-h$, the bottom boundary condition in terms of $W(z)$ becomes

$$W = 0 \qquad (1.32)$$

at $z = -h$, and assuming a free-surface with a constant atmospheric pressure, the surface boundary condition in terms of $W(z)$ becomes

$$\omega^2 \frac{dW}{dz} - gk^2 W = 0 \qquad (1.33)$$

at $z = 0$. Solving for the eigenvalues of $W(z)$ (equation 1.3), and the two boundary conditions, equations 1.32 and 1.33, yields the modes (eigenvectors) and frequencies (eigenvalues) of the system. Once the modes have been determined, the vertical velocities can be projected onto the modes, to determine how much energy is in each mode.

1.4 Internal Tide

While the frequencies of real internal waves are bounded by the inertial and Brunt-Vaisala frequencies (equation 1.15) the dominant internal wave frequencies are the near-inertial frequencies and the tidal frequencies. When the barotropic tide comes into contact with bottom topography, internal baroclinic waves are generated that propagate at tidal frequency, or the internal tide. The mechanism of generation of an internal tide is illustrated in Figure 1.5 for the simplified case of 2-layer stratification in 2D (x,z). The continuity equation for a varying bottom topography results in the generation of a barotropic vertical velocity, $W(z)$. This vertical velocity advects the interface between the two layers at tidal periods and generates a baroclinic wave at the tidal frequency. For the sake of simplicity, the sketch neglects the vertical baroclinic velocity that arises as soon as the baroclinic wave is generated.

The tides are forced by the gravitational pull of the moon, and to a lesser extent the sun, on the oceans. A strong diurnal and semidiurnal tidal signal, as well as their harmonics, are evident in ocean time series. The interaction of the gravitational pull of the sun and that of the moon leads to different tidal components of multiple frequencies, as can be seen in Table 1.1. The interference of the solar and lunar tides leads to a spring-neap cycle of stronger and weaker tides respectively. Each tidal component can generate an internal tide at that tidal component frequency when the barotropic tide interacts with topography.

1.4.1 Ray Paths

Since the frequency of the internal tide is known, the internal wave dispersion relation, equation 1.13, can be used to trace their ray paths, using the inverse slope of the internal tide

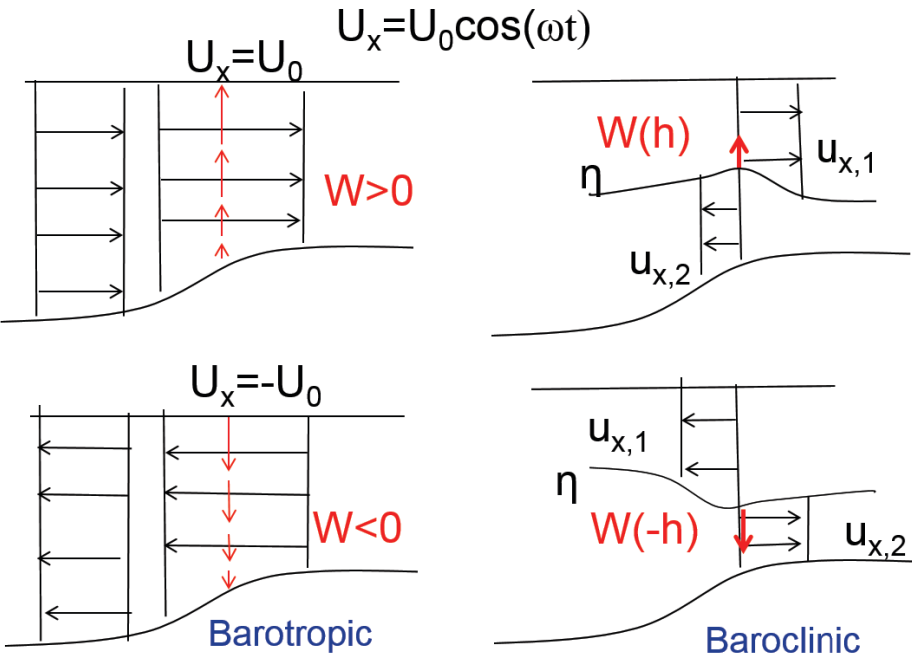$$\frac{dx}{dz} = \sqrt{\frac{N^2 - \omega^2}{\omega^2 - f^2}}, \qquad (1.34)$$

Figure 1.5 – Barotropic v. baroclinic waves.

Table 1.1 – Principal Tidal Harmonic Components. (from Defant (1961))

Tide name	Symbol	Period in solar hours	Ratio (% of M_2)
Semi-diurnal components			
Principal lunar	M_2	12.42	100
Principal solar	S_2	12.00	46.2
Larger lunar elliptic	N_2	12.66	19.2
Luni-solar semi-diurnal	K_2	11.97	12.7
Diurnal components			
Luni-solar diurnal	K_1	23.93	58.4
Principal lunar diurnal	O_1	25.82	41.5
Principal solar diurnal	P_1	24.07	19.4

$$\text{Ray Slope} = \quad \frac{dx}{dz} = \sqrt{\frac{\langle N^2 \rangle - \omega^2}{\omega^2 - f^2}}$$
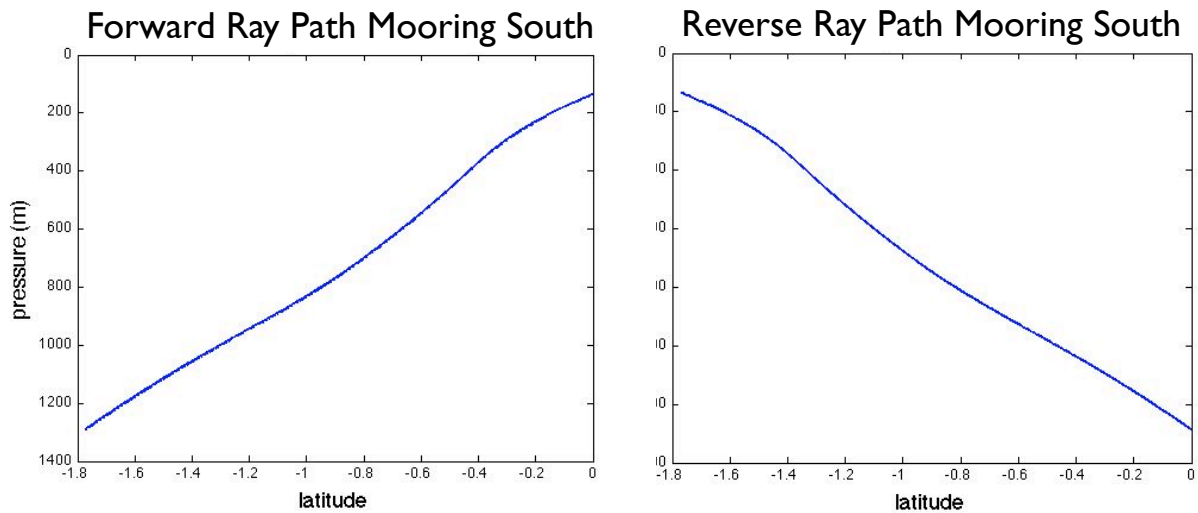
Figure 1.6 – Internal wave raypath calculated from the internal wave dispersion relation using a stratification from the Indian Ocean.

where ω is the tidal frequency. When the stratification $N(z)$ varies slowly compared with the vertical scale of the wave m^{-1}, a WKB approximation can be made by assuming that the previous relationship is verified locally. Equation 1.34 can then be integrated numerically for any profile of $N(z)$. An example of internal wave ray paths is shown in Figure 2.9.

1.4.2 Theoretical Internal Tide Generation

The conversion from barotropic to baroclinic energy is theoretically determined by the amount of power available to go into the internal tide. The theoretical power available for conversion can be calculated as the product of the Baines (1982) Force $F_b = N^2 w_{bt}\omega^{-1}$ and the vertical component of the barotropic velocity $w_{bt} = \mathbf{u_{bt}} \cdot \nabla \mathbf{H}(z/H)$:

$$F_b w_{bt} = \frac{N^2 w_{bt}^2}{\omega} = \frac{N^2 [\mathbf{u_{bt}} \cdot \nabla \mathbf{H}(z/H)]^2}{\omega},$$

To infer the theoretical internal tide generating force, based on Baines (1982)

$$\|\vec{F}\| = \frac{N^2}{\omega} z \frac{\|\vec{Q} \cdot \nabla h\|}{h^2},$$

where N is taken to be uniform in our calculation, ω is the tidal frequency (M_2), $\|\vec{Q}\|$ is the barotropic tidal flux, and h is the bottom depth.

Following Nash et al. (2006), we first find the theoretical depth-integrated energy flux over the region of generation:

$$\Delta F_E = \int_{x_1}^{x_2} [\int_{-H}^{0} < F_b w_{bt} > dz] dx,$$

We would expect internal tide generation to occur when the topographic slope is nearly equivalent to the wave ray slope. The ratio of the topographic slope to the wave ray slope, as defined in Baines (1986), is:

$$\gamma = \frac{\Delta H/\Delta y}{\alpha},$$

where $\alpha = \frac{dz}{dx}$ is the slope of the internal tide. According to Baines (1986), when the ratio of the topographic slope to that of the internal tide is between 0.5 and 2, the topographic slope is near critical, and internal tide generation is likely.

$$\gamma = \frac{\Delta H/\Delta y}{\alpha}, \tag{1.35}$$

where

$$\alpha = \frac{1}{tan\theta} = (\frac{w^2 - f^2}{N^2 - \omega^2})^{\frac{1}{2}} \tag{1.36}$$

1.5 Mixing

When internal waves break, the kinetic energy transfers to turbulent microscale eddies that dissipate kinetic energy as heat. Turbulent motions are complex nonlinear motions that cannot be predicted in detail, but only quantified statistically. Turbulence theory assumes these turbulent motions are isotropic, with no preferred orientation; homogeneous, being statistically the same throughout; and stationary, or constant in time.

To quantify how turbulent a flow is, we look at how quickly it dissipates its kinetic energy. The rate of loss of the kinetic energy of the turbulent motion per unit mass through viscosity to heat, ϵ, gives a measure of the strength of turbulent mixing.

$$\epsilon = \nu(\frac{\partial \mathbf{u}'}{\partial x}^2 + \frac{\partial \mathbf{u}'}{\partial y}^2 + \frac{\partial \mathbf{u}'}{\partial z}^2) \tag{1.37}$$

where ν is the fluid viscosity, with units $m^2 s^{-1}$, or a squared unit length L per unit time T. Since $\frac{\partial \mathbf{u}}{\partial y}$ has units s^{-1}, the units of ϵ are $m^2 s^{-3}$, or $L^2 T^{-3}$. The rate of turbulent dissipation ϵ controls the scale of the turbulence. The limits of the scales of turbulence can be found by dimensional analysis. At the smallest scales of turbulence where the viscous dissipation is dominant, the length scale must depend only on ν and ϵ, which have dimensions $L^2 T^{-1}$ and $L^2 T^{-3}$, respectively. To find a length scale using just these two quantities, we cube ν and divide by ϵ to eliminate the time, and take the fourth root to get a length (Thorpe, 2005):

$$((L^2 T^{-1})^3 (L^2 T^{-3})^{-1})^{\frac{1}{4}} = L \tag{1.38}$$

where the length is equivalent to the smallest scale of turbulence, the Kolmogorov length scale, l_K.

$$l_K = (\nu^3 \epsilon^{-1})^{\frac{1}{4}} \tag{1.39}$$

To satisfy the constraint that turbulence is isotropic, the largest turbulent eddy scales cannot exceed the depth of the water column, so the scale of the turbulence will be constrained either by the geometry of the system, or the stratification, N. Greater rate of turbulent dissipation ϵ means more energy to overcome the vertical density gradients. Thus the largest length scales of the turbulent eddies increase as the rate of turbulent dissipation ϵ increases, and decrease with the stratification. Using dimensional analysis, and the two quantities ϵ and N whose dimensions are $L^2 T^{-3}$ and T^{-1} respectively, to find a length scale that satisfies these constraints, we divide ϵ by the N cubed and take the square root

$$((L^2 T^{-3})(T^3))^{\frac{1}{2}} = L, \tag{1.40}$$

where L is equivalent to the outer scale of turbulence, the Ozmidov length scale (Dillon, 1982).

$$L_o = (\epsilon N^{-3})^{\frac{1}{2}}. \tag{1.41}$$

L_O is the maximum vertical displacement of a fluid particle within a turbulent overturn, after it has converted all of its kinetic energy to potential energy.

One way to quantify turbulence is to measure the micro-scale motions directly through microstructure measurements. In the absence of microstructure measurements, however, larger-scale parameters, including stratification and shear, can be used to get an approximation of the magnitude of the mixing generated by the internal wave field, based on dimensional scaling and finescale parameterizations.

1.5.1 Thorpe Scale Dimensional Analysis

One of the parameters that is easily measured is the density. Segments in a density profile that are unstable, i.e. denser water lying above lighter water, known as an overturn, indicate that energetic events altered the potential energy of the water column. The length of density overturns is directly related to the outer scale of turbulence, L_O, and can thus be used to dimensionally determine ϵ.

To find the length of the density overturn, an observed density profile is sorted so the denser water is below the lighter water. The new depth of each data point in the sorted profile is then compared to the actual depth of the same point in the observed profile.

The difference between the two positions is called the Thorpe displacement, d' (Thorpe, 2005), and the root mean square of this quantity, the Thorpe length, L_{Th}

$$L_{Th} = \overline{(d'^2)}^{\frac{1}{2}} \tag{1.42}$$

A linear relationship between L_{Th} and L_O, allows us to find an approximation for the rate of turbulent dissipation, ϵ_{Th}, (Thorpe, 1977; Dillon, 1982; Ferron et al., 1998)

$$\epsilon_{Th} = c_1 L_{Th}^2 (N_{ot}^3)[W kg^{-1}]$$

where N_{ot} is the average sorted stratification within the overturn, and the constant $c_1 = L_0/L_T$ ranges from $.63 - .91$ (Thorpe, 2005).

1.5.2 Finescale Parameterizations

While Thorpe-scale analysis determines the rate of turbulent dissipation by dimensional scaling of larger-scale turbulent overturns in a stratified fluid, irrespective of the source of the overturns, finescale parameterizations use measurements of shear that are assumed to be due to internal waves, as well as the stratification, to parameterize the mixing. Finescale parameterizations assume that the measured shear is due to internal waves, and that the spectral shape of the internal wave field is in a steady state. The rate of turbulent dissipation can then be determined from the eikonal wave-wave interaction model and the assumption that the energy dissipation rate is primarily due to nonlinear internal wave interactions that transfer energy from the finescale $(10 - 100m)$ towards the micro scale (cm) turbulence (Henyey et al., 1986; MacKinnon & Gregg, 2003, 2005; Whalen et al., 2012).

Common finescale parameterizations include the the Gregg-Henyey (GH) parameterization (Gregg, 1989), the MacKinnon-Gregg (MG) parameterization (MacKinnon & Gregg, 2003, 2005), and the Kunze et al. (2006) shear-strain parameterization (Gregg et al., 2003; Kunze et al., 2006). GH, the most germaine of these fine-scale parameterizations, is based on comparison between empirical open-ocean data, and the Garrett-Munk (GM) model. The rate of turbulent dissipation determined by GH, hereinafter ϵ_{GH}, scales the fourth power of the observed 10-m shear with that of GM.

$$\epsilon_{GH} = 1.8 \times 10^{-6}[fcosh^{-1}(N_0/f)](S_{10}^4/S_{GM}^4)(N^2/N_0^2)[Wkg^{-1}],$$

where S_{GM} is the modeled 10-m Garrett-Munk shear, $S_{GM}^4 = 1.66 \times 10^{-10}(N^2/N_0^2)^2 s^{-2}$, S_{10} is the shear at 10-m resolution, and $N_0 = 3$ cph.

While GH was intended to parameterize waves in the open ocean, MG modifies GH for low-mode dominated coastal regions for which the GM spectrum is not a good representation. As opposed to the GH scaling, which relies on 10-m resolution shear scaled by the GM shear variance, the turbulent rate of dissipation determined by MG, hereinafter ϵ_{MG}, relies on 1-m resolution low-frequency mode-1 shear.

$$\epsilon_{MG} = \epsilon_0(N/N_0)(S_1/S_0)[Wkg^{-1}],$$

where $S_0 = N_0 = 3$ cph, and ϵ_0 is an adjustable parameter found by fitting ϵ_{MG} to simultaneous microstructure measurements, which MacKinnon & Gregg (2005) find to be equal to $1.1 \times 10^{-9} Wkg^{-1}$.

While GH and MG focus on using the shear to parameterize the mixing, Kunze et al. (2006) use not only the shear, but also the strain, ζ_z.

$$\epsilon_{shst} = \epsilon_0 \frac{\bar{N}^2}{N_0^2} \frac{<V_z^2>}{<V_{zGM}^2>^2} h(R_\omega)j(\frac{f}{N})[Wkg^{-1}],$$

where,

$$h(R_\omega) = \frac{3(R_\omega + 1)}{2\sqrt{2}R_\omega\sqrt{R_\omega - 1}}$$

and,

$$j\left(\frac{f}{N}\right) = \frac{f arccosh(N/f)}{f_{30}arccosh(N_0/f_{30})}$$

$f_{30} = f(30^o)$, and $N_0 = 5.2 \times 10^{-3} rads^{-1}$. The shear-strain variance ratio

$$R_\omega = \frac{<V_z^2>}{N^2<\zeta_z^2>}.$$

for the GM frequency spectrum, $R_\omega GM = 3$.

1.5.3   Diapycnal Eddy Diffusivity (κ_z)

Following the assumption that turbulence is stationary, and thus that the total turbulent kinetic energy (TKE) is constant in time, there must be a balance between the sources and sinks of TKE. TKE sinks include the buoyancy flux $b = g < \rho'w > /\rho_0$ and the dissipation rate $\epsilon = \nu(\frac{\partial \mathbf{u'}}{\partial x}^2 + \frac{\partial \mathbf{u'}}{\partial y}^2 + \frac{\partial \mathbf{u'}}{\partial z}^2)$, with primes denoting fluctuations from the mean. The dominant source of TKE is due to the rate of working of the Reynold's stress on the mean shear, or the shear production term, $< uw > dU/dz$. If the TKE is in a steady state, these three terms balance (Thorpe, 2005)

$$< uw > dU/dz + \epsilon + g < \rho'w > /\rho_0 = 0 \tag{1.43}$$

Taking the ratio of the rate of removal of energy by buoyancy forces to the production of turbulent kinetic energy by the shear, or, the flux Richardson number,

$$R_f = \frac{g(< \rho'w > /\rho_0)}{< uw > dU/dz}, \tag{1.44}$$

and the rewriting $\kappa_z = - < \rho'w > /(d < \rho > /dz)$ in terms of N, so $\kappa_z = g < \rho'w > /\rho_0 N^2$, allows us to define κ_z as

$$\kappa_z = [R_f/(1 - R_f)]\epsilon/N^2. \tag{1.45}$$

We can then define

$$\Gamma = R_f/(1 - R_f), \tag{1.46}$$

where Γ is known as the mixing efficiency. Osborn (1980) found that the upper bound for Γ is 0.2 and this value is commonly used to determine κ_z from ϵ. Several recent studies, however, have also shown that the mixing efficiency decreases with the turbulence intensity I which is defined as:

$$I = \frac{\epsilon}{\nu N^2},$$

where ν is the kinematic viscosity of water. I can be seen as the ratio of the stabilizing effects of viscosity and stratification against the destabilizing effects of turbulence. Using high-resolution numerical simulations of stratified turbulence, Shih et al. (2005) have proposed empirical laws to parameterize κ_z as a function of I. They define three regimes: In the diffusive range where the turbulent intensity is low, the total diffusivity reverts to the molecular value, $\kappa_T = 1 \times 10^{-7} m^2/s$. If the turbulent intensity is in an intermediate range between 7 and 100, κ_{turb} is defined by the Osborn (1980) relation, $\kappa_{turb} = \frac{\Gamma\epsilon}{N^2}$, with $\Gamma = 0.2$. If, however, the turbulent intensity is elevated above 100, $\kappa_{turb} = 2\nu I^{\frac{1}{2}}$. The total κ_z is then found by adding $\kappa_{turb} + \kappa_T$.

Estimates of diapycnal diffusivities have been made across the ocean, revealing strong spatial variability. Areas of heightened diffusivities have been detected above topographic features, such as mid-ocean ridges, and at ocean boundaries, with much weaker diffusivities occurring in the open ocean far from ridges and boundaries (e.g. Polzin et al., 1997; Kunze et al., 2006). In order to close the global overturning circulation energy balance posed in the Introduction, we need to accurately parameterize the diffusivities throughout the ocean. The goal of this thesis is to look closely at the internal wave field in two distinct ocean regions, the Indian and Arctic Ocean basins, and based on the background theory presented in this chapter, characterize their internal wave fields. If we can understand how different environmental conditions affect the life cycle of the internal waves in these specific areas, we can more accurately parameterize their generation, propagation, and subsequent dissipation into turbulent mixing throughout the ocean.

Chapter 2

Internal Tide Generation Over the Southwest Indian Ridge

Abstract

Internal tides play a vital role in the cascade of energy between large-scale winds and tides and the small-scale turbulence that mixes the ocean. To better understand internal tide generation and propagation, we look at the internal wave field above an area of rough topography in the Indian Ocean, the Southwest Indian Ridge. Two moorings were deployed in 2500 meters of water on the north and south ends of the western side of the Atlantis II Fracture Zone in the center of the ridge from November 2007 - January 2008 as part of the Southwest Indian Ridge Mixing Project (SWIRM). Each mooring was equipped with two McLane Moored Profilers, one in the top, and one in the bottom half of the water column, yielding time series throughout the water column. Fourier transforms of the time series reveal that the strongest signal in the region is the M_2 semidiurnal internal tide. The data are then filtered to isolate the internal tide. Both kinetic and potential energy show complex vertical structures consistent with high-mode beam-like structures. Ray paths from the locations of these tidal beams in the direction of the energy flux indicate the probable internal tide generation sites. Comparison of the observed generation sites with the sites predicted by theory reveal the complexity of the region. Tidal beams that can be ray-traced to a point of interception where the slope of the topography is greater than .65 the slope of the M_2 tide, agree well with theory, whereas tidal beams whose ray paths intercept topography with a slope less than .65 the slope of the M_2 tide, do not. Those tidal beams whose generation sites do not agree with theory cannot be ray-traced back to one simple generation site, but are thought to occur due to reflection and interference of the internal tide over the rough topography. Variation of the ray paths is consistent with changes in the mesoscale.

2.1 Introduction

The internal tide plays an important role in ocean circulation. The Meridional Overturning Circulation requires warmer surface water be mixed down to a lower geopotential height, to induce the convection necessary for the observed large-scale overturning circulation (Munk & Wunsch, 1998). Since the main source of mechanical energy in the oceans comes from the winds and tides, there must be a cascade of energy from the large-scale winds and tides to the small-scale turbulence that mixes the ocean. Internal waves act as conduits between large- and small-scale energy in the ocean. The internal tides, internal waves at tidal frequency, are one of the biggest components of the internal wave field, and

are largely responsible for this energy cascade. The generation of the internal tides in areas of relatively simple topography, such as the Hawaiian Ridge (e.g. Rudnick et al., 2003; Merrifield & Holloway, 2002; Rainville & Pinkel, 2006; Nash et al., 2006; Klymak et al., 2008; Cole et al., 2009), as well as areas of complex topography, such as the Mid-Atlantic Ridge (e.g. Zilberman et al., 2009; Dovgaya & Cherkesov, 1996; Thurnherr et al., 2002) has both local as well as far-reaching effects on the internal wave field. In this study, we look at internal tide generation over an area of rough corrugated topography, the Southwest Indian Ridge, to better understand the effects of environmental conditions on the generation and propagation of the internal tide.

The Southwest Indian Ridge is a slow-spreading ridge separating the Antarctic and African plates that is characterized by steep valleys and rough topography, as depicted in Figure 3.2. WOCE reanalysis data indicate that turbulent diapycnal mixing is elevated orders of magnitude above background levels over the rough topography of the ridge (Kunze et al., 2006). For just over one month, from December 2007 to January 2008, two moorings were deployed on the western crest of the Atlantis II Fracture Zone, a steep-walled canyon in the center of the Southwest Indian Ridge, as shown in Figure 3.2, as part of the Southwest Indian Ridge Mixing Project (SWIRM). Each mooring was equipped with two McLane Moored Profilers, one in the upper, and one in the lower half of the water column. One mooring was deployed on the north (hereinafter Mooring North) and the other on the south (hereinafter Mooring South) end of the western side of the fracture zone. The profilers collected temperature, conductivity, and current meter data which provide a long-term record of tidal variability.

This paper analyzes the spatial and temporal variability of the current meter data to determine the frequency and magnitude of the local internal waves, and from that information, determine the genesis of those waves. Section 4.2 describes how the velocity data are interpolated, and Fourier-transformed to determine that the internal M_2 tide is the strongest signal. The data are then bandpass filtered around this powerful internal tide signal. The kinetic and potential energies of the filtered internal tide data, as seen in Section 2.3, reveal a high-mode vertical structure. The energy in this case, however, is more vertically localized than one would expect in any high mode. These areas of highly-concentrated tidal energy, or "tidal beams," occur at specific depths in the water column. To find the source of these tidal beams, in Section 2.4, the center of the beams are determined, and the energy flux calculated at these locations. The arctangent of the meridional over the zonal energy flux then yields the direction of the tidal beams. The ray paths are then plotted in the direction of the energy flux through the tidal beam locations to determine probable sites of internal tide generation. The theoretical internal tide generation is calculated based on Baines (1982) in Section 2.4.3. Comparing the observed and theoretical generation, we see that while the theory is consistent with the observations in some circumstances, there are significant discrepancies between the theory and the observations. To understand the reasons behind these discrepancies, the spatial and temporal variability of the energy flux is analyzed in Section 2.5. The possible sources of the discrepancies between the observations and the theory, as well as the spatial and temporal variability, are discussed in Section 4.6.

2.2 Data

The data were collected by two moorings deployed during the first SWIRM cruise from Mauritius to Durban in November 2007 and subsequently recovered during the second SWIRM cruise departing and returning to Durban in January 2008. Each mooring consisted of two McLane Moored Profilers (MMPs) (Morrison et al., 2000) that moved up and down in the water column, one in the top ($\sim 100 - 1300m$), and one in the
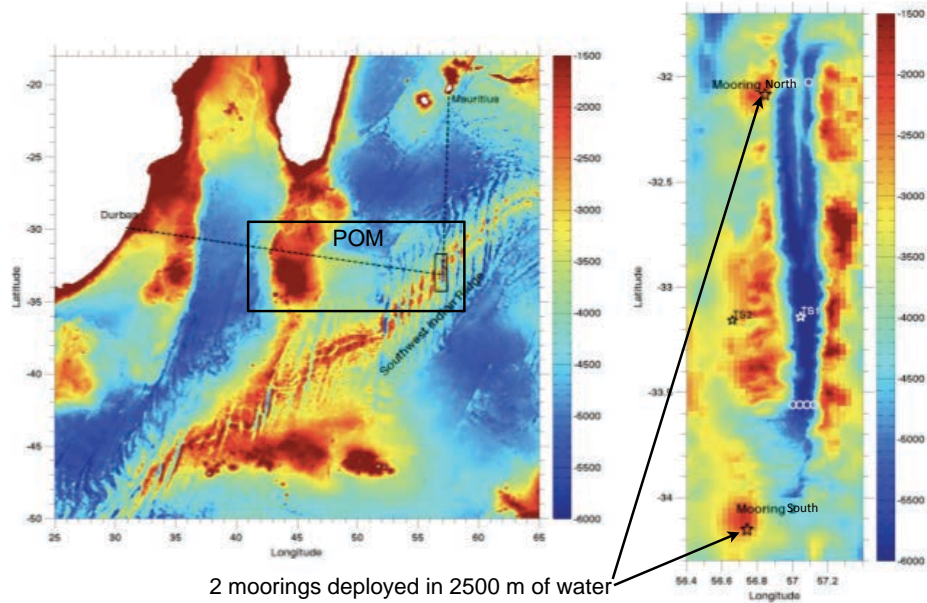
Figure 2.1 – Topography of the SWIRM study area. The large black box indicates the area where the Princeton Ocean Model was run before the experiment. The small black box is blown up on the right and the locations of the two moorings are indicated.

bottom ($\sim 1300 - 2500m$) of the water column. The MMPs, supplied by the Woods Hole Oceanographic Institution, were each equipped with a Falmouth Scientific Conductivity/Temperature/Depth (CTD) sensor as well as a Nortek Aquadopp Acoustic Current Meter (ACM). Each profile consisted of measurements spanning 1200 m every 2 hours. CTD and ACM data from the entire deployment were successfully recovered from the shallow water MMP at Mooring South, and for the first month of the deployment for the the shallow water MMP at Mooring North. Only CTD data were successfully collected from the deep water MMPs, along with some ACM data from the first few days of the deployment from the deep MMP of Mooring North. An enlarged view of the SWIRM study region in Figure 3.2 indicates the location of the two moorings.

Prior to the start of the field experiment, a model was run of the entire region to determine the best locations for the cruise and mooring deployments. The model, a Princeton Ocean Model (POM), an incompressible, hydrostatic Boussinesq model, was forced by the TPXO7.2 M_2 tide (Egbert et al., 1994) over the topography of the region. The SWIRM study area, including the region over which the POM was run, as well as an enlarged view of the region in which the two moorings were located, can be seen in Figure 3.2.

Observed velocity time series were obtained from ACM data interpolated onto an evenly-spaced time grid. Velocity plots in both the zonal and meridional directions show
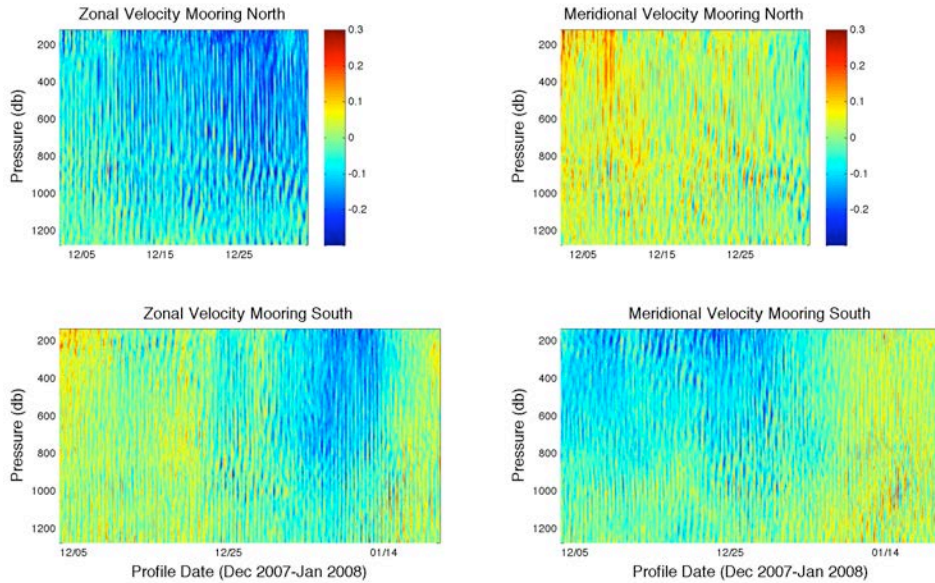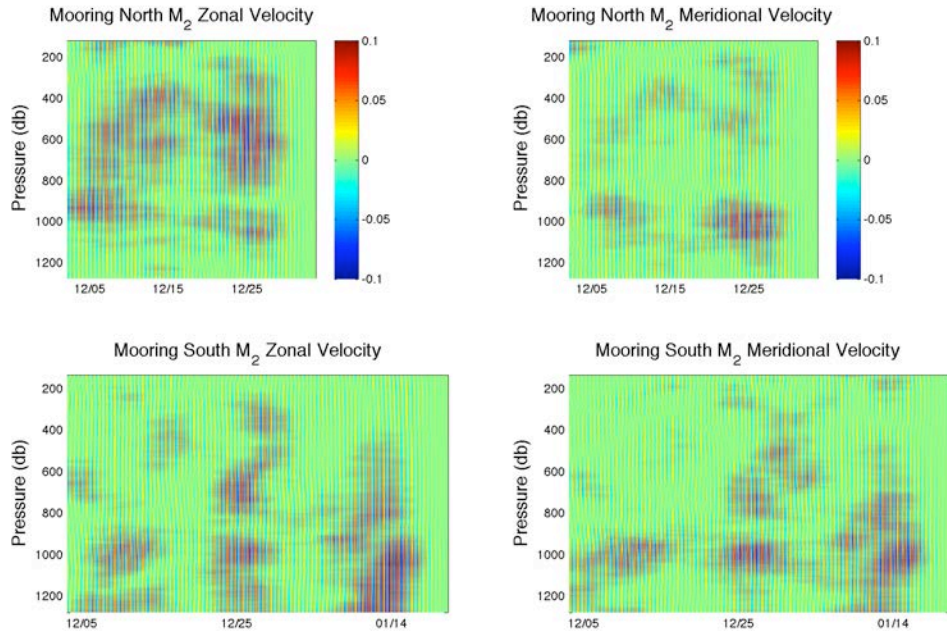
Figure 2.2 – Zonal (left) and meridional (right) velocities (m/s) at Mooring North (above) and Mooring South (below).

strong mesoscale currents, particularly at Mooring South, with energetic high-frequency motions superimposed (Figure 2.2). To determine at precisely which frequency these signals occur, the velocity time series were time windowed using a Kaiser-Bessel window, and then Fourier-transformed to obtain the horizontal kinetic energy spectrum at each depth. The spectra were then averaged together to yield the overall power spectra for the two moorings, as can be seen in Figure 2.3. The depth-averaged horizontal kinetic energy spectra reveal the motions evident in the time series to be a combination of motions with the local inertial frequency (Figure 2.3 black lines) and those with the semidiurnal frequency (Figure 2.3 green line). The 95% confidence intervals (magenta lines) indicate data that falls within 95% of a chi-square distribution.

The M_2 tidal frequency, being the strongest signal in the velocity data, has been isolated using a Chebychev type II filter. The filtered time series reveal a high-mode vertical structure, with the strength of the signal varying with depth and with the spring-neap cycle (Figure 2.4).

The observed internal tide time series are then compared to the model output, which similarly reveals a strong tidal signal, but, since it is forced only by the M_2 tide flowing over the rough topography of the ridge, does not reproduce the spring-neap cycle seen in the observations. The model also effectively reproduces the high-mode vertical structure of the internal tide seen in the observations, indicating that the topography is most likely responsible for the strong tidal signal seen at various depths in the observed time series.

2.3 Mechanical Energy

To investigate further the high-mode vertical structure seen in the velocity time series, the spatial and temporal variability of the mechanical energy of the system is analyzed, both for the observations as well as for the model.

The kinetic energy (KE) density has been calculated using the average horizontal velocities filtered around the M_2 tidal frequency, and the potential energy (PE) density,
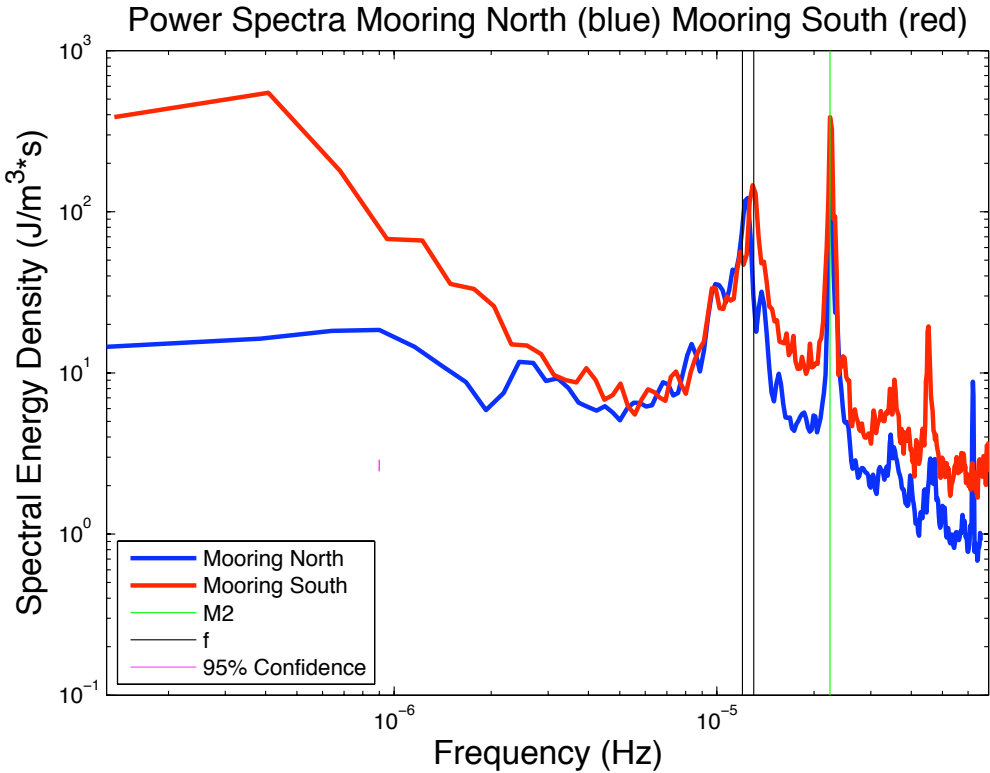
Figure 2.3 – Power spectra of kinetic energy. Mooring South (red) shows a much greater mesoscale (low) frequency signal than Mooring North (blue). The dominant peak for both moorings is at the M_2 frequency (green). There are also strong peaks at the inertial frequencies for each mooring (black).

Figure 2.4 – Zonal (left) and meridional (right) velocities (m/s) filtered around the M_2 frequency at Mooring North (above) and Mooring South (below).

$\frac{1}{2}\eta^2 N^2$, using the filtered isopycnal displacements, $\eta = \rho'/\frac{d\rho}{dz}$, where ρ' is the perturbation from the time mean density at each depth, and $\frac{d\rho}{dz}$, the change in density with depth, where dz is 1 m. $\frac{d\rho}{dz}$ was found by dividing the Brunt-Vaisala frequency by g and multiplying by the average density, ρ_0. The spatial and temporal structure of PE and KE reveal high-mode vertical structures at both moorings, with areas of strong mechanical energy occurring at similar depths, for example at ~ 1000 m, in the water column, as can be seen in Figure 2.5. The overall mechanical energy observed at Mooring South, however, is stronger than that observed at Mooring North, and the mechanical energy is strongest at depths deeper than 1000 m at Mooring South, while the energy at Mooring North is strongest at depths shallower than 1000 m.

To compare the observed mechanical energy densities with that of the model, the KE for the model data is calculated in the same manner as that of the observations. Plots comparing the time-mean observed and model mechanical energies are shown in Figure 2.6. As can be seen in Figure 2.6, the magnitude of the observed and model KE are of roughly the same order, and the model also shows a high-mode vertical structure of KE, although the exact locations of the tidal beams are not identical. Since the location of the observed and modeled tidal beams are not in the exact same locations, the tidal beam ray paths must be influenced by outside factors, such as changes in stratification or the mesoscale, and are not solely dependent on the rough topography.

2.4 Tidal Beams

Both the kinetic and potential energy diagrams reveal regions of heightened tidal energy, areas where the tide has been focused into tidal beams. The energy diagrams reveal generally the points at which our time series intercepts these "tidal beams." To get a
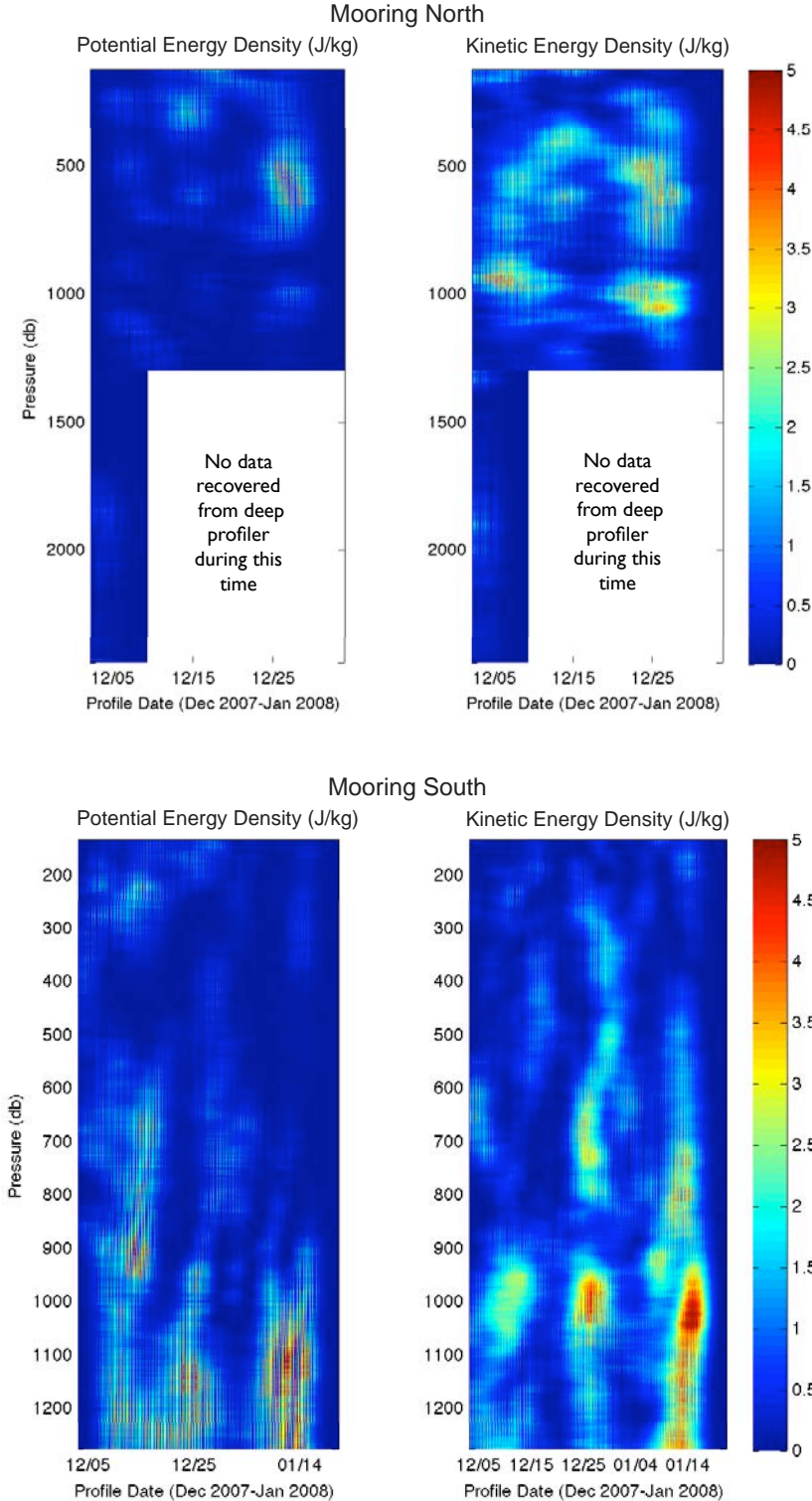
Figure 2.5 – Comparison of the potential versus kinetic energy densities Mooring North (above) and Mooring South (below)

Time Mean Observed and Model Energy Densities (J/kg)
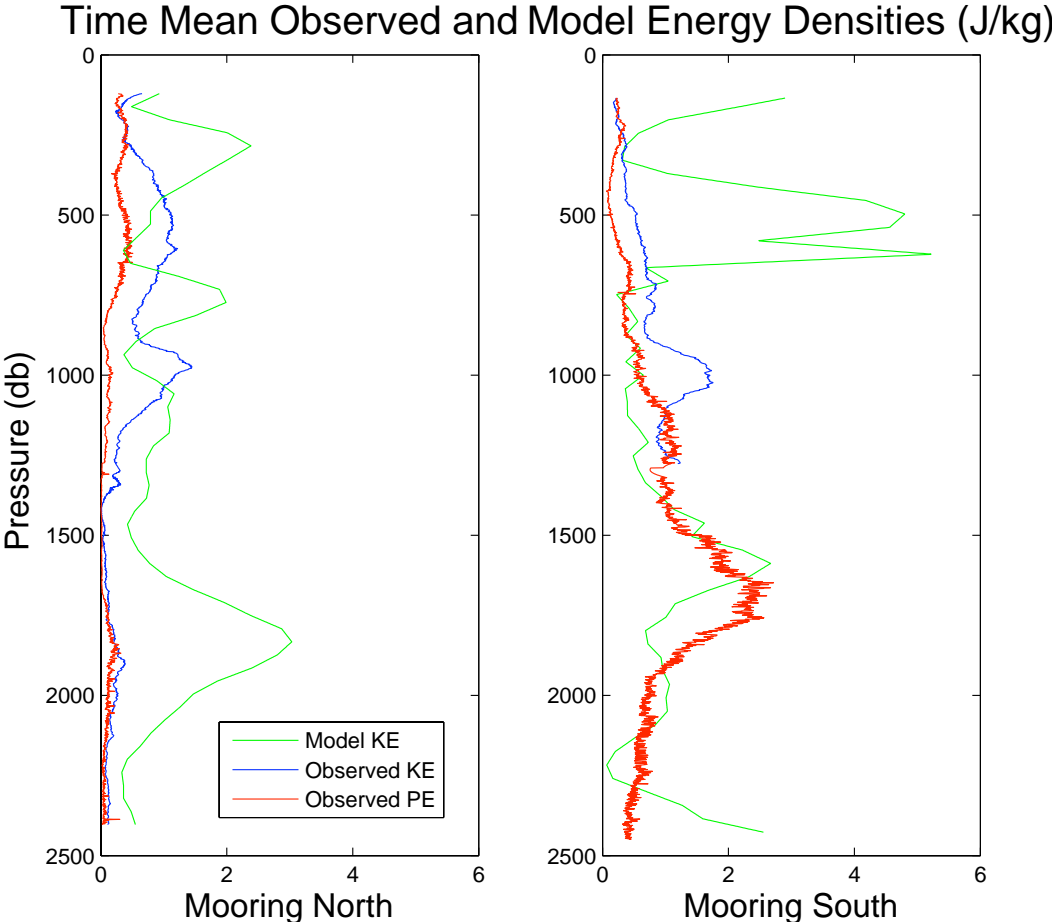
Figure 2.6 – Comparison of the time-mean averaged kinetic (blue) versus potential (red) energy densities Mooring North (left) and Mooring South (right) with the POM predicted kinetic energy density (green).

quantitative view of where the tidal beam interception points are spatially and temporally located, we look at where the total mechanical energy is elevated above a certain value, which we have set as ≥ 2 J/m^3 (Figure 2.7). As can be seen in Figure 2.7, the total mechanical energy observed at Mooring South is greater than that observed at Mooring North, and the areas of heightened energy occur lower in the water column for Mooring South.

After locating the interception points of the tidal beams, we determine the direction of the internal tide at these points, so that the ray path of each tidal beam can be traced through its intercept in the direction of the energy flux to its point of origin.

2.4.1 Energy Flux

To determine the direction of the internal tide, we calculate the energy flux, which, for a group of internal waves, is estimated as $< p'\mathbf{u}' >$, the covariance of the wave-induced pressure, p', determined from the density perturbation assuming a hydrostatic relation, and the velocity $\mathbf{u}'$, with the resultant values averaged over a discrete number of tidal periods (Nash et al., 2005). The wave-induced pressure p' was calculated by assuming a hydrostatic balance, $\frac{dp}{dz} = -\rho g$, and integrating the density perturbation filtered around the M_2 frequency. Since the data did not extend throughout the water column, the velocity data were projected onto normal modes. Figure 2.8 shows the variation of the energy flux in space and time, indicating the flux of the internal tide along both the meridional, $< p'\mathbf{v}' >$, and zonal, $< p'\mathbf{u}' >$, axes at each mooring.

The energy flux reveals great spatial and temporal variability in the direction of propagation of the internal M_2 tide. As can be seen in the top two plots of Figure 2.8, in the upper half of the water column at Mooring North, the M_2 energy flux goes from a northward direction to a nearly due west direction to a southeastward direction, except from 600-900 m, where instead of changing to a southeastward direction, it maintains its westward direction. In the lower half of the water column at Mooring North, for the short time period for which we have data, the semidiurnal energy flux goes from nearly due north from 1300 - 1400 m, varies from northwest to southwest from 1800 to 2300m, and is almost due south at the very bottom of the water column.

At Mooring South, shown in the bottom two plots of Figure 2.8, the direction of the energy flux changes from an eastward direction to a southeastward direction to a northeastward direction from the surface to about 600 m. From 600 m to about 1150 m, the flux direction varies from northeast to northwest. From about 1100 m to 1300 m, the bottom of our measurements, the energy flux has a southeastward direction.

Although the internal M_2 tide changes direction in space and time, each tidal beam is associated with one specific direction. Once the direction of each of the tidal beams at their precise location in space and time has been determined, the path of the tidal beams through these points is calculated, so each tidal beam can be traced back to its point of origin.

2.4.2 Ray Paths

To trace the tidal beams back to their point of origin, the ray paths for the tidal beams are determined using the inverse slope of the internal tide at each mooring:

$$\frac{dx}{dz} = \sqrt{\frac{N^2 - \omega^2}{\omega^2 - f^2}},$$

which is derived from the internal wave dispersion relation, where ω is the M_2 tidal frequency. To plot the ray paths, a simple iterative method was used, multiplying the inverse ray slope, $\frac{dx}{dz}$, by the step in z, $dz = $ (pressure in $db * 1.019716\frac{m}{db}$)/110888.32$\frac{m}{\deg}$
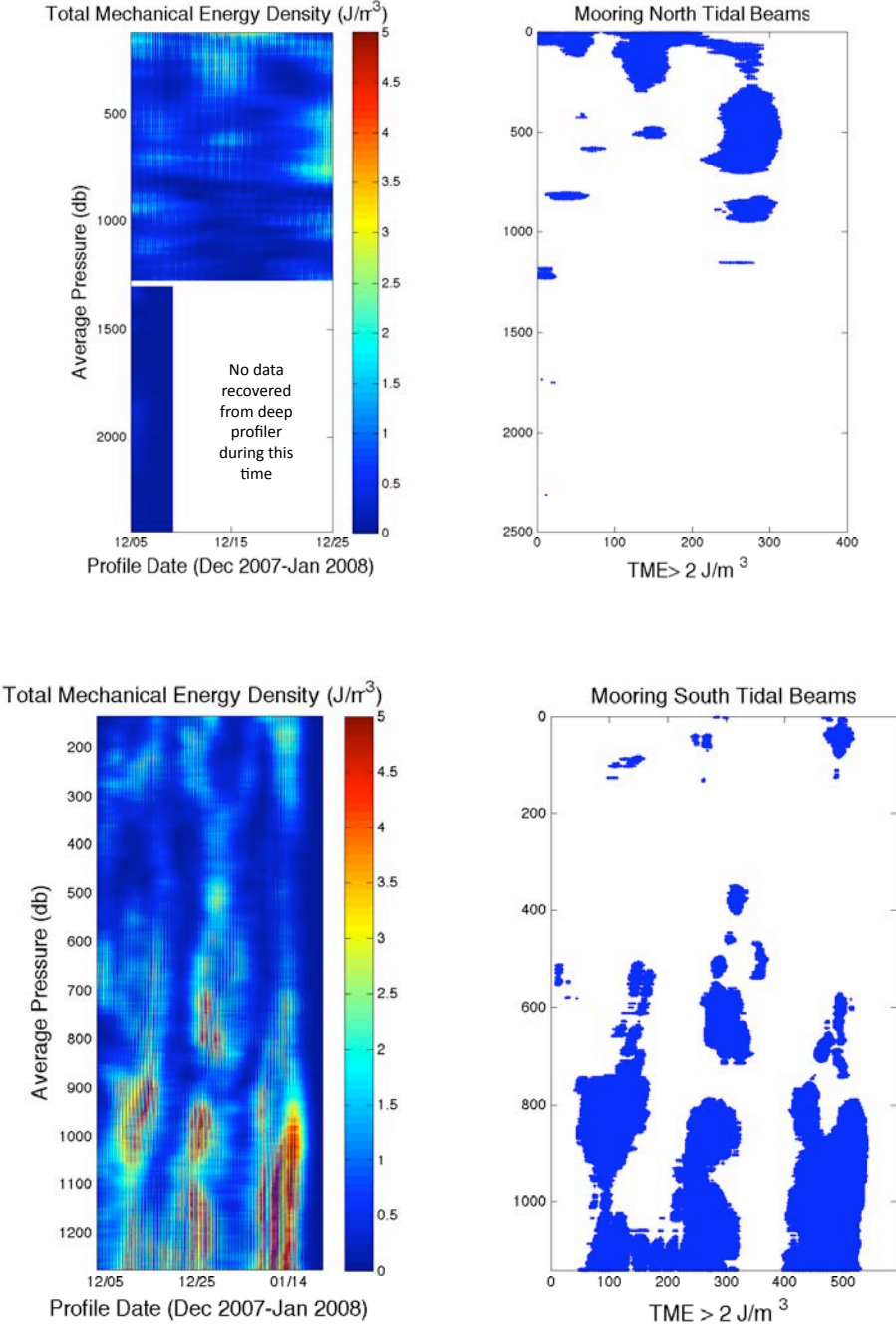
Figure 2.7 – Location of tidal beams based on exceeding a maximum total mechanical energy.
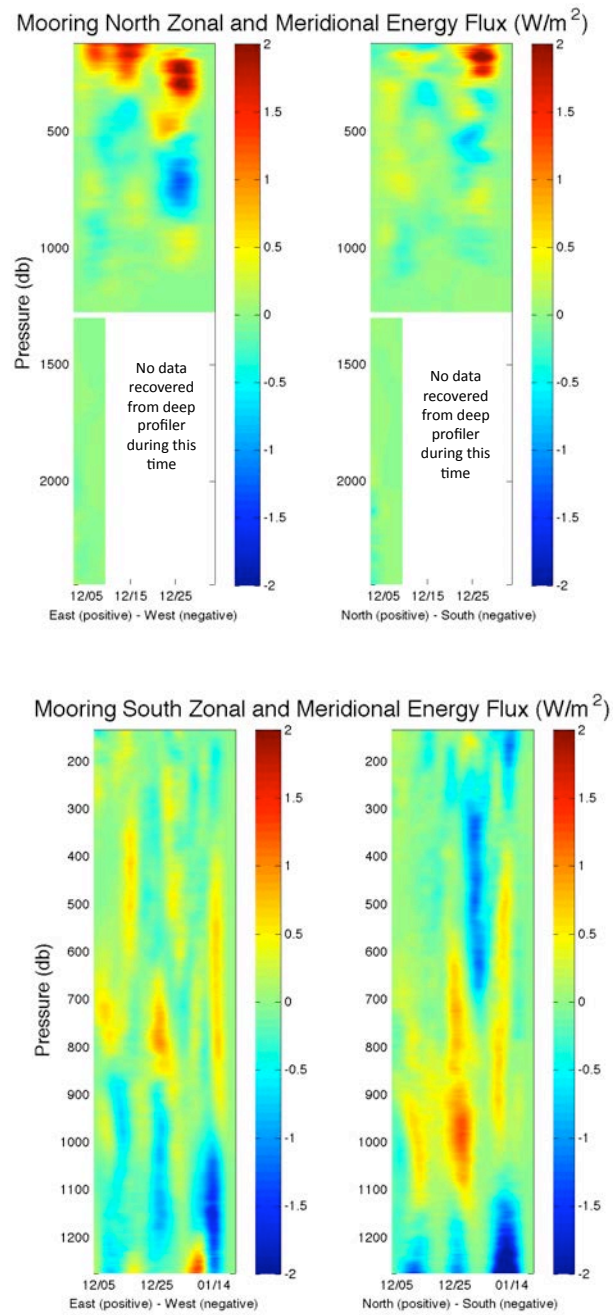
Figure 2.8 – Zonal (left) and meridional (right) energy flux at Mooring North (above) and Mooring South (below).

(length of one degree latitude at Mooring North) or $110925.12 \frac{m}{\text{deg}}$ (length of one degree latitude at Mooring South) and adding the step in dx to the previous position.

The direction of the tidal beam ray paths was then determined by taking the arctangent of the meridional over the zonal energy flux, $\frac{p'\mathbf{v}'}{p'\mathbf{u}'}$, which yields the angle of the energy flux from east. This angle was then used to plot the ray paths on the topography. The starting point for the rays was chosen to coincide with the average depth of the tidal beams, defined by our criteria TME $\geq 2\ J/m^3$, seen at each mooring, which was found by taking the maximum of the average TME. Starting from this intercept at each mooring, the tidal beam rays were traced back in the direction of the energy flux to find their point of interception with the bottom topography.

2.4.3 Theoretical Generation

The conversion from barotropic to baroclinic energy is theoretically determined by the amount of power available to go into the internal tide. The theoretical power available for conversion can be calculated as the product of the Baines (1982) Force $F_b = N^2 w_{bt} \omega^{-1}$ and the vertical component of the barotropic velocity $w_{bt} = \mathbf{u_{bt}} \cdot \nabla \mathbf{H}(z/H)$:

$$F_b w_{bt} = \frac{N^2 w_{bt}^2}{\omega} = \frac{N^2 [\mathbf{u_{bt}} \cdot \nabla \mathbf{H}(z/H)]^2}{\omega},$$

where N^2 is the time-mean N^2 at each mooring for the top 2500 m combined with the N^2 from a nearby deep CTD cast taken during the cruise, $\mathbf{H}$ is the seafloor topography taken from Smith & Sandwell (1997), and the barotropic tidal velocity, $\mathbf{u_{bt}}$, comes from TPXO7.2 data (Egbert et al., 1994) interpolated onto the Smith & Sandwell (1997) topography.

The expected locations of internal tide generation are the sites where the barotropic tide does the most work on the topography. If we compare the locations where our observed ray paths intercept the topography with the theoretically-predicted sites of baroclinic generation, we see that there are certain tidal beam ray paths that intercept topography in the location of theoretical generation, and other ray paths whose points of interception do not coincide with theory, as demonstrated by the two examples in Figure 2.9. Some of the tidal beam raypaths, such as Tidal Beam N7, intercept the topography in locations of strong theoretically-predicted internal tide generation, such as the dominant feature to the west of Mooring North (Figure 2.9 left), whereas other tidal beam raypaths, such as Tidal Beam S4, intercept the topography in areas of little to no theoretically-predicted internal tide generation, such as the relatively weak topographic feature east of Mooring South (Figure 2.9 right).

While the ray-traced generation sites of several of our observed tidal beams are consistent with those predicted by Baines (1982) theory, including Tidal Beam N7 (Figure 2.9 left), the majority of baroclinic generation sites from our observed tidal beams and not consistent with theory. To compare the theoretical internal tide generation with the observed internal tide beams, we first look at the magnitude of the observed energy flux of our tidal beams compared with the theoretically-predicted magnitude. Following Nash et al. (2006), we first find the theoretical depth-integrated energy flux over the region of generation:

$$\Delta F_E = \int_{x_1}^{x_2} [\int_{-H}^{0} < F_b w_{bt} > dz] dx,$$

where we have set x_1 and x_2 as 10 km to either side of the point of intercept of our tidal beams with the topography. While the magnitude of the energy flux for our tidal beams does not coincide with the theoretically-predicted internal tide energy flux magnitude for all the tidal beams, for several specific tidal beams, the magnitudes of the observed and
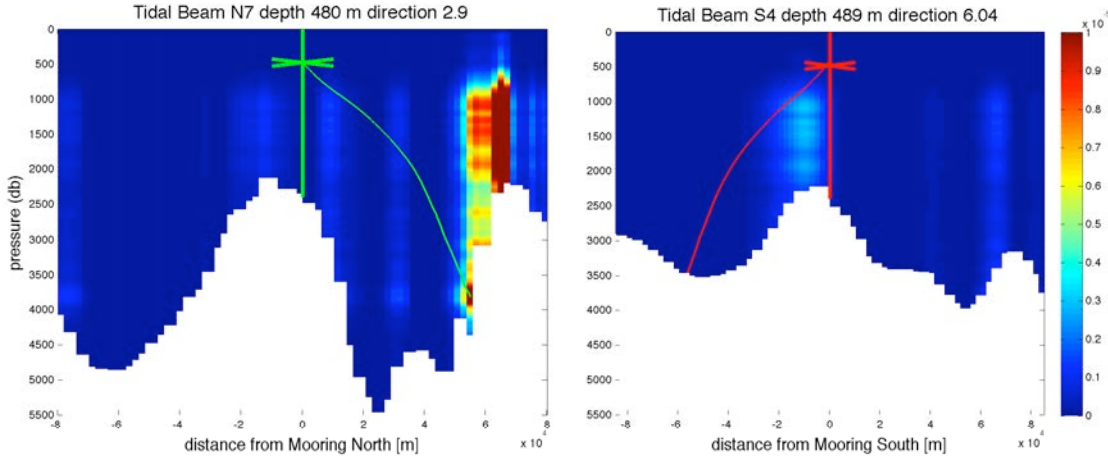
Figure 2.9 – Example tidal beam raypaths projected on a latitude slice in the direction of the tidal beam at Mooring North (left) and Mooring South (right). Colors represent magnitude of the rate of work of the barotropic tide on the topography (Baines, 1982). View is from north to south.

theoretical energy flux do coincide, as can be seen in Figure 2.10. All of the the Mooring South tidal beam energy flux magnitudes are significantly greater than the theoretical energy flux magnitudes, and none correspond to the theoretical flux values. Several of the Mooring North tidal beam energy fluxes, however, correspond well with the theoretical flux magnitudes, including Tidal Beams N10, N12, and the tidal beam from Figure 2.9 that intersects the dominant topographic feature west of Mooring North, Tidal Beam N7.

To determine which factors affect how well our tidal beam generation sites line-up with the theoretical generation sites, we compare the value of the rate of work of the barotropic tide at the point where our tidal beam ray paths intersect the topography to both the depth at which we observe our tidal beams, and the direction of the energy flux at that depth in Figure 2.11.

As can be seen in Figure 2.11, multiple tidal beams observed at Mooring North in the top of the water column, ranging from ~ 100 to $\sim 700\ m$, are consistent with theory. If we look at the angle of the direction of the energy flux of the tidal beams observed at Mooring North, we see that the majority of the tidal beams that agree with theory, including Tidal Beam N7 (Figure 2.9 left), originate due west of the mooring. Since most of the tidal beams at Mooring North that agree with theory come from the same direction, there is likely one common source of all these beams. While there are also tidal beams that agree with theory at Mooring South, these tidal beams do not occur at any specific depth or angle.

To figure out the source of these tidal beams that agree with theory, we look at the latitude slices for each of these tidal beams. All of these latitude slices reveal the same dominant feature as that seen in Figure 2.9 left, as the source of these tidal beams. If we look at the latitude slices for the Mooring North tidal beams that agree with theory, we see that they are all generated at the same strong topographic feature. As seen in Figure 2.9, this peak has a significant slope. To determine the significance of this feature, its slope is compared with that of the M_2 internal tide. We would expect internal tide generation to occur when the topographic slope is nearly equivalent to the wave ray slope. The ratio of the topographic slope to the wave ray slope, as defined in Baines (1986), is:

$$\gamma = \frac{\Delta H/\Delta y}{\alpha},$$
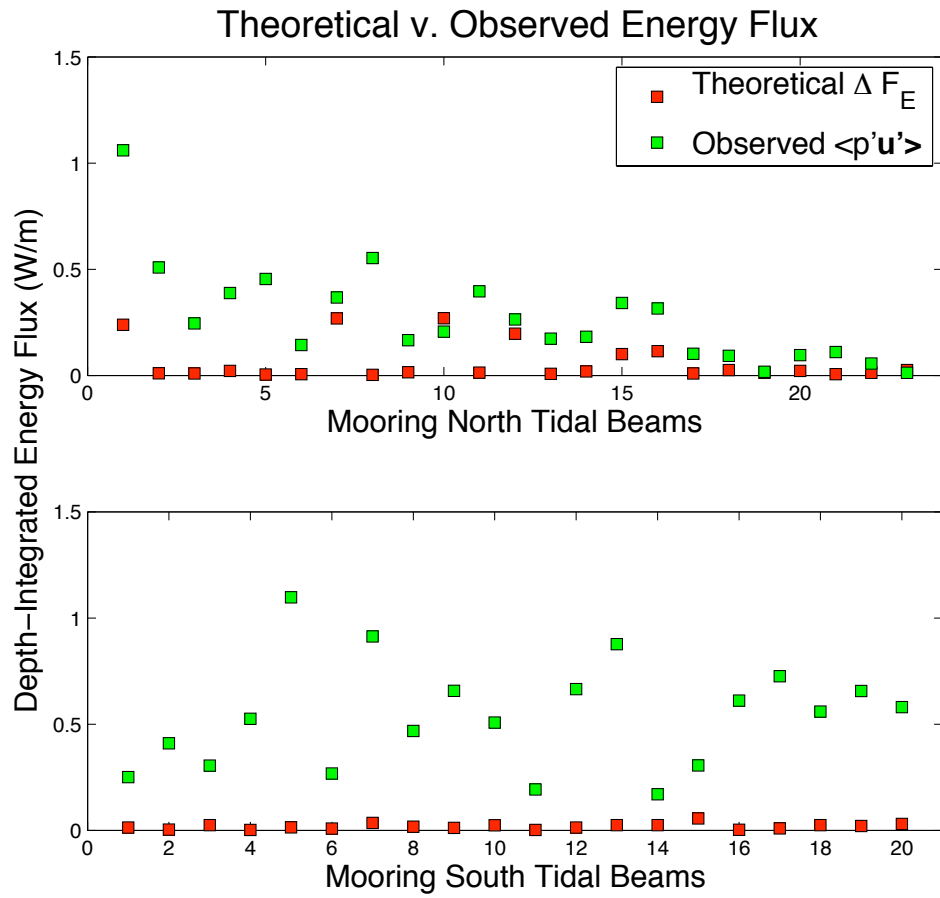
Figure 2.10 – Comparison of the value of the depth-integrated theoretical work done by the topography in converting barotropic to baroclinic energy (Baines, 1982) integrated across the intersection point of the observed tidal beams with the observed tidal beam energy flux for Mooring North (above) and Mooring South (below). While the observed energy flux is consistently stronger than the theoretical energy flux, the theory corresponds most closely with several observed tidal beams at Mooring North.
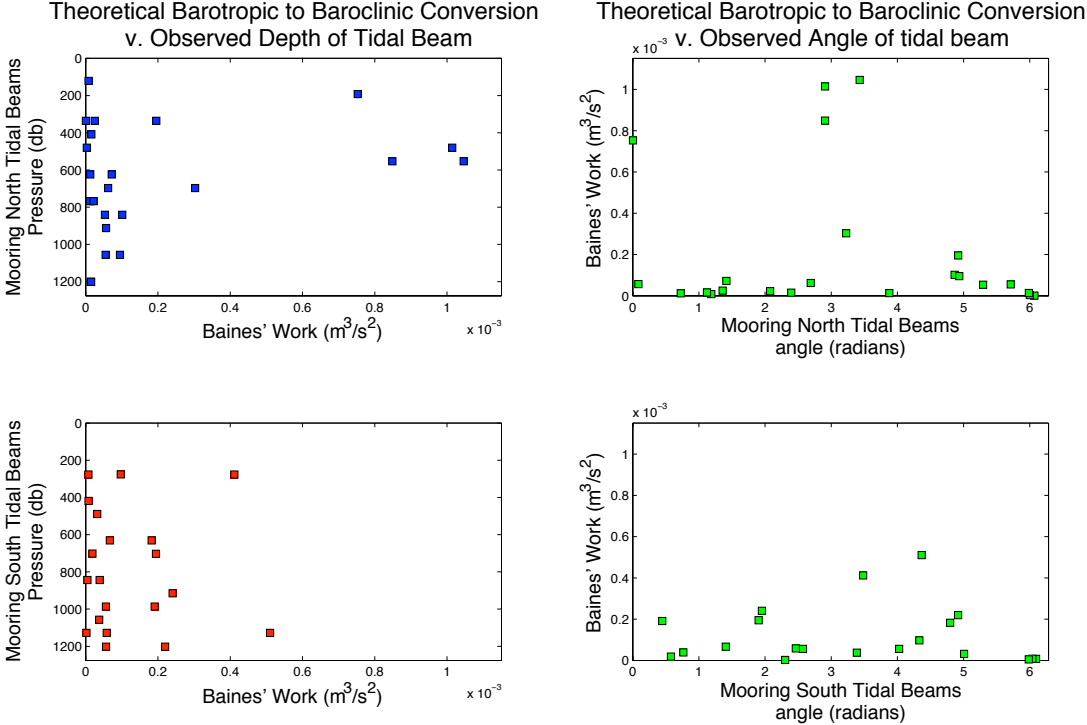
Figure 2.11 – Comparison of the value of theoretical work done by the topography in converting barotropic to baroclinic energy (Baines, 1982) at the intersection point of the observed tidal beams with the depth of tidal beams (left) and with the observed angles of tidal beams (right) for Mooring North (left) and Mooring South (right).
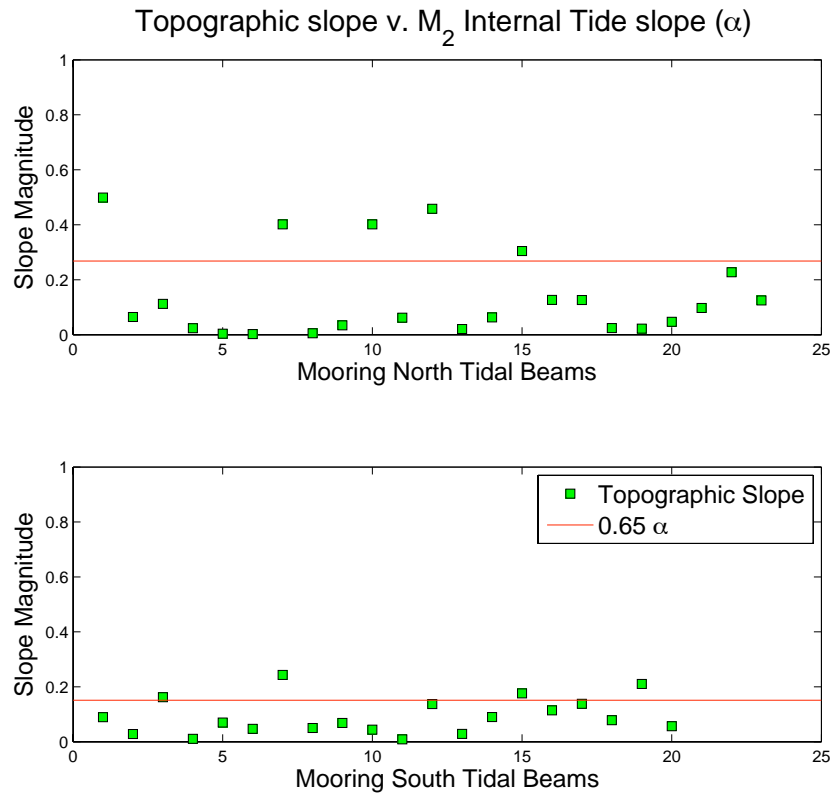
Figure 2.12 – Topographic slope at the point of interception for observed tidal beams (green squares) at Mooring North (above) and Mooring South (below). The red line indicates the value above which the observed interception points correspond to the theoretical internal wave generation sites, which we found to be 0.65 the value of the critical slope (α) at each mooring.

where $\alpha = \frac{dz}{dx}$ is the slope of the internal tide. According to Baines (1986), when the ratio of the topographic slope to that of the internal tide is between 0.5 and 2, the topographic slope is near critical, and internal tide generation is likely. We have found that when the topographic slope is greater than 0.65 α, the interception points of the ray paths of our observed tidal beams correspond to the theoretical generation sites. As can be seen in Figure 2.12, the topographic slope of the area near the interception of our tidal beam rays is greater than 0.65 α for five observed tidal beams at Mooring North, and four tidal beams at Mooring South. The interception points of the tidal beams that intercept near-critical topography, as defined by our criterium, $> 0.65\ \alpha$, correspond to areas of theoretical internal tide generation, as can be seen in Figure 2.9 left and Figure 2.13. Several tidal beams observed at Mooring North intercept near-critical topography, including Tidal Beam N7 (Figure 2.9 left) as well as three other tidal beams originating at the same dominate near-critical feature due west of the mooring, Tidal Beams N10, N12, and N15, as can be seen in Figure 2.13. All the tidal beams that can be traced back to near-critical topography ($> 0.65\alpha$) are consistent with the theoretical sites of generation.
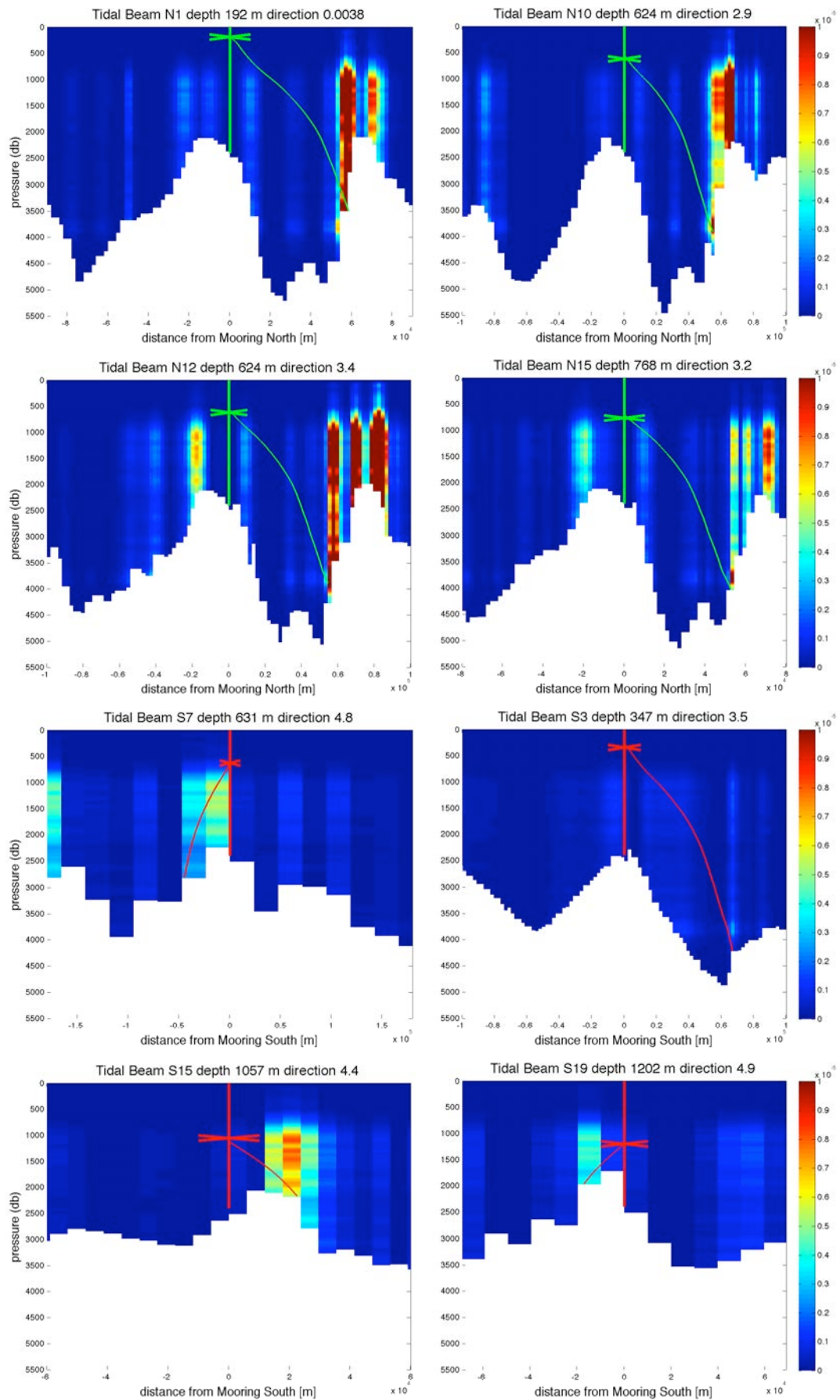
Figure 2.13 – Tidal beam raypaths with a topographic slope > .65 α at the point of interception projected on a latitude slice in the direction of the tidal beam at Mooring North (green ray paths) and Mooring South (red ray paths).

2.5   Space-Time Variability

To understand the reasons behind why some of the observed sites of internal tide generation are consistent with the theoretical sites while others are not, the spatial and temporal variability of the tidal beams is analyzed. From Figure 2.8, it is evident that the semidiurnal energy flux changes direction with space and time. To get a better idea of how the energy flux direction varies both spatially and temporally, we look at the time-mean (Figure 2.14) and the depth-mean (Figure 2.15) energy flux directions at each mooring.

The time-mean energy flux diagrams in Figure 2.14 reveal strong differences between how the observed energy flux varies with depth in both magnitude and direction at the two moorings. The magnitude of the energy flux at Mooring North is greatest in the top of the water column, whereas the magnitude of the energy flux at Mooring South increases with depth. The direction of the energy flux shifts significantly between the top and the bottom of the water columns at both moorings. At Mooring North, all the energy flux in the top of the water column comes from the southwest, whereas the energy in the bottom half of the water column comes from the east. The time-mean energy flux at Mooring South also changes direction with depth, but as opposed to the nearly bimodal pattern observed at Mooring North, the energy flux at Mooring South shows a gradual continuous shift to the left with depth.

To understand how these spatial changes in depth evolve in time, the water column is divided into eight depth regimes, and the temporal changes of the mean of each depth regime are plotted for each mooring in Figure 2.15. Figure 2.15 shows the dramatic decrease in energy flux with depth at Mooring North, and that the overall energy flux magnitudes at Mooring South are much greater than those at Mooring North. The most interesting feature of this plot is the shift in direction between the start of the time series and the end of the time series at Mooring North. Similarly, at Mooring South, the direction of the energy flux is not constant in time, but rather varies between the start, middle, and end of the time series.

In order to understand the source of this spatial and temporal variability in the observed energy flux, changes in stratification as well as mesoscale events were investigated. Changes in stratification during the course of our time series could cause the internal tide ray paths to change direction, and hence be linked to the spatial and temporal changes seen in the energy flux. As can be seen in Figure 2.16, however, the stratification at both Mooring North and Mooring South remained mostly unchanged throughout the time series, so temporal changes in stratification are not the cause of the observed temporal variability in energy flux.

Another possible cause of the spatial and temporal variability observed in the energy flux, as well as the reason why the observed tidal beam generation sites do not agree with the theoretical sites, could be due to spatial variability in the stratification, which would cause the tidal beam ray paths to change direction. In order to test this hypothesis, plots of the stratification taken during CTD casts at multiple points in the surrounding area during the two cruises are compared with the stratification at the two moorings. As can be seen in Figure 2.17, the stratification does not vary significantly among the various CTD casts and the moorings. Evidently, changes in stratification are not responsible for the spatial and temporal variability observed in the energy flux, nor for the differences between the observations and theory.

While the stratification did not change in space or time during our time series, changes in the mesoscale eddy field could also be responsible for the changes in the observed energy flux. In order to investigate this possible cause, sea surface height (SSH) phenomena based on SSH fields in the Aviso Satellite Altimetry Reference series (CNES, 2014) were analyzed. The SSH images, for which the images corresponding to the beginning and the
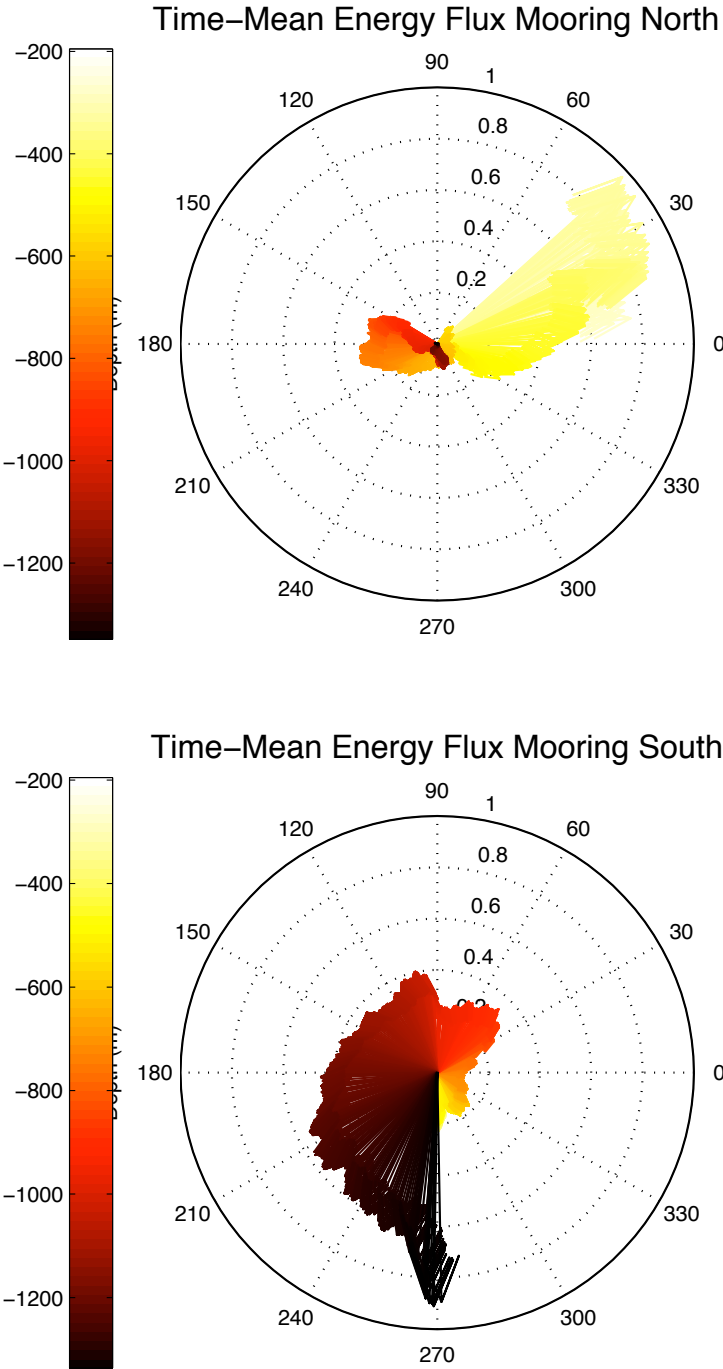
Figure 2.14 – Time-mean energy flux (W/m^2) at Mooring North (above) and Mooring South (below). The colors correspond to depth, with lighter colors at the surface, getting darker with increasing depth.

Depth-Mean Energy Flux Mooring North
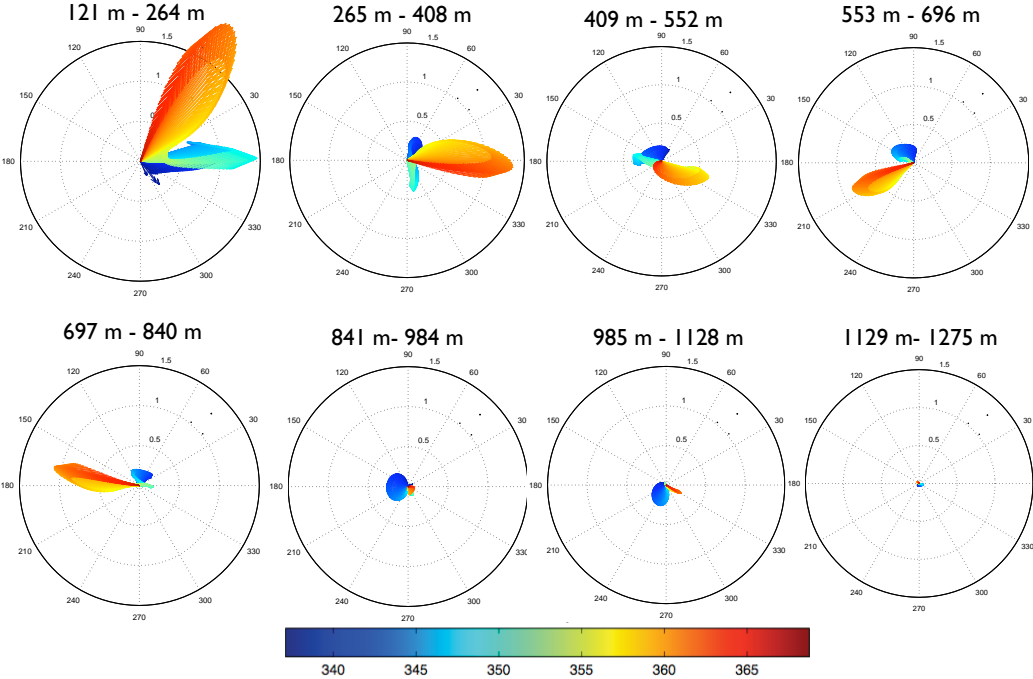
Depth-Mean Energy Flux Mooring South
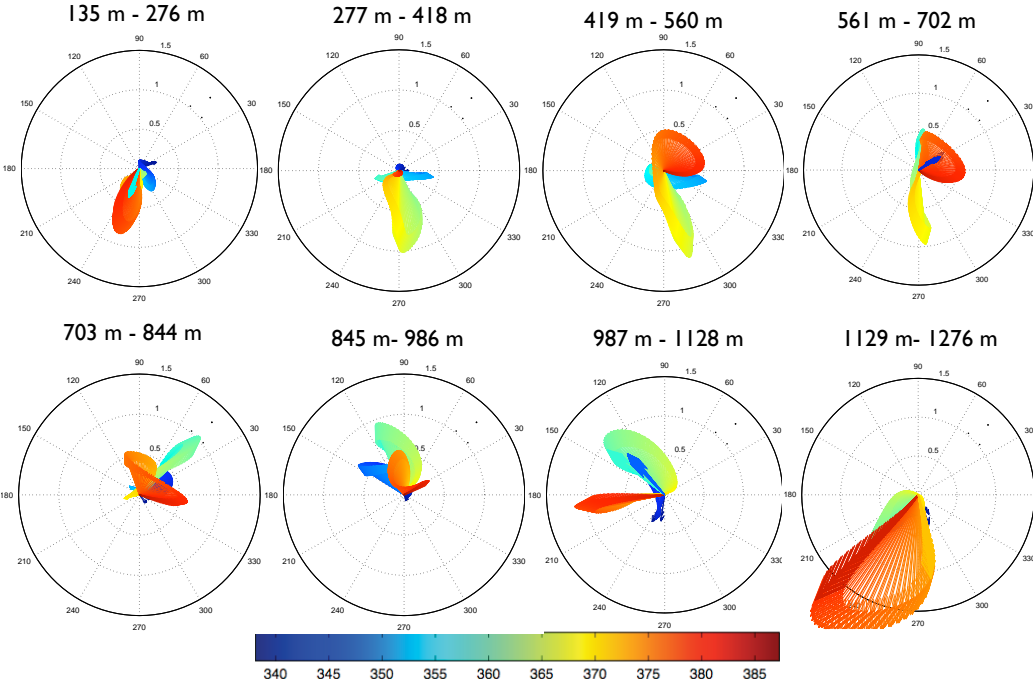
Figure 2.15 – Depth-mean energy flux (W/m^2) at Mooring North (above) and Mooring South (below)
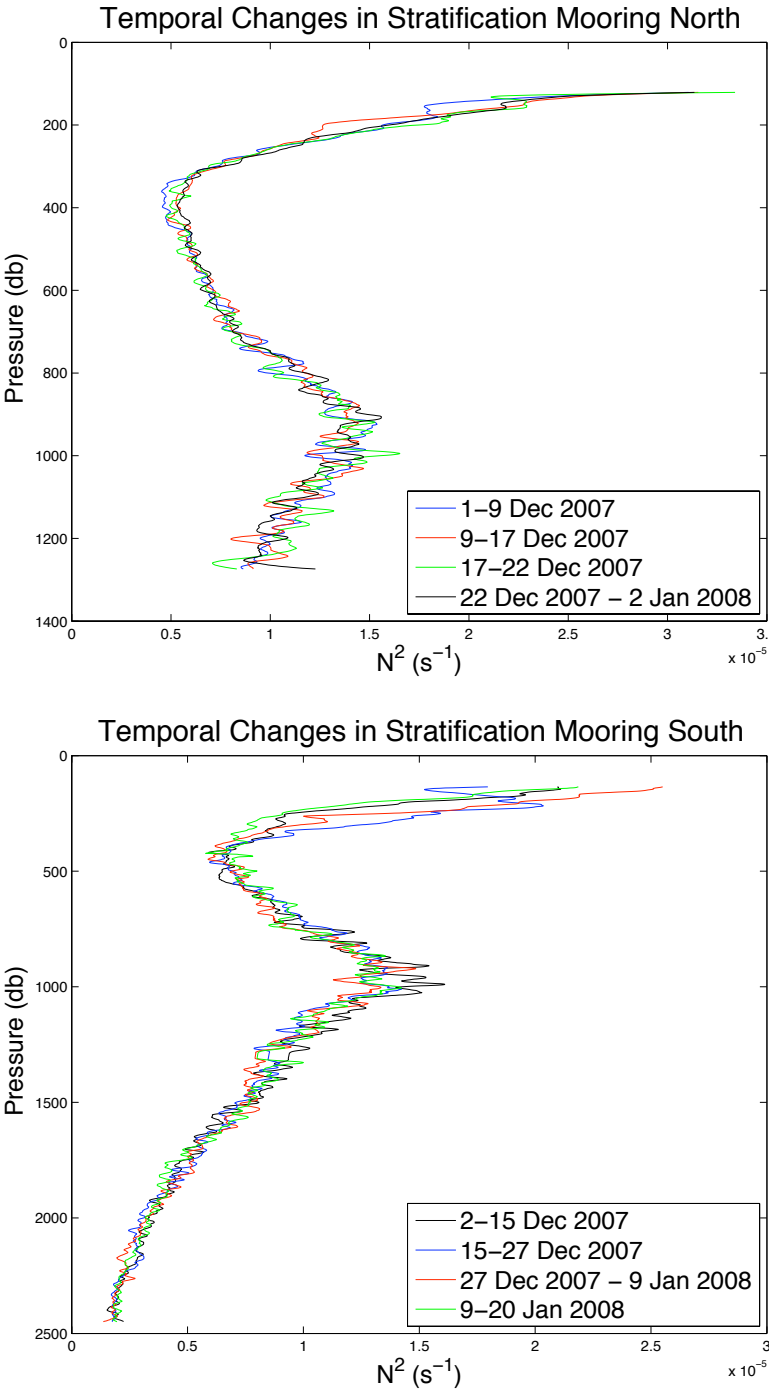
Figure 2.16 – Time-mean stratification ($N^2[s^{-1}]$) over several short time segments during the time series at Mooring North (above) and Mooring South (below).
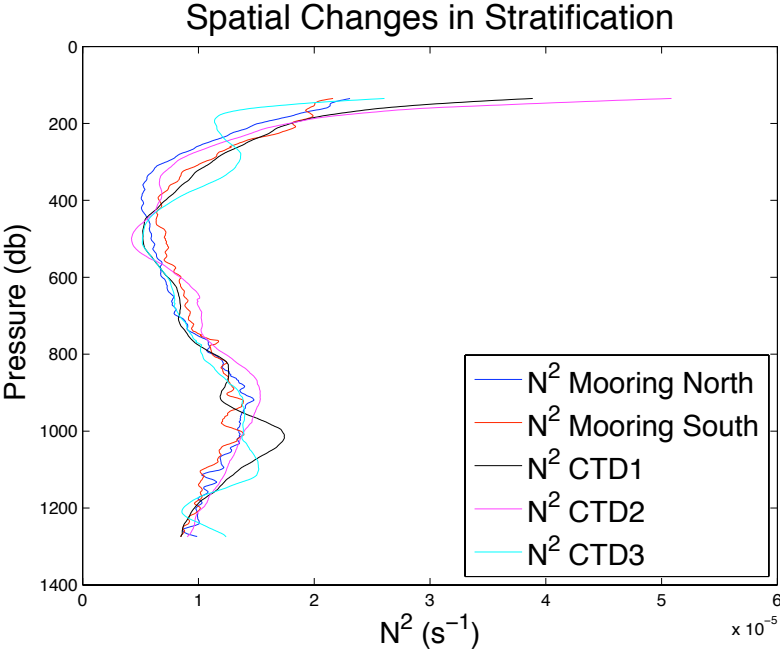
Figure 2.17 – Time-mean stratification ($N^2[s^{-1}]$) at Mooring North, Mooring South, and three CTD locations in the SWIRM study area.
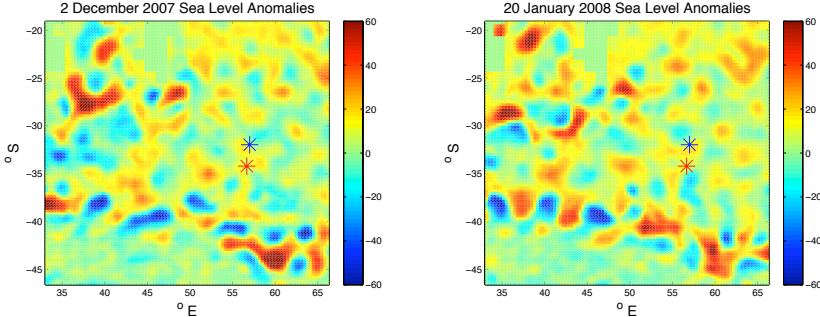
Figure 2.18 – Temporal variation in the mesoscale eddy field, shown here by changes in sea surface height anomalies (cm) between the beginning of our time series (left) and the end of our time series (right). Mooring locations are indicated by a blue star (Mooring North) and a red star (Mooring South).

end of our time series are shown in Figure 2.18, reveal significant spatial variability in the mesoscale phenomena. These images reveal heightened activity south of the moorings, which corresponds to the greater low frequency signal observed at Mooring South in comparison to Mooring North (Figure 2.3), and could contribute to the reasons why the observed and theoretical generation sites for the tidal beams of Mooring South do not coincide, there is little to no temporal variability during the course of our time series. The interaction between the internal tide and the mesoscale eddy field is most likely responsible for the spatial and temporal variation observed in the energy flux of the internal tide.

2.6   Summary and Discussion

To analyze the generation and propagation of the internal tide in an area of rough topography, we have looked at velocity and hydrographic data from two moorings in 2500 m of water on the western edge of the Atlantis II Fracture Zone located in the Southwest Indian Ridge. Both the velocity and hydrographic data from these two moorings reveal a high-mode vertical structure, indicative of focused tidal beams. Comparison with output data from the Princeton Ocean Model, run in advance of the experiment, forced by the topography and the M_2 semidiurnal tide, reveals similar vertical structure, indicating that the M_2 tide's interaction with the rough topography of the region is responsible for the observed tidal beams. While the model reveals a high-mode vertical structure, the location of the tidal beams is not identical to those observed at the moorings, implying that other factors influence the propagation of the observed tidal beams.

To quantify and isolate the tidal beams observed at the moorings, we set a criterium that defined a tidal beam as an area where the total mechanical energy $\geq 2 \; J/m^3$. Based on this criterium, we identified the locations of the tidal beams in the water column. Starting from the locations in the water column of these observed tidal beams, each beam was traced back to its point of interception with the topography, to determine the probable generation site of each beam. The ray path of the tidal beams was determined by the inverse slope of the M_2 tidal rays, derived from the internal wave dispersion relation and dependent on the stratification, and the direction of the ray paths was determined from the arctangent of the meridional over the zonal energy flux. Based on these factors, the observed tidal beams were traced back to their sites of probable generation.

Comparison between the observed sites of probable generation, and those predicted by Baines (1982) Theory, yields some correspondence for some specific tidal beams, but not for the majority of the tidal beams. When retracing the observed tidal beams back to their interception points with the topography leads to a dominant topographic feature, the observed tidal beam generation sites are consistent with Baines (1982) Theory. Most of the tidal beams at Mooring North that agree with theory, for example, have a similar angle of propagation. The times when the generation sites of the observed tidal beams at Mooring North agree with the generation sites predicted by Baines (1982) Theory for four out of five of the tidal beams, occur when the energy is coming from one dominant topographic feature, which explains why all the energy flux of these tidal beams at Mooring North comes from one specific angle. Mooring South, on the other hand, does not have a dominant angle at which the generation sites of the observed tidal beams line-up well with the theoretical generation sites. This difference can be attributed to the differences in the surrounding topography. While Mooring South does have some very strong topographic features in the surrounding area, it does not have a single dominant peak to consistently generate a baroclinic tide in one direction, as at Mooring North.

To quantify when the observed tidal beams are consistent with theory, we compared the topographic slope with the slope of the M_2 tide, α, and found that when the topographic slope is $> 0.65 \; \alpha$, the observed generation sites correspond to the those predicted by theory.

This empirically-determined cut-off corresponds to all of our observed tidal beams whose point of interception with topography lines-up with the theoretical point of generation.

To understand the differences between our two moorings, and why some tidal beams agree with theory while others do not, we looked a the spatial and temporal variability of the energy at each mooring. In this region of rough topography, the spatial and temporal variability of the energy flux of the internal M_2 tide is quite high, and there are striking differences between the two moorings. The magnitude of the energy flux at Mooring North decreases dramatically with depth, whereas the magnitude at Mooring South increases with depth. At Mooring North, all the tidal beams whose topographic intercept has a slope $> 0.65 \alpha$ and correspond to the theoretical generation sites, originate in the top of the water column ($\sim 100 - 700 \ m$) where the energy flux is the greatest. Mooring South, on the other hand, is more energetic than Mooring North, and all the tidal beams observed at Mooring South have greater energy flux than that predicted by theory. The fact that the energy is much higher at Mooring South, implies that the areas of heightened total mechanical energy $\geq 2 \ J/m^3$ are due not to a single tidal beam, but rather a construction of multiple tidal beams. The elevated low-frequency mesoscale signal observed at Mooring South, and corroborated by satellite data, most likely impacts the propagation of the internal tide observed at the mooring, allowing multiple beams to be focused in one area. We can assume that the tidal beams we observe have not merely been generated in one location, but rather have been bounced off several different topographic features and focused as tidal beams.

Our research indicates that in areas of rough topography with multiple ridges and crests, such as the Southwest Indian Ridge, only tidal beams which can be traced back to topography with a slope $> 0.65 \ \alpha$ can be assumed to have been generated at that generation site. A tidal beam traced to a topographic intercept $\leq 0.65 \ \alpha$ cannot be assumed to have originated at the intersection of its ray path with the topography, but rather must be assumed to have been reflected multiple times off the rough topographic features. The complexity of tracing the tidal beams in regions of rough topography requires more complex ray paths and modeling to determine the actual generation sites of the tidal beams, and, as is the case with our data, interacted with the mesoscale eddy field.

Changes in the mesoscale eddy field significantly impact the paths of our observed ray paths. As the internal tide interacts with the mesoscale eddies, the direction of propagation of the tidal beams alters significantly. The complexity of tracing the tidal beams in regions of rough topography and variable mesoscale activity requires more complex ray paths and modeling to determine the actual generation sites of the tidal beams.

Acknowledgments

Chapter 3

Internal Waves and Mixing Over the Southwest Indian Ridge

Abstract

A finescale pararmeterization based on shear and strain measurements obtained during WOCE campaigns indicated a high level of turbulent mixing above areas of rough topography (Kunze et al., 2006). One region of rough topography with particularly elevated estimated mixing was the area above the Southwest Indian Ridge, with heightened estimated mixing extending all the way to the surface (Kunze et al., 2006). Due to its location above a corrugated mid-ocean ridge, the heightened estimated mixing was assumed to be due to the internal tide. To pinpoint the source of this elevated mixing, two moorings were deployed in 2500 meters of water on the north and south ends of the western side of the Atlantis II Fracture Zone in the center of the ridge from December 2007 - January 2008 as part of the Southwest Indian Ridge Mixing Project (SWIRM). Each mooring was equipped with two McLane Moored Profilers, one in the top, and one in the bottom half of the water column, yielding time series throughout the water column. While overall velocity power spectra reveal a dominant M_2 internal tide signal, shear power spectra indicate a dominance of near-inertial shear. Mixing parameterizations are on the same order of magnitude as those predicted by Kunze et al. (2006), but show a spatial and temporal variability between the two mooring locations.

3.1 Introduction

Turbulent ocean mixing changes the distribution of physical water properties such as heat and salt, transforming water masses, and maintaining the ocean stratification necessary for the Meridional Overturning Circulation (Munk & Wunsch, 1998). While mixing is germane throughout the ocean, mixing intensity is not uniform. In order to better map the intensity of mixing throughout the ocean, we need ample measurements of mixing to cover the world's oceans. Direct measurements of mixing require costly ship-launched microstructure profilers, and are thus scarce. Measurements from CTDs and ADCPs, however, are much less costly and more abundant. While the scale of these measurements is much larger than the scale of the turbulence, both spatially and temporally, the larger-scale shear and strain from CTD and ADCP measurements can be used to estimate the smaller-scale turbulence, if we assume that the shear and strain at $10 - 100m$ scales is due to internal waves, and that the spectral shape of the internal wave field is in a steady state. The rate of turbulent dissipation can then be determined from the eikonal wave-wave interaction model and the assumption that the energy dissipation rate is primarily due to nonlinear internal wave interactions that transfer energy from the finescale $(10 - 100m)$
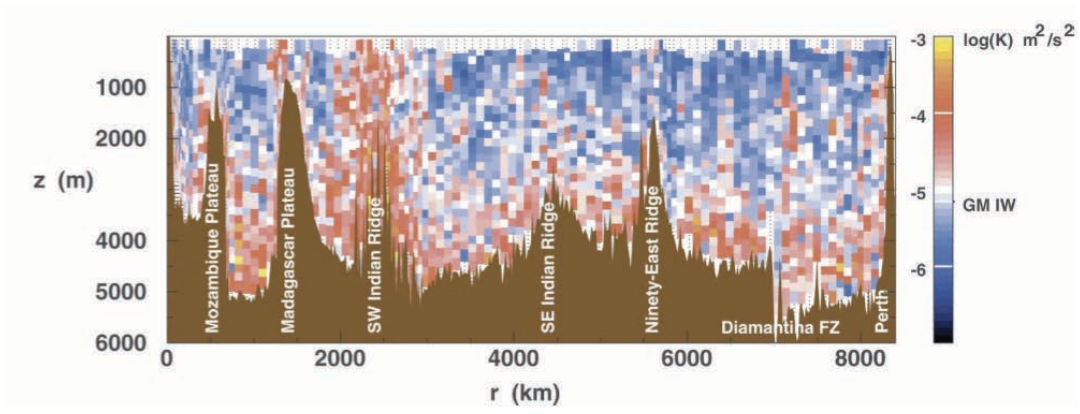
FIG. 7. Zonal section along 32°S (Fig. 4a). See Fig. 5 for details. Note that these profiles were not absolute because of lack of GPS information, and therefore absolute barotropic and 500-mab velocities could not be computed.

Figure 3.1 – Estimated diffusivities ($log_{10}(K)$) from Kunze et al. (2006)

towards the micro scale (cm) turbulence (MacKinnon & Gregg, 2003, 2005; Whalen et al., 2012).

Kunze et al. (2006) used shear and strain measurements from Lowered Acoustic Doppler Current Profiler (LADCP) and Conductivity/Temperature/Depth (CTD) data from the World Ocean Circulation Experiment (WOCE) and subsequent hydrographic cruises to approximate the mixing in different regions around the world. Originally from Gregg et al. (2003), the finescale parameterization used by Kunze et al. (2006) takes into account both the shear and strain in reference to the Garrett-Munk (GM) (Munk, 1981) spectrum in the following relation:

$$\kappa_{shst} = \kappa_0 \frac{<V_z^2>}{<V_{zGM}>^2} h(R_\omega) j(\tfrac{f}{N}),$$

where $\kappa_0 = 0.05 \times 10^{-4} m^2 s^{-1}$, and

$$h(R_\omega) = \frac{3(R_\omega+1)}{2\sqrt{2}R_\omega \sqrt{R_\omega-1}}$$

and,

$$j(\tfrac{f}{N}) = \frac{f arccosh(N/f)}{f_{30} arccosh(N_0/f_{30})}$$

$f_{30} = f(30^o)$, and $N_0 = 5.2 \times 10^{-3} rad/s$. The shear-strain variance ratio

$$R_\omega = \frac{<V_z^2>}{N^2<\zeta_z^2>}.$$

for the GM frequency spectrum, $R_\omega GM = 3$.

Based on this finescale parameterization of the WOCE data, Kunze et al. (2006) mapped out varying mixing intensities across the world's oceans, and found elevated turbulent mixing above areas of rough topography. Numerical models in areas of rough topography such as the Mid-Atlantic Ridge (hereinafter MAR) (e.g. Zilberman et al., 2009; Dovgaya & Cherkesov, 1996) show a strong internal tide generation. Observations along the rough topography of the MAR, near the Brazil Basin by Polzin et al. (1997), indicate that the enhanced mixing observed above the MAR is due to the breaking of this strong internal tide. Jayne & St. Laurent (2001) attribute the mixing above areas of rough topography to the internal tide. Along with the local effects of the internal tide on mixing,

the internal tide has also been assumed to affect mixing on a global scale. Based on a global energy budget, Munk & Wunsch (1998) infer that the energy required for mixing could come from the tide interacting with rough topography.

One site with particularly highly-elevated estimations of mixing with mixing elevated orders of magnitude and extending all the way to the surface, is an area of rough corrugated topography, the Southwest Indian Ridge (Figure 3.1). The Southwest Indian Ridge is a slow-spreading ridge separating the Antarctic and African plates that is characterized by steep valleys and rough topography, as depicted in Figure 3.2. WOCE reanalysis data indicate that turbulent diapycnal mixing is elevated orders of magnitude above background levels over the rough topography of the ridge (Kunze et al., 2006). Based on the numerous previous observational, numerical, and theoretical studies that showed mixing above rough topography to be due to the internal tide, it was assumed that the internal tide was responsible for the heightened mixing above the Southwest Indian Ridge.

To analyze this area of heightened mixing, two moorings were deployed from December 2007 - January 2008, on the western crest of the Atlantis II Fracture Zone, a steep-walled canyon in the center of the Southwest Indian Ridge, as shown in Figure 3.2, as part of the Southwest Indian Ridge Mixing Project (SWIRM). The moorings, each consisting of two McLane Moored Profilers, one in the upper, and one in the lower half of the water column, were deployed on the north (hereinafter Mooring North) and the south (hereinafter Mooring South) end of the western side of the fracture zone. The profilers collected temperature, conductivity, and current meter data which provide a long-term record of tidal variability.

This paper analyzes the predicted turbulent mixing due to the shear and strain observed by the two moorings. Section 4.2 describes how the data are collected, Section 4.5 shows the turbulent diapycnal mixing predicted from the shear and strain data, and Section 3.4 analyzes the possible sources of this heightened mixing. The results are discussed in Section 4.6.

3.2   Data

The data were collected by two moorings deployed during the first SWIRM cruise from Mauritius to Durban in November 2007 and subsequently recovered during the second SWIRM cruise departing and returning to Durban in January 2008. Each mooring consisted of two McLane Moored Profilers (MMPs) (Morrison et al., 2000) that moved up and down in the water column, one in the top ($\sim 100 - 1300m$), and one in the bottom ($\sim 1300 - 2500m$) of the water column. The MMPs, supplied by the Woods Hole Oceanographic Institution, were each equipped with a Falmouth Scientific Conductivity/Temperature/Depth (CTD) sensor as well as a Nortek Aquadopp Acoustic Current Meter (ACM). Each profile consisted of measurements spanning 1200 m every 2 hours. CTD and ACM data from the entire deployment were successfully recovered from the shallow water MMPs for both Mooring North and Mooring South, but only CTD data were successfully collected from the deep water MMPs, along with some ACM data from the first few days of the deployment from the deep MMP of Mooring North. An enlarged view of the SWIRM study region in Figure 3.2 indicates the location of the two moorings. ACM velocity data can be seen in Figure 3.5.

3.3   Mixing Estimation

To quantify the turbulent mixing at each mooring, we look at how quickly the turbulent kinetic energy is dissipating. This local turbulent dissipation is responsible for mixing of the water column, which changes the distribution of physical water properties
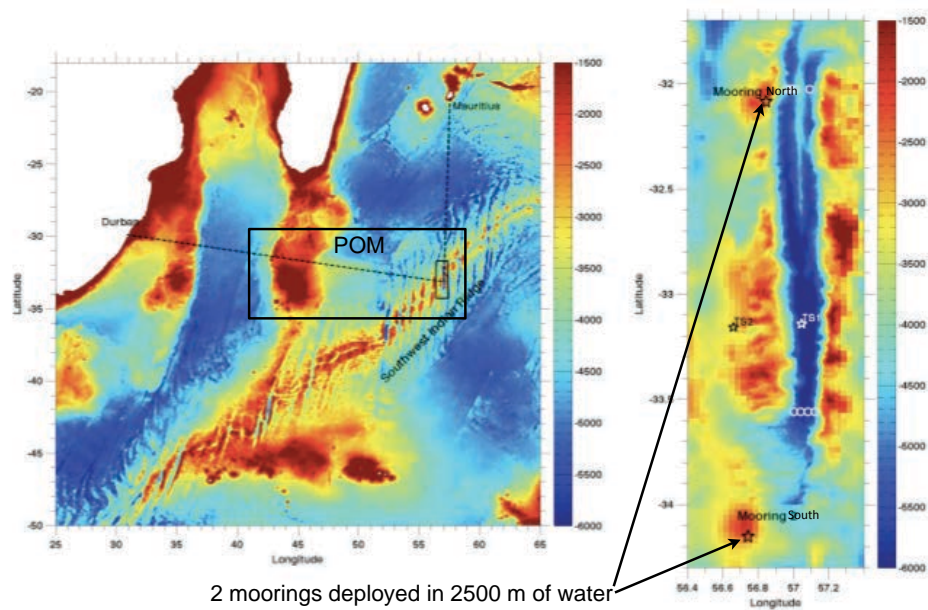
Figure 3.2 – Topography of the SWIRM study area. The large black box indicates the area where the Princeton Ocean Model was run before the experiment. The small black box is blown up on the right and the locations of the two moorings are indicated.
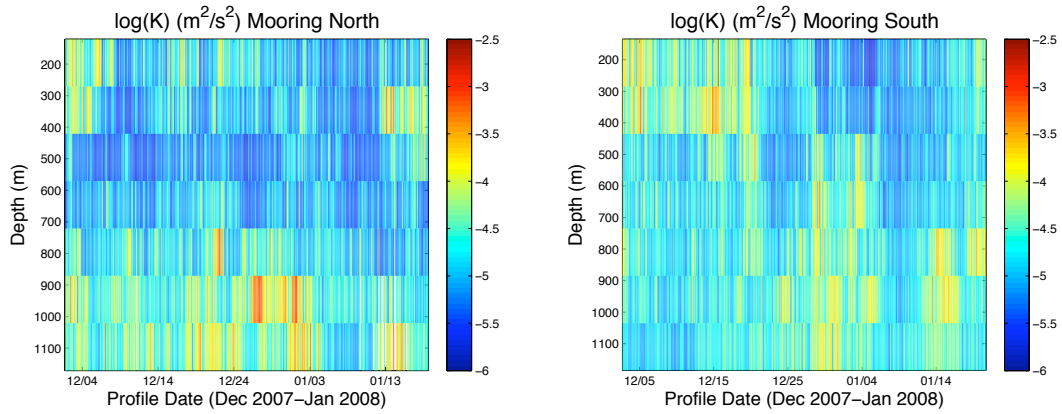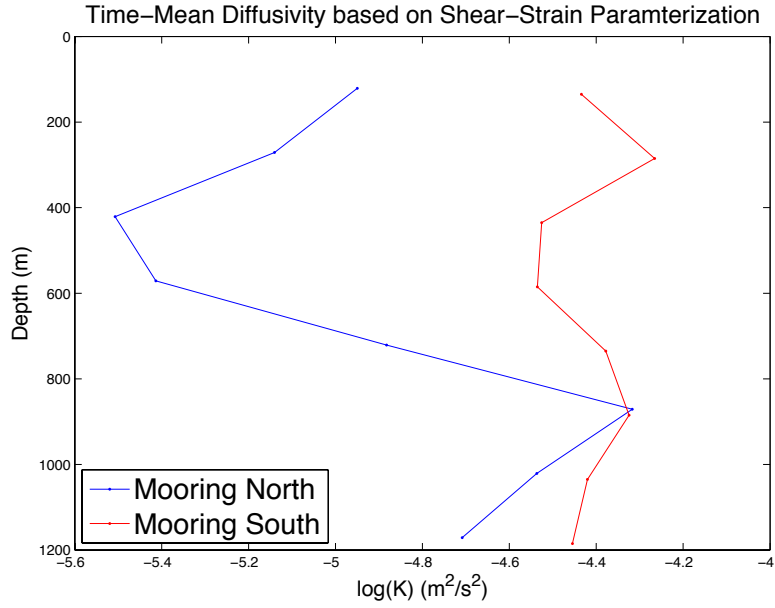
Figure 3.3 – log_{10} of the diffusivity (κ_z) at Mooring North (right) and Mooring South (left) based on the Kunze et al. (2006) shear/strain parameterization.

such as heat and salt. The rate of turbulent kinetic energy dissipation can be found by direct measurement, using microstructure profiles, or estimated indirectly, using larger-scale quantities such as stratification and shear to parameterize the mixing. In the absence of microstructure measurements, we use a shear/strain finescale parameterization to get an estimate of the turbulent dissipation rate.

In order to approximate the turbulent diapycnal mixing at our moorings, we look at the Kunze et al. (2006) shear and strain parameterization. While the internal M_2 tide is the dominant signal in the data (Figure 3.6), the shear is due mostly to the inertial f frequency (Figure 3.8). The average observed diffusivities are on the same order as those predicted by Kunze et al. (2006), with average values ranging from 10^{-4} to 10^{-5} m^2/s^2 for both moorings. While Kunze et al. (2006) predicts turbulent diffusivities on the order of 10^{-4} m^2/s^2 throughout the water column (Figure 3.1), our data shows inhomogeneous mixing varying from 10^{-6} to $10^{-2.5}$ m^2/s^2 throughout the water column for both Mooring North and Mooring South, with overall stronger diffusivities observed at Mooring South than at Mooring North (Figure 3.3). While stronger diffusivities are observed consistently near the bottom of the sampled water column at Mooring North, the diffusivities at Mooring South are less depth-dependent, but rather vary temporally, with heightened diffusivities in the top of the water column for the first third of the time series, and then switching to the bottom of the water column for the last two thirds of the time series, possibly related to the spring-neap cycle of the internal tide (Figure 3.3).

3.4 Sources of the Mixing

3.4.1 Velocity

To determine the source of this elevated estimated mixing, we look at the source of the finescale shear and strain used to parameterize the mixing. Since the shear is the change in velocity with depth, $\frac{d\mathbf{u}}{dz}$, we look at the velocity data to determine the source of the shear.

The velocity time series from the from both Mooring North and Mooring South reveal a streaky pattern with peaks every approximately 12 hours, indicative of a strong semidiurnal tidal signal, as can be seen in Figure 3.5. The velocity time series also show a lower-fequency about fortnightly signal, indicative of a spring-neap cycle. This spring-neap cycle is more evident at Mooring South than Mooring North, as can be clearly seen by the variation between yellow and blue in lower plots of Figure 3.5.

Figure 3.4 – log_{10} of the time-mean diffusivity (κ_z) at Mooring North (blue) and Mooring South (red) based on the Kunze et al. (2006) shear/strain parameterization.
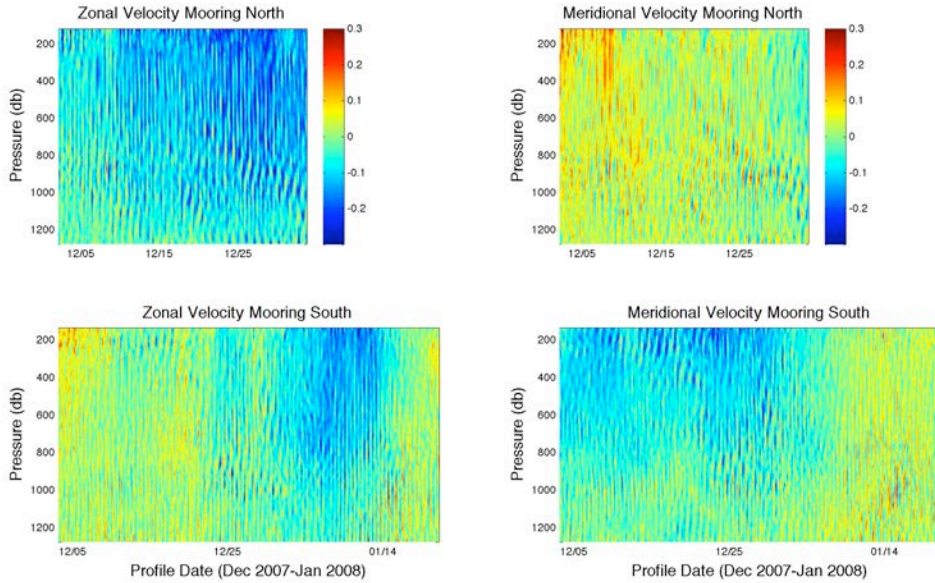
Figure 3.5 – Zonal (left) and meridional (right) velocities (m/s) at Mooring North (above) and Mooring South (below).
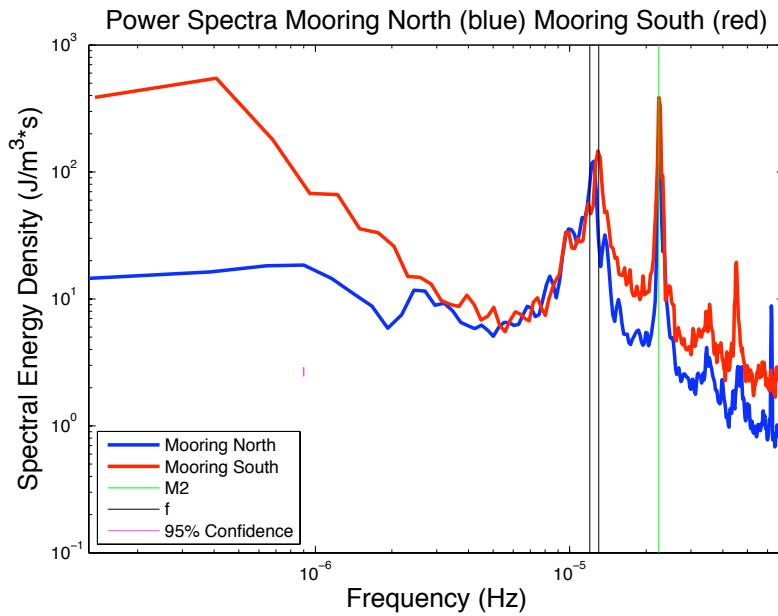
Figure 3.6 – Power spectra of kinetic energy. Mooring South (red) shows a much greater mesoscale (low) frequency signal than Mooring North (blue). The dominant peak for both moorings is at the M_2 frequency (green). There are also strong peaks at the inertial frequencies for each mooring (black).

To more accurately identify the signals in the velocity time series, we Fourier transform the velocity time series to identify the different frequencies. The Fourier transform of the velocity signal at each depth is then averaged to provide a depth-averaged power spectra at each mooring, shown in Figure 3.6. As can be seen in the plot of the power spectra (Figure 3.6), while there are contributions from low-frequency mesoscale inputs, particularly at Mooring South, as well as near-inertial (f) waves at both moorings, the semidiurnal M_2 tide is the strongest signal in the velocity time series. The fact that the internal tide signal is the greatest signal in the velocity data, lines up with the assumption that the elevated mixing in this region is due to the internal tide.

3.4.2 Shear

While the fact that the velocity data is dominated by the internal tide implies that the tide is responsible for the elevated mixing, to more accurately identify the source of the estimated mixing, we look at the shear itself. The shear, the spatial gradient of the velocity in a direction normal to its direction, $\frac{d\mathbf{u}}{dz}$, destabilizes the water column, possibly leading to instabilities and turbulent mixing. The shear, normalized by the Brunt-Vaisala frequency, N, is shown in Figure 3.7.

To identify which components of the velocity contribute the most to the shear, we Fourier transform the shear. The depth-average of the shear spectra is shown in Figure 3.8. As can be seen in Figure 3.8, while there is a definite semidiurnal tidal signal in the shear signal, the dominant signal is in fact the near-inertial signal. So while the velocity was dominated by the internal tide, the signal that has the greatest change in velocity with depth is in fact the inertial signal.

While the inertial signal is the dominant signal in the depth-averaged shear spectra, we would like to know what dominates the shear signal at different depths. To see how
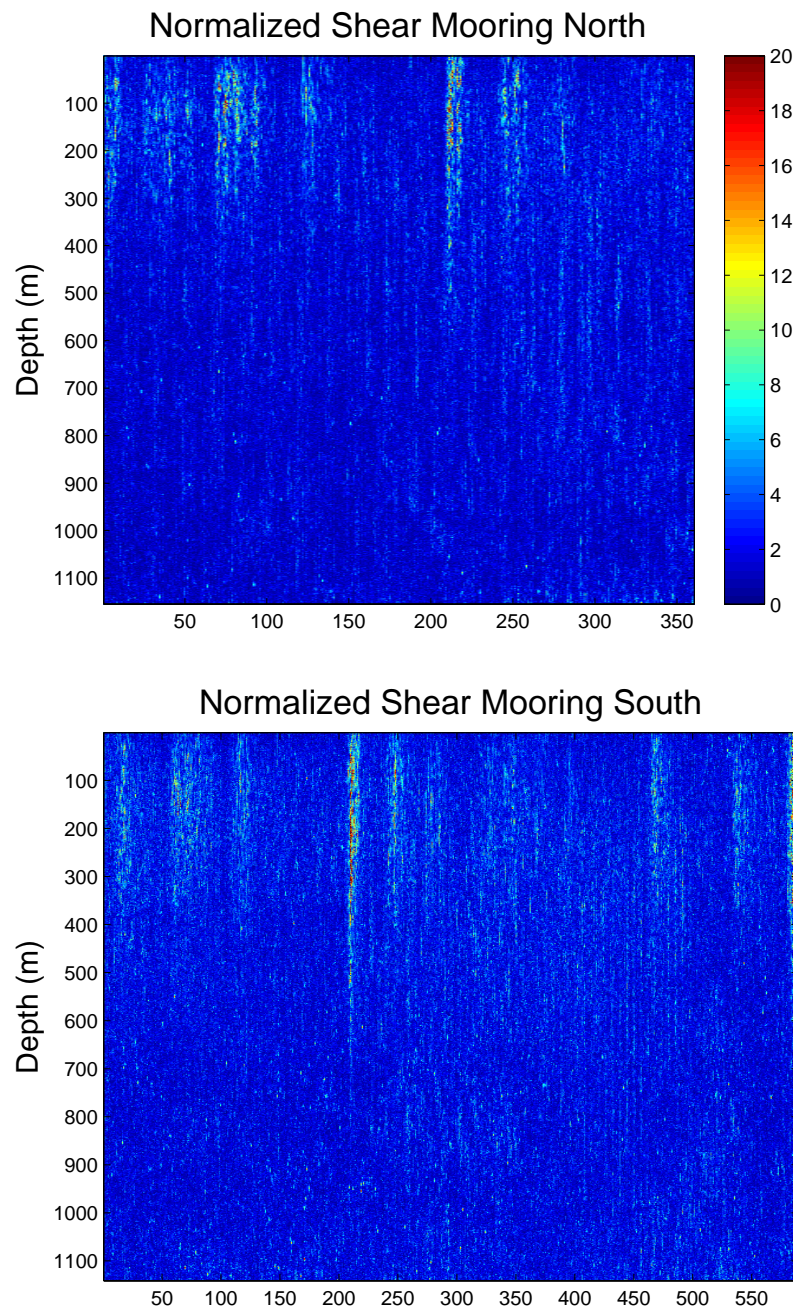
Figure 3.7 – The shear $\frac{d\mathbf{u}}{dz}$, normalized by the Brunt-Vaisala frequency, N, at Mooring North (above) and Mooring South (below).
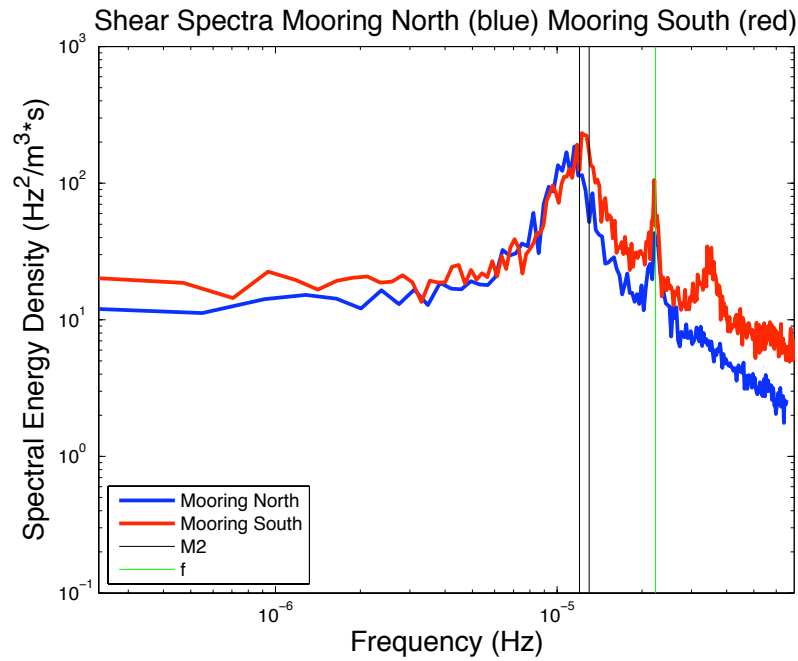
Figure 3.8 – Power spectra of shear. Mooring South (red) shows a much greater mesoscale (low) frequency signal than Mooring North (blue). The dominant peak for both moorings is at the inertial f frequencies for each mooring (black).

the shear spectra varies with depth, we look at the spectra for each of our bins used in the shear-strain parameterization, with lighter colors higher in the water column, and darkening with depth, Figure 3.11. When all of the different spectra from each depth bin are plotted one on top of the other, it is clear that the near-inertial signal dominates at all depths. There is still a contribution from the semidiurnal tide at both moorings, and the difference between the strength of the tidal and near-inertial peaks is even less pronounced at Mooring South, but the near-inertial signal is dominant at all depths.

If, however, we break up the shear spectra at each depth, and look at them individually, as can be seen for Mooring North in Figure 3.10, the near-inertial dominance is less-clear. Near the surface at Mooring North, there is no clear dominant peak in the shear spectra, but rather, just slightly higher energy around the near-inertial and semidiurnal tidal frequencies. As the depth increases, the near-inertial signal increases, indicating that the inertial shear at Mooring North is mostly due to the rough bottom topography.

The near-inertial signal is more clearly seen at all depths of the water column at Mooring South, as can be seen in Figure 3.11. In this case, the near-inertial signal is the dominant signal in the surface waters, and has an even more defined peak lower in the water column. The internal tide also contributes, but is less evident in the surface waters, increasing in strength with depth.

3.5 Summary and Discussion

Since finescale parameterization of WOCE data revealed elevated levels of turbulent mixing above this area of rough topography, the assumption was made that this mixing was due to the internal tide. While the internal tide is in fact the dominant signal in the velocity power spectrum, the dominant signal in the finescale shear spectra is not
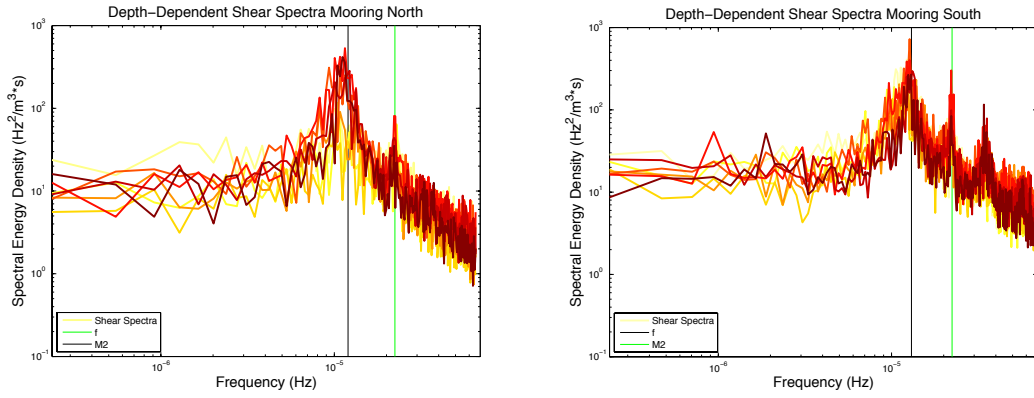
Figure 3.9 – Depth-Dependent Shear at Mooring North (left) and Mooring South (right).
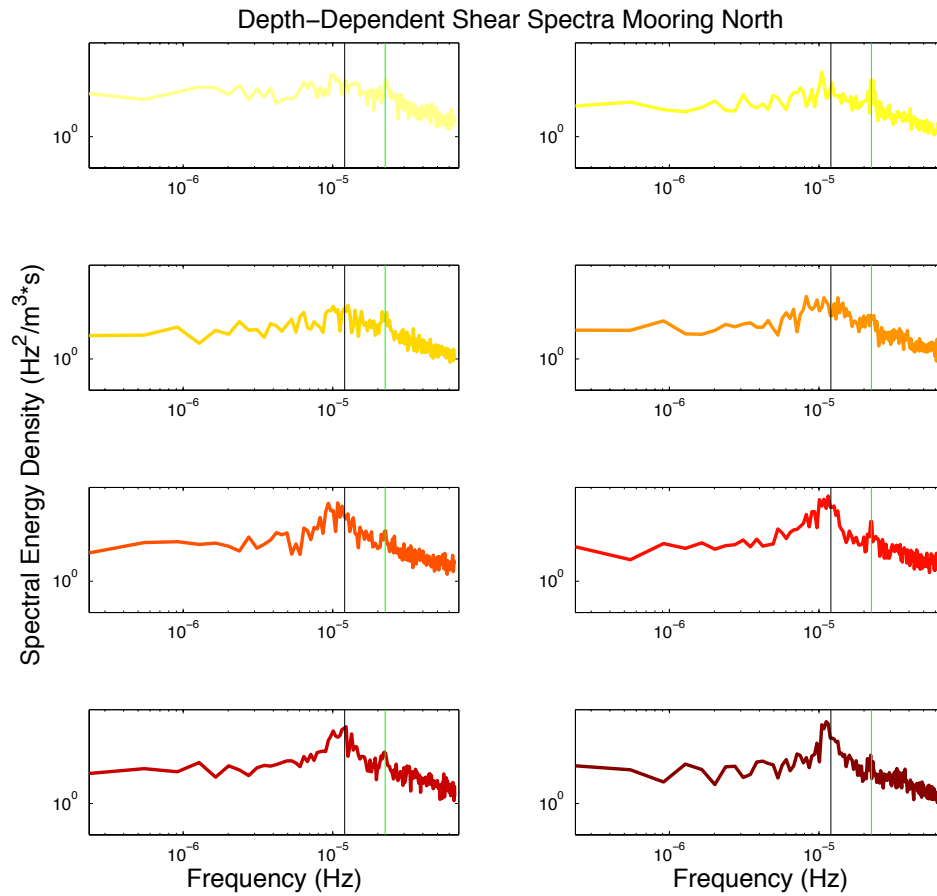
Figure 3.10 – Depth-Dependent Shear at Mooring North.
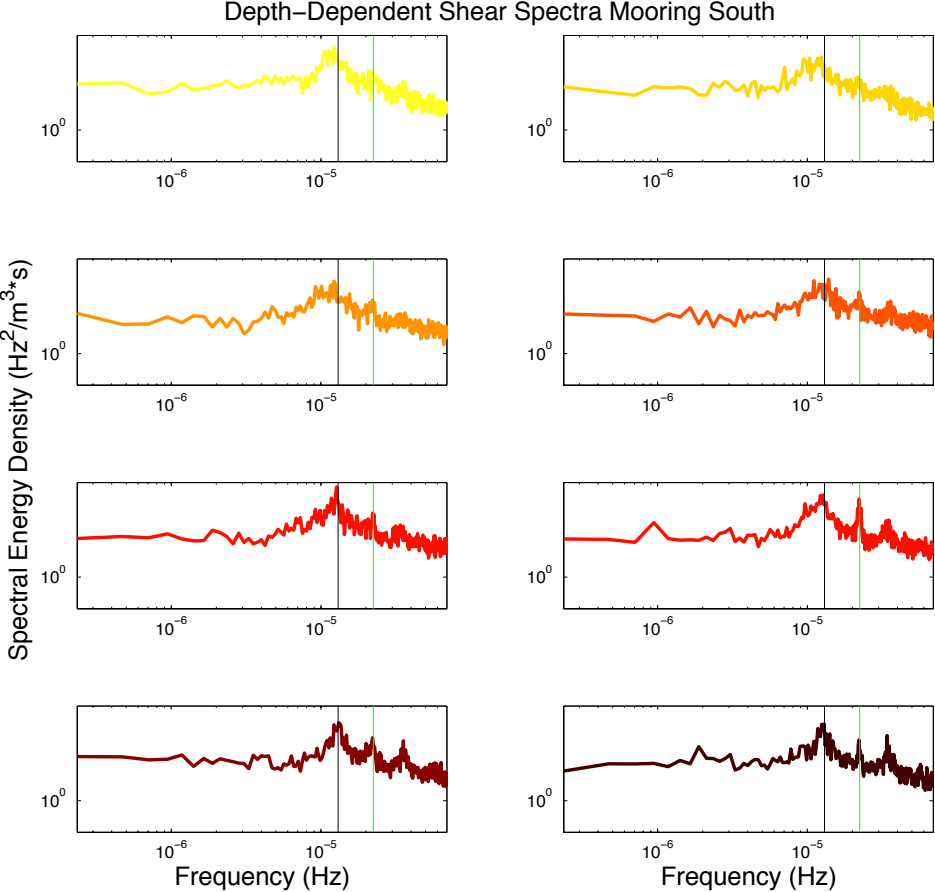
Figure 3.11 – Depth-Dependent Shear at Mooring South.

the internal tide, but rather the inertial signal. The mixing in the region is therefore controlled by the near-inertial signal, and not the internal tide. Even though there is a strong internal tide, and strong parameterized mixing in the region, the internal tide is not in fact responsible for this heightened mixing.

The parameterized mixing in our study region is not homogeneous, but rather varies vertically throughout the water column, as well as spatially between the two moorings, with stronger diffusivities observed at Mooring South, where the mesocale signal is stronger, than at Mooring North. The mixing is consistently strongest near the bottom of the sampled water column for Mooring North, as would be expected due to overturns in the bottom boundary layer near the rough topography, but not so for Mooring South. Mooring South, on the other hand, shows less of a vertical variability, and more of a temporal variability, which could be related to the spring-neap tidal cycle, or changes in the mesoscale eddy field.

Since the mixing is due to the near-inertial signal, and not that of the internal tide, it is strongly dependent on the winds and mesoscale eddy field. A variable mesoscale eddy field, as we have seen in this region of rough topography, will therefore lead to a variable mixing intensity in the region.

Acknowledgments

Chapter 4

The Impacts of Stratification on High Latitude Ocean Mixing: a case study of internal waves in Storfjorden, Svalbard

Abstract

Hydrographic and velocity measurements were taken over four different time periods from April and May 2005-2007 at adjacent stations in Storfjorden, Svalbard. Different environmental conditions, including winds, ice cover, and water mass contributions, yield markedly different stratification (N^2) profiles among the time series. When classified according to the Gerkema (2001) classification system, the stratification profiles span the spectrum with two profiles resembling that of a two-layer fluid, one resembling more closely a fluid of constant stratification, and one falling in between the two extremes. The different N^2 profiles elicit sharply contrasting modal responses from the internal wave field, which is dominated by mode 1 during the two time series most resembling a two-layer fluid, and nearly evenly spread out among the first five modes during the time series with a nearly constant stratification. Turbulent dissipation rates determined from fine-scale parameterizations reveal an average rate on the order of $10^{-9} W kg^{-1}$ for all time series with an associated average diapycnal diffusivity of $10^{-5} m^2 s^{-1}$ - $10^{-4} m^2 s^{-1}$. Turbulent heat fluxes, determined from the estimated turbulent dissipation rates, ϵ, were found to have a relative maximum at the tops of the pycnoclines, with values up to $1 W m^{-2}$, typical of ice-covered conditions. The turbulent dissipation rate and diapycnal diffusivities for each time series vary with the Gerkema (2001) stratification profile rankings, and are elevated for the time series most resembling a fluid of constant stratification, and reduced for the time series most similar to a two-layer fluid.

4.1 Introduction

High latitude internal waves have distinct properties due to their geolocation. Ice cover reduces the wind forcing that generates most of the inertial waves in lower latitudes. This decreased surface forcing, coupled with increased dissipation due to the turbulent boundary layer beneath the rough ice, leads to significantly lower internal wave energy in the Arctic, as compared to lower latitudes (Levine et al., 1985; Levine, 1990). Even with the recent decline in sea ice, internal wave energy in the Arctic has remained low over the past 30 years (Guthrie et al., 2013). Guthrie et al. (2013) attribute this continued low

internal wave energy to enhanced boundary layer dissipation due to increased stratification, and thus increased internal wave horizontal velocity above the pycnocline, relative to the rest of the water column.

Another peculiarity of high latitudes is that the diurnal as well as certain components of the semidiurnal, including M_2, tidal frequencies are sub-inertial, so the baroclinic waves generated by these tidal components are evanescent. While in areas of weak stratification the nontraditional β terms, which come into play in the full projection of the Coriolis force, may expand the range of internal wave frequencies, allowing near-inertial waves to propagate beyond their inertial latitude, (Gerkema & Shrira, 2005a,b) and allowing energy to be focused within these waveguides (Winters et al., 2011), the internal tide remains largely evanescent above the inertial latitude. Previous work suggests that a significant part of the baroclinic tidal energy is dissipated by the instability of these evanescent waves, as energy is transferred to short topography-scale nonlinear internal waves (Vlasenko et al., 2003).

Along with the dissipation due to these unstable evanescent waves, other processes particular to high latitudes, including deep water formation, can impact the energy budget. Deep water formation takes place at high latitudes in openings in the ice known as polynyas, where heat transfers rapidly from the relatively warmer ocean to the colder atmosphere (Schauer, 1995). As the heat is lost to the atmosphere, the sea water freezes, rejecting its saline content in the process, and forming new dense waters which then sink rapidly, destabilizing the water column, and increasing turbulent mixing (Skogseth et al., 2013). Since dissipation at high latitudes is due to multiple processes, the rate of turbulent dissipation varies greatly, ranging from 10^{-10} to $10^{-6} W kg^{-1}$ due to background mixing and breaking internal waves (Fer et al., 2010; Sundfjord et al., 2007), to up to $10^{-5} W kg^{-1}$ during deep water formation (Jardon et al., 2011).

These deep water formation events not only incite instantaneous mixing, but also rapidly alter the shape of the stratification profile. The goal of this study is to look at how these highly variable stratification profiles impact the dynamics and dissipation of the internal wave field at high latitudes. If we can determine what factors control internal wave dynamics and dissipation under these conditions, we can get a better picture of how the ocean mixes at high latitudes.

In order to get some insight into what controls the dynamics and dissipation of high-latitude internal waves, we look at high-latitude data from multiple campaigns in Storfjorden, a fjord in the Svalbard Archipelago. As can be seen in Figure 4.1, Storfjorden, encircled by three islands and a large sill at a depth of $120m$, is semi-enclosed with only two narrow gateways to the northeast (Skogseth et al., 2005; Quadfasel et al., 1988). This Arctic fjord is a highly productive site of deep water formation, responsible for nearly 5-10% of all Arctic Deep Water (Quadfasel et al., 1988). Deep water formation takes place inside the fjord in a recurring polynya that opens during northeasterly winds in winter, allowing heat transfer to the atmosphere, and subsequent ice production and brine release (Skogseth et al., 2013). While the average stratification in Storfjorden is always relatively weak, with typical average N^2 values never exceeding approximately $10^{-4} s^{-1}$, the vertical structure of the stratification profiles can change rapidly, in just a few days, due to these brine release events, or the intrusion of Atlantic water masses (Skogseth et al., 2005). The impact of these strong and rapid modifications of the stratification profiles on the dynamics and dissipation of high-latitude internal waves has never been quantified.

According to Skogseth et al. (2013), the processes occurring in Storfjorden are representative of those in the Arctic shelf seas, which makes this semi-enclosed basin a natural laboratory for studying high-latitude internal wave dynamics and the resultant turbulent mixing. A previous study in Storfjorden, Jardon et al. (2011, 2014) analyzed ice-tethered moorings drifting southward from the northwestern part of the fjord for a 10-day period

in late March 2007. Jardon et al. (2011) found turbulent eddy diffusivities ranging from $10^{-4} - 10^{-6} m^2/s$, which they attributed to breaking internal waves. This paper builds upon Jardon et al. (2011, 2014), by analyzing hydrographic and velocity data from three subsequent years, at a fixed location, to get a deeper understanding of how interannual variations in Storfjorden, specifically changes in the stratification profile, impact internal wave dynamics and dissipation.

An overview of the measurement locations, instrumentation, and data collection methods are laid out in Section 4.2. The hydrographic data, including water masses and stratification, are presented in Section 4.3.1. The currents are presented and discussed in Section 4.3.3. In Section 4.4, the internal waves are characterized, including the energetics of their various frequency components, their associated power spectra, and vertical modes. Finally, the amount of energy dissipating locally is determined by analyzing several different turbulent mixing parameterizations, their associated diapycnal diffusivities, and the resultant heat flux (Section 4.5).

4.2 Data

4.2.1 CTD and ADCP data

The data come from Conductivity/Temperature/Depth (CTD) and Acoustic Doppler Current Profiler (ADCP) measurements obtained during several campaigns in Svalbard aboard the Polar Yacht Vagabond, wintering in Storfjorden. The campaigns include the BRINES campaign, which consisted of three field experiments in April 2005, April 2006, and May 2006, as well as the ICE-DYN campaign of April 2007. The data were collected through the ice at three different nearly co-located stations on the western side of Storfjorden, Svalbard. The stations were located between $18.53^o E - 18.65^o E$, and $77.86^o N - 77.91^o N$, as can be seen in Figure 4.1.

CTD casts were taken by a Seabird SBE 19 plus CTD which was lowered through the ice from a hand-cranked winch on a sledge, at an interval of approximately 30 minutes, during the BRINES campaign from 28-29 April 2005, 8-9 April 2006, and 2-3 May 2006, as well as during the ICE-DYN experiment from 27-28 April 2007. The data were later binned into 1-meter bins.
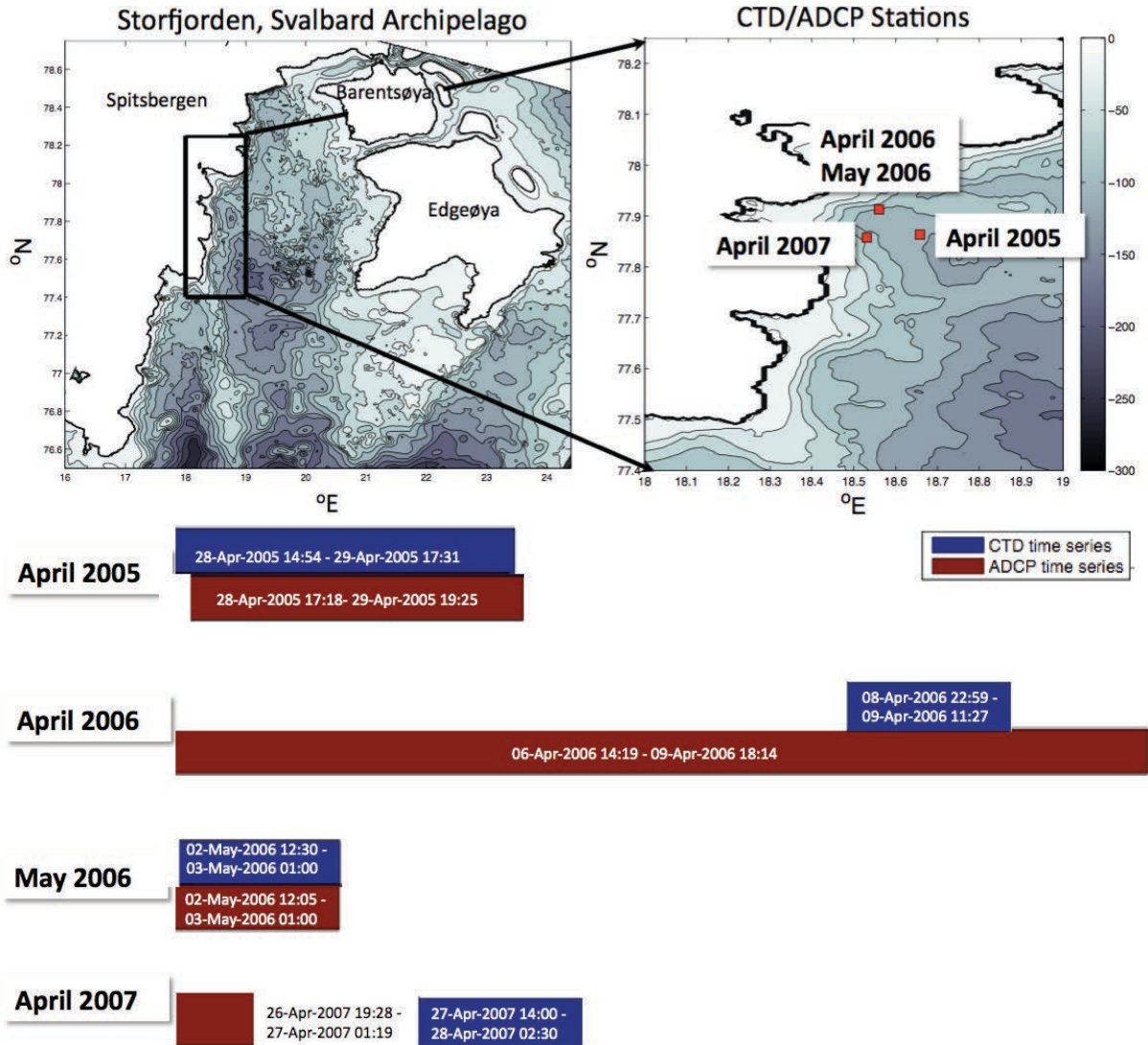
Figure 4.1 – Locations of the three CTD/ADCP stations in Storfjorden (above) (April 2006 and May 2006 were co-located.) The relative length of the CTD (blue) and ADCP(red) time series are depicted (below).

At the latitude of our stations, the inertial frequency is $1.426 \times 10^{-4} s^{-1}$, with a period of 12.24 hours, which falls in between the S_2 and M_2 semidiurnal tidal frequencies. So, at the resolution of our measurements, inertial waves at our stations are almost indistinguishable from the internal semidiurnal tide. In order to measure the contributions from these important frequencies, the CTD casts were performed to encompass at least one inertial/semidiurnal period. The longest of the four CTD time series, April 2005, spans about two semidiurnal tidal cycles, or nearly two inertial wave periods. The three shorter CTD data sets from April and May 2006, and April 2007 each span approximately one semidiurnal/inertial cycle.

ADCP measurements were taken with an ice-tethered downward-looking Teledyne RDI broadband 300 kHz ADCP approximately every five minutes with a 4-meter resolution during all four time series. The longest ADCP time series, April 2006, spans more than six inertial, or semidiurnal, periods. The second-longest, April 2005, spans just over two periods, and May 2006 spans just over one period. Due to a battery failure during April 2007 which caused the ADCP to stop working before the CTD profile could be acquired, the April 2007 ADCP time series is just under half an inertial period. The relative length of the different time series can be seen in Figure 4.1.

4.2.2 Environmental Data

The environmental conditions affecting our data, including winds and ice cover, were obtained by examining ancillary data coincident with our measurements.

Ice Cover

The relative importance of the ice cover during the four different time series is found by examining high-resolution ice charts from the Norwegian Meterological Institute. The ice charts are based on satellite imagery, including 1.5-km resolution Synthetic Aperture Radar data from the satellites Radarsat and Envisat, 10-km resolution Ocean and Sea Ice Satellite Application Facility (O&SI SAF) data derived from Defense Meteorological Satellite Program Special Sensor Microwave Imager (DMSP SSM/I) satellite data, 7-km resolution QuickScat Seawinds derived ice edge, as well as observations from ships and aircraft (PolarView, 2012).

Winds

Since there is no satellite cover of winds at latitudes as far north as our CTD/ADCP stations, we have looked at both the NCEP/NCAR and ECMWF reanalysis wind data. The reanalysis data nearest to our stations is located at 77.14° N, 18.75° E. While these wind data may not give an exact wind stress at the measurement sites, they do reveal the relative strength of the winds during the different time series. The mean NCAR/NCEP reanalysis wind vectors range from 0.69 m/s during April 2005, to 2.6 m/s during May 2006, to 4.3 m/s during April 2007, up to 7.1 m/s during April 2006 (Kalnay, 1996). ECMWF reanalysis wind data are similar in magnitude and direction, ranging from 0.71 m/s in April 2005 to 6.2 m/s in April 2006 (ECMWF, 2014).

4.3 Hydrography and Currents

4.3.1 Water Masses

According to the literature, the main water masses contributing to the waters in Storfjorden include Arctic Water (ArW), which enters the fjord from the east via the East

Spitzbergen Current, and Atlantic Water (AW), carried into the fjord from the south by the Norwegian Atlantic Current, both of which circulate cyclonically through the fjord. In addition to these two water masses formed outside the fjord, local brine rejection leads to the formation of Brine-enriched Shelf Water (BSW) in the fjord. Brine rejection primarily occurs in ArW in the northeastern section of the fjord (Loeng, 1991; Schauer, 1995; Skogseth et al., 2005).

To determine which water masses contribute to the water columns observed during the four time series, we plot the data from each time series on a potential temperature-salinity $(\Theta - S)$ diagram (Figure 4.2). All or part of each observed water column share similar water characteristics with BSW, with $S > 34.8$ and $T < -1.5^oC$, based on the water mass classification from Loeng (1991) and Skogseth et al. (2005).
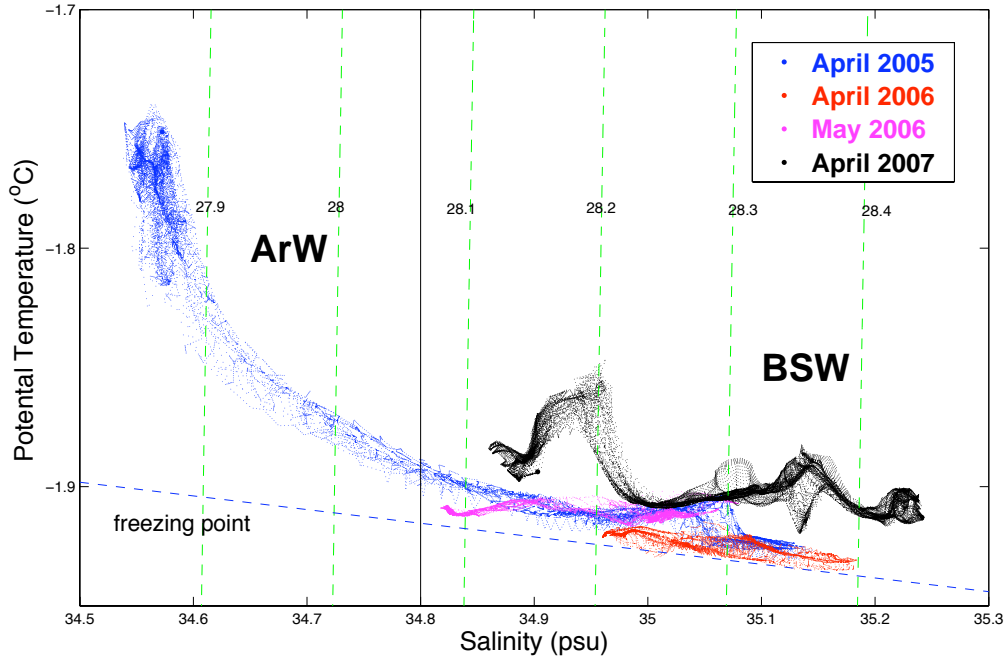
Figure 4.2 – Potential Temperature-Salinity Diagrams from the four time series in Storfjorden. Different colors represent different time series. Dashed green lines trace surfaces of constant density, and the dashed blue line indicates the freezing point temperature. Water masses, based on the water mass classification by Loeng (1991) and Skogseth et al. (2005), are indicated.

While the deeper waters in April 2005 share properties of BSW just like the other three time series, the waters in the top approximately $40m$ share characteristics with the less-dense Arctic Water (ArW), which is not present in any of the other three time series. It is interesting to note that while we did not observe any ArW at our CTD station in April 2007, Jardon et al. (2014) observed ArW further south in Storfjorden just one month prior to our observations.

4.3.2 Stratification

The stratification, as defined by the square of the Brunt-Vaisala, or buoyancy, frequency, $N^2 = -g/\rho_0 \frac{d\rho}{dz}$, was calculated for each time series, and the time-mean vertical

profiles are shown in Figure 4.3. Even though each CTD time series was obtained in similar locations during similar times of year (April and May), each time period is distinguished by a remarkably different N^2 profile, as seen in Figure 4.3. The N^2 profile from April 2005 (Figure 4.3a) shows a marked change in density, a strong pycnocline, at approximately $40m$ depth, the depth at which the water properties shift from those of ArW to those of BSW (Figure 4.2). While the April 2007 N^2 profile also reveals a strong pycnocline in the top of the water column, around $20m$ depth, this strong pycnocline is not unique, but rather is followed by another somewhat less strong pycnocline deeper in the water column (Figure 4.3b). Similarly, the May 2006 N^2 profile (Figure 4.3d) consists of several weaker pycnoclines throughout the water column, and April 2006 (Figure 4.3c) has almost no distinct pycnocline, but rather a nearly constant stratification throughout the water column.

While the April 2006 N^2 profile looks strikingly different from that of April 2005, both of these seemingly incongruous stratification profiles show almost no stratification in the top of the water column to about $20m$ depth, revealing the presence of a mixed layer during these two time periods. From our stratification profiles (Figure 4.3 a and c), we can see that the water begins to get stratified at about $23m$ for April 2005 and about $14m$ for April 2006. These depths correspond to a change in density of $.01kg/m^3$ from the surface, consistent with the criterion used by Fer & Drinkwater (2014) to define the mixed layer depth in the Barents Sea. We take this to be the depth of our mixed layer during these two time series. In contrast, the N^2 from the two other time series, May 2006 and April 2007 (Figure 4.3b and d), do not have clearly defined mixed layers, but rather a changing stratification all the way to the surface. This difference in mixed layer depth (MLD) corresponds to differences in relative ice cover, as can be seen in Figure 4.4. The ice cover in Storfjorden during the time series range from "close drift ice" (70-90% cover) in April 2006, to "very close drift ice" (90-100% cover) in April 2005, and "fast ice" (100% cover) in May 2006 and April 2007. There is less ice cover during the two periods with a mixed layer, April 2005 and April 2006,(Figure 4.4a and c), than during the other two periods where the observed stratification extends to the surface, May 2006 and April 2007 (Figure 4.4b and d).

To objectively compare the N^2 profiles, we have fit each profile to a simple theoretical stratification profile from Gerkema (2001), who used a simple stratification model to analyze the effect of the thermocline on the vertical mode diffraction of an internal tidal beam. While our data are not dominated by an internal tidal beam, but rather span the spectrum of the internal wave field, we are similarly interested in which vertical mode is favored by which stratification profile, and so are also interested in objectively comparing the stratification profiles. The Gerkema (2001) 2c-layer model, based on the stratification classification system first proposed by Baines (1982), consists of a mixed upper layer, a constantly stratified lower layer (from which the "c" is derived), and a jump in density across the interface between the layers (the pycnocline). Based on this simple stratification model, Gerkema (2001) defines the objective parameter $\gamma = \frac{(g'd)^{1/2}}{N_c H}$, where g' is the reduced gravity (g times the relative difference in density across the pycnocline), d is the depth of the pycnocline, N_c is the constant stratification of the lower layer, and H is the total water depth, which is a finite constant. Since the numerator of γ is the phase speed of a wave in a two-layer system, and its denominator, that of a wave in a fluid of constant stratification, γ indicates whether the stratification is more similar to that of a uniformly-stratified fluid ($\gamma = 0$), or that of a two-layer fluid ($\gamma = 1$).

Our N^2 profiles are more complex than those in Gerkema (2001), however, so we cannot simply fit them to the 2c-layer model. Since there is no clearly defined interface, but rather a more gradual change in density between the top and bottom of the water column, following Mercier et al. (2012), we first looked at the density profiles to identify
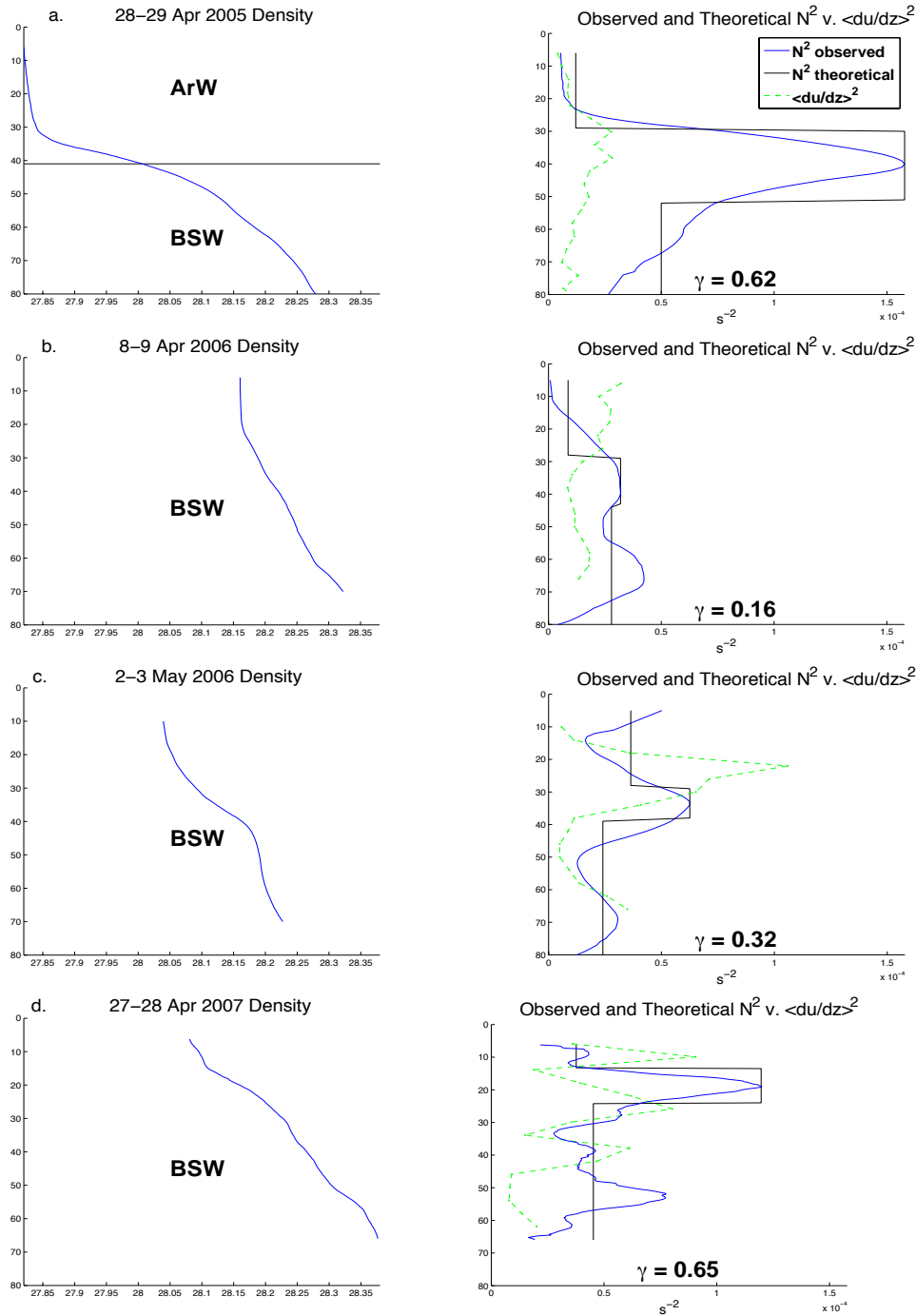
Figure 4.3 – The time-mean density, as well as the sources of the water masses that make up the water columns (Loeng, 1991; Skogseth et al., 2005) are indicated for each profile (left). The time-mean squared shear, $\frac{d\mathbf{u}}{dz}^2$, (green) is compared to the time-mean squared Brunt-Vaisala frequency, N^2, (blue) for each profile (right). The fit to the theoretical Gerkema (2001) 2c-layer model (black), as well as the theoretical $\gamma = \frac{(g'd)^{1/2}}{N_c H}$ are also indicated for each profile (right).
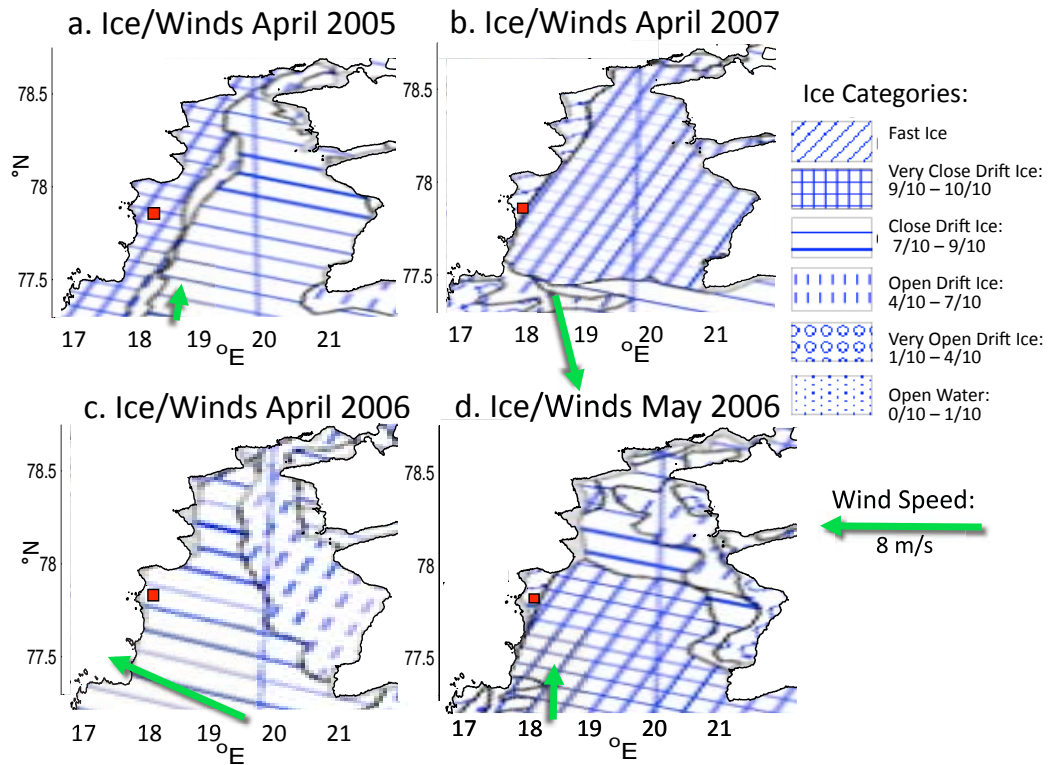
Figure 4.4 – Icecharts in Storfjorden 28 April 2005 (a), 7 April 2006 (c), 2 May 2006 (d), and 27 April 2007 (b). These data come from the Meteorologisk institutt (PolarView, 2012). Both the April 2007 (b) and May 2006 (d) icecharts indicate "fast ice" or solid ice cover, along the western edge of Storfjorden near the CTD/ADCP stations, whereas both April 2005 (a) and April 2006 (c) icecharts indicate no "fast ice" along the western edge, but rather "very close drift ice" (90-100%) and "close drift ice" (70-90%), respectively. The green arrow represents the relative wind strength based on NCAR/NCEP Reanalysis data at 77.14° N, 18.75° E. The wind vectors represent the average wind values over each time series.

the points of inflection which define the top and bottom of each pycnocline. We can then calculate $g' = \int N^2 dz$, where the limits of the integral are the previously defined top and bottom of the pycnocline. To find the depth of the pycnocline, d, we calculate a weighted depth $d = \int z N^2 dz / (\int N^2 dz)$, where the limits of the integral are the same previously-defined top and bottom of the pycnocline. Setting N_c as the average stratification below the pycnocline, and $H = 80m$, the approximate water depth at our stations, we can then calculate $\gamma = \frac{(g'd)^{1/2}}{N_c H}$ for each time series.

We can then compare the dimensionless parameter γ for each of our N^2 profiles. For the two profiles with strong pycnoclines in the top of the water column, April 2005 and April 2007, γ is 0.62 and 0.65 respectively. This value compares favorably with the value for the regime with a very strong thermocline in Gerkema (2001), with a γ of 0.61. The profile with the weakest pycnocline, April 2006, has a γ equal to 0.16, which compares favorably with the moderate thermocline regime in Gerkema (2001), with a γ of 0.12. The profile with multiple moderately strong pycnoclines, May 2006, has a γ of intermediate strength, with a value of 0.32.

Based on the γ's we calculated, we expect the April 2005 and April 2007 internal waves to behave more like those of a two-layer fluid, those of April 2006 to behave more like waves in a fluid of constant stratification, and those of May 2006 to behave somewhere in between these two regimes.

4.3.3 Currents

An overview of the space-time structure of the velocity field at each station is presented in Figures 4.5 - 4.8, starting with the barotropic (depth-mean velocity) signal represented in Figure 4.5. As can be seen in Figure 4.5 a and d, both the zonal and meridional barotropic velocities during April 2005 and April 2006 reveal a semidiurnal/inertial barotropic signal. These two time series also reveal both a lower frequency, or diurnal, signal, as well as a higher-frequency signal with a period of about 6 hours. The average value of the barotropic current indicates a southwesterly flow at nearly all stations. This southwesterly flow is consistent with the cyclonic circulation that has been well-documented in Storfjorden (Loeng, 1991; Schauer, 1995). The magnitude of the average barotropic current is on the order of $5 - 10$ cm/s. For comparison, we ran the Arctic Ocean Tidal Inverse Model (AOTIM-5) (Padman & Erofeeva, 2004), which also yields an average barotropic current of a few cm/s for all stations.

The baroclinic velocity, $\mathbf{U}_{bc}$, the total velocity minus the barotropic velocity, is represented in Figure 4.6. The magnitude of the baroclinic velocities is of the same order as that of the barotropic velocities. All of the baroclinic time series reveal opposite directions in the top and bottom of the water column, indicating a mode-1 response, in the zonal direction (top of Figure 4.6), and this mode-1 response is even more pronounced in the meridional direction (bottom of Figure 4.6). While this pattern is present in all the time series, it is much less apparent in April 2006, the time series with the weakest stratification (see Figure 4.3c), which instead reveals significant vertical propagation of internal waves in both the zonal direction, in particular on 7 April 2006 from 06:00 to 18:00 (Figure 4.6d), as well as in the meridional direction (Figure 4.6h).

Taking the time mean of the baroclinic velocities over a discrete number of inertial periods (which at this latitude is basically a discrete number of semidiurnal tidal periods), reveals significant time-mean baroclinic currents (Figure 4.7). The time-mean currents in April 2005 and April 2007 vary in direction from northeast at the surface and southwest at depth.
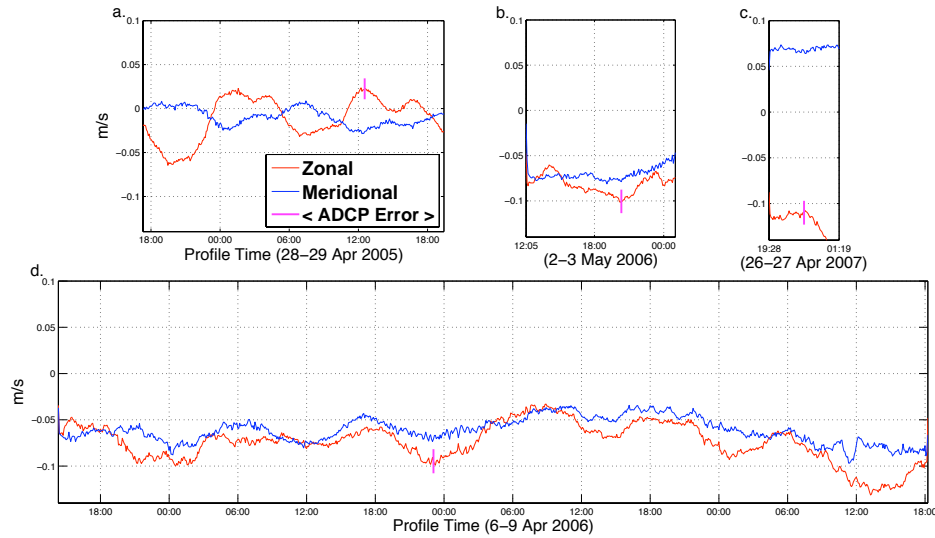
Figure 4.5 – The barotropic (depth-mean) velocities (m/s) in both the zonal (blue) and meridional (red) directions. The average barotropic ADCP error (magenta) is indicated for each station.

4.4 Internal Waves

4.4.1 Baroclinic Perturbation Velocity

To isolate the internal wave field, the time-mean baroclinic currents must be subtracted from the baroclinic velocity ($\mathbf{U}_{bc}$) field, ideally without subtracting any contribution from the underlying internal wave field. Since the main contribution to the internal wave field comes from near-inertial and semidiurnal frequencies and their harmonics, subtracting whole number multiples of the semidiurnal/inertial time period will not diminish these signals. We have defined the baroclinic perturbation velocities, $\mathbf{U}'_{bc}$, as the difference between the $\mathbf{U}_{bc}$ and the time-mean baroclinic current. It is important to note, however, that since the April 2007 time series spans half of one semidiurnal period, when the time-mean current is subtracted from this time series, some of the semidiurnal/inertial energy is unavoidably lost. $\mathbf{U}'_{bc}$ for all stations can be seen in Figure 4.8.

After the time-mean baroclinic currents have been subtracted, the mode-1 response is no longer dominant, but rather the velocities change direction at multiple points in the water column, indicating the presence of other higher modes (Figure 4.8). The absence of the dominant mode-1 signal allows the vertical propagation of the internal waves to be clearly seen in all time series, for example between 28 April 2005 at 18:00 and 29 April 2005 at 06:00 in Figure 4.8e. Despite the similarities in vertical structure, however, significant discrepancies in the magnitude of the velocity fields exist. The two time periods with the greatest γ values, April 2005 and April 2007, have the smallest average perturbation velocities, on the order of $.01m/s$, as compared to $.016m/s$ during the period with an intermediate γ value, May 2006, and $.02m/s$ during the period with the smallest γ value, April 2006. This energetic time series is less dominated by the semidiurnal/inertial period, and appears to have contributions from other higher-frequency signals of approximately 3 and 6 hours.
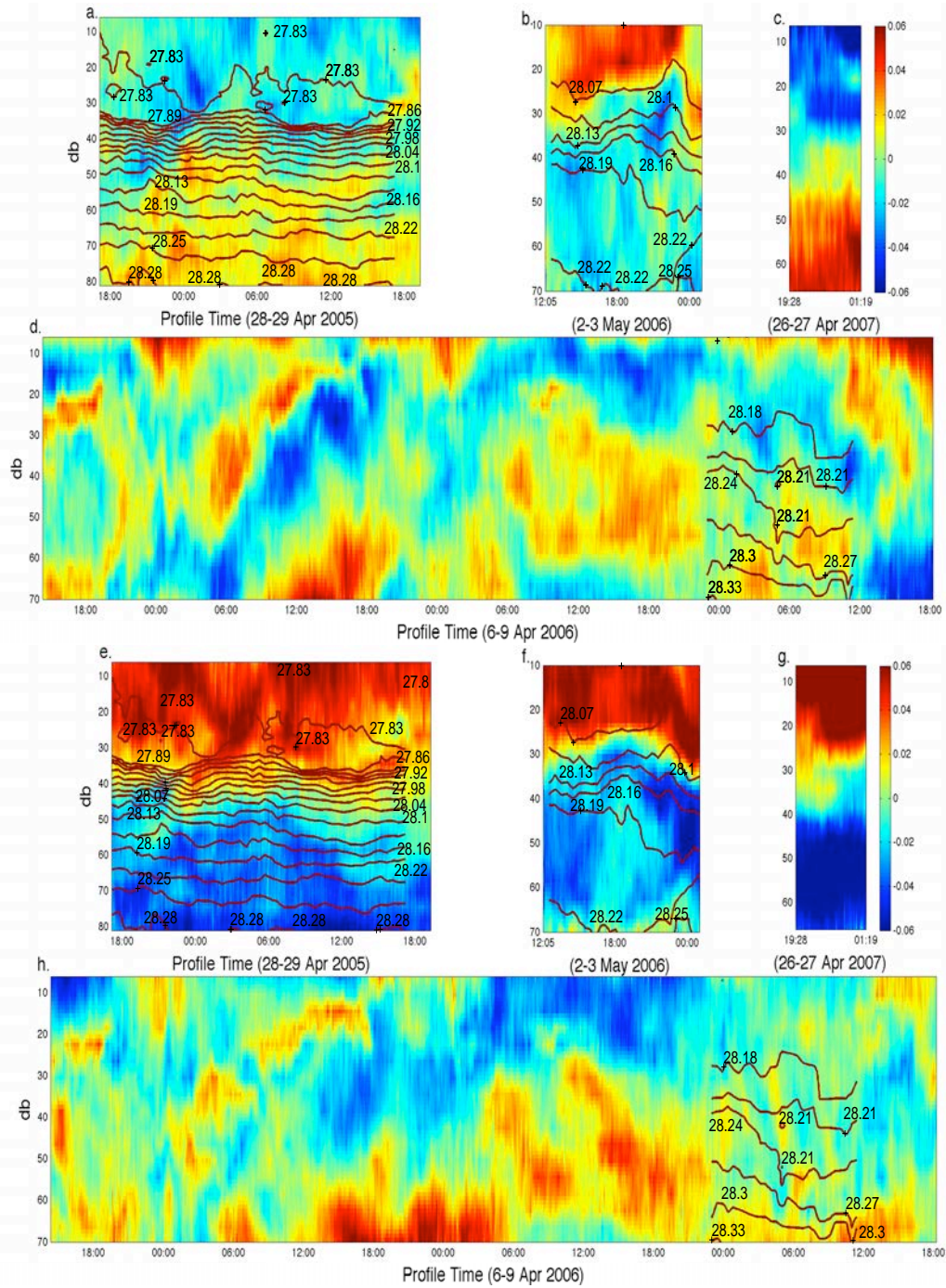
Figure 4.6 – Baroclinic velocities, $\mathbf{U}_{bc}$, in m/s. The top four figures represent zonal component of $\mathbf{U}_{bc}$, and the bottom four display the meridional component. Contours trace isopycnal surfaces.
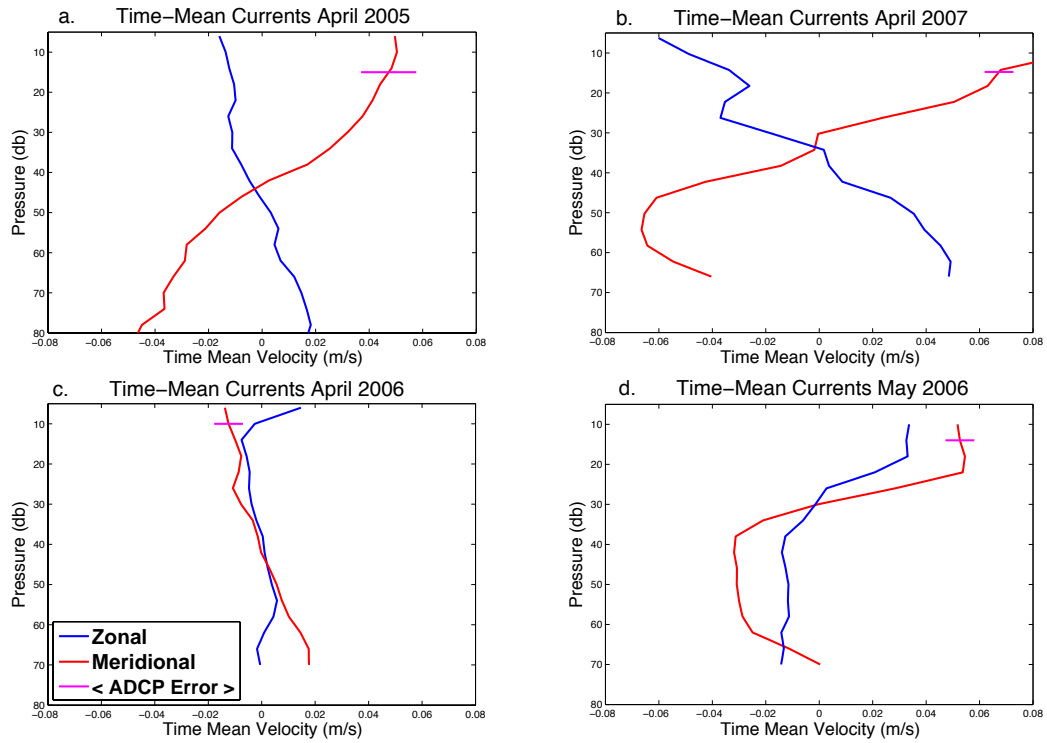
Figure 4.7 – The time-mean of the zonal (blue) and meridional (red) components of the baroclinic velocity over a whole number of inertial periods (2 periods for April 2005, 6 periods for April 2006, and 1 period for May 2006) except for April 2007 where the length of the time series is just under 6 hours (approximately $\frac{1}{2}$ an inertial period). The average time-mean ADCP error (magenta) is indicated for each station.
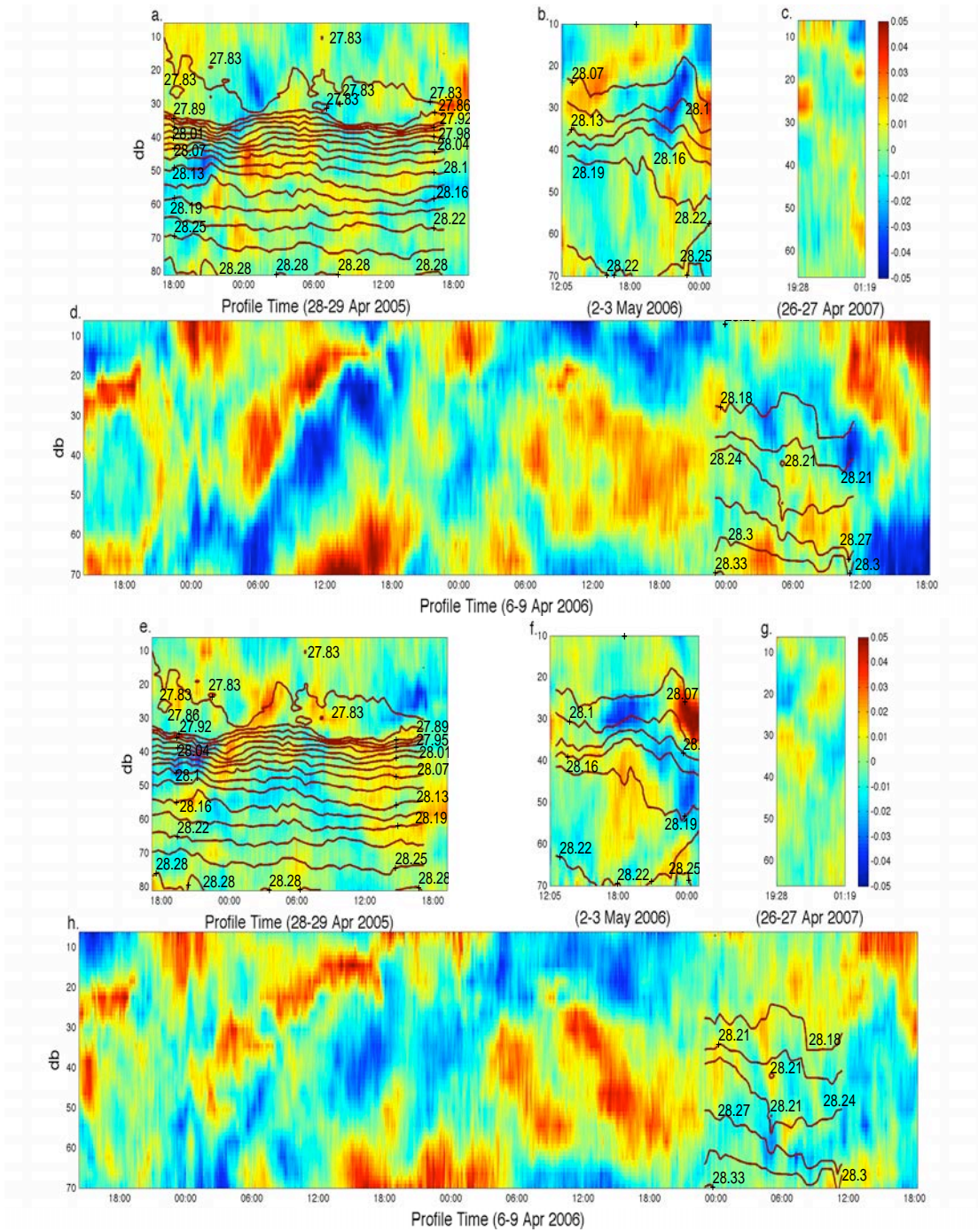
Figure 4.8 – Baroclinic perturbation velocities, $\mathbf{U}'_{bc}$ (baroclinic velocities, $\mathbf{U}_{bc}$, with the time-mean current (Figure 4.7) subtracted) in m/s. The top four figures represent zonal $\mathbf{U}'_{bc}$, and the bottom four are meridional $\mathbf{U}'_{bc}$. Contours trace isopycnal surfaces.

4.4.2   Energetics

In order to characterize the internal wave field and how it contributes to the energy budget, we calculate its mechanical energy, both that due to its isopycnal displacement (potential energy) and that due to its velocity (kinetic energy). Since the perturbation velocity time series (Figure 4.8) reveal semidiurnal/inertial signals, as well as 3- and 6-hour signals, the contribution from each of these specific signals is analyzed. Along with these higher-frequency signals, a low-frequency signal was also apparent in both the barotropic and baroclinic signals of April 2005 and April 2006, so for these two periods, the diurnal signal is also analyzed. The modal response of each of these components is then determined, along with the contribution of each of the vertical modes to the overall internal wave energetics.

Mechanical Energy

The available potential energy (APE) of the internal wave field is $\frac{1}{2}\eta^2 N^2$, where η, the isopycnal displacement, is $\rho'/\frac{d\rho}{dz}$, and ρ' is the perturbation from the time-mean density at each depth. The kinetic energy (KE) of the internal wave field is $KE = 1/2(\mathbf{u}^2 + \mathbf{v}^2)$. The KE was calculated for the baroclinic velocities (KE_{bc}), as well as the baroclinic perturbation velocities (KE'_{bc}).

In order to calculate the component of the kinetic and potential energies due to the diurnal and semidiurnal internal tides, and that due to the 3- and 6- hour signals, the velocities and the isopycnal displacement must be isolated at those specific frequencies. Since the time series are not long enough to distinguish specific components, we have separated the various components using a harmonic analysis, following the method laid out in Gerkema & van Haren (2007), who separated the various components by assuming that different components are orthogonal, mimicking a Fourier transform. Since this method does not allow us to distinguish between nearby frequencies, we have lumped nearby frequencies together around each of the signals of interest before performing the frequency transformation. For example, M_2, S_2, and the inertial frequency were all grouped together as one frequency, and will henceforth be referred to as the semidiurnal (sd) frequency.

For all time series, the semidiurnal/inertial component of both the potential and kinetic energies are the biggest contributors to the energy of the internal wave field, followed by the 6-hour component, and then the 3-hour component. For the time series longer than 24 hours, however, the diurnal signal for both the potential energy PE_{24h} (in April 2005), and the kinetic energy KE_{24h} (in April 2005 and April 2006) is a strong contributor, overlapping with the semidiurnal signal at several depths. The time mean of the various components of the KE are plotted in Figure 4.9.

Figure 4.9 reveals a node, an energy minimum, in the baroclinic velocities (KE_{bc}) in the middle of the water column in April 2005 and April 2007, indicative of a mode-1 response during these two time series. May 2006 similarly shows a local node in the top of the water column, as well as a second local node in the bottom, but this nodal pattern is entirely absent from the KE_{bc} in April 2006. Once the time-mean currents have been subtracted, and just the KE'_{bc} remains, this strong nodal feature disappears, and is not distinguishable in the semidiurnal, KE_{sd}, the 6-hour, KE_{6h}, nor the 3-hour KE_{3h} signals.

Power Spectra

The APE and KE power spectra were calculated by Fourier-transforming the time series at each depth, and averaging over all depths. The biggest peak in both the APE and KE power spectra occurs at the semidiurnal frequency, revealing the presence of near-inertial waves and/or a semidiurnal internal tide. Both the APE and KE power spectra
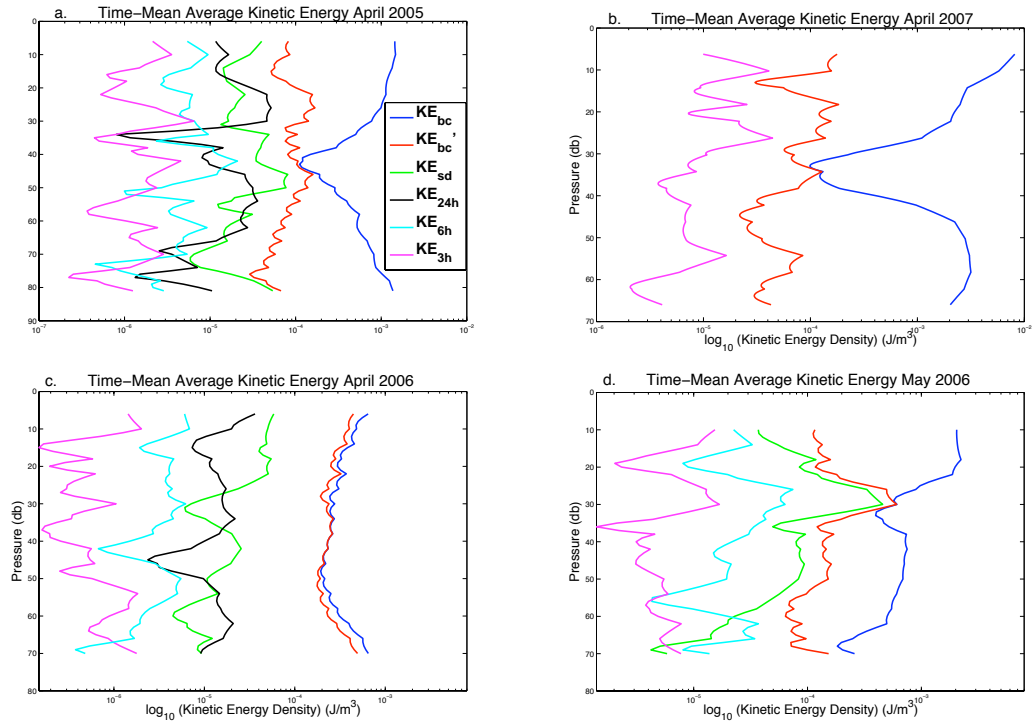
Figure 4.9 – Time-mean kinetic energy of several components of the velocity field, including the baroclinic velocity ($\mathbf{U}_{bc}$), the baroclinic perturbation velocity ($\mathbf{U}'_{bc}$), as well as the semi-diurnal ($\mathbf{U}_{sd}$), the diurnal ($\mathbf{U}_{24h}$), the 6-hour ($\mathbf{U}_{6h}$), and the 3-hour ($\mathbf{U}_{3h}$) components.
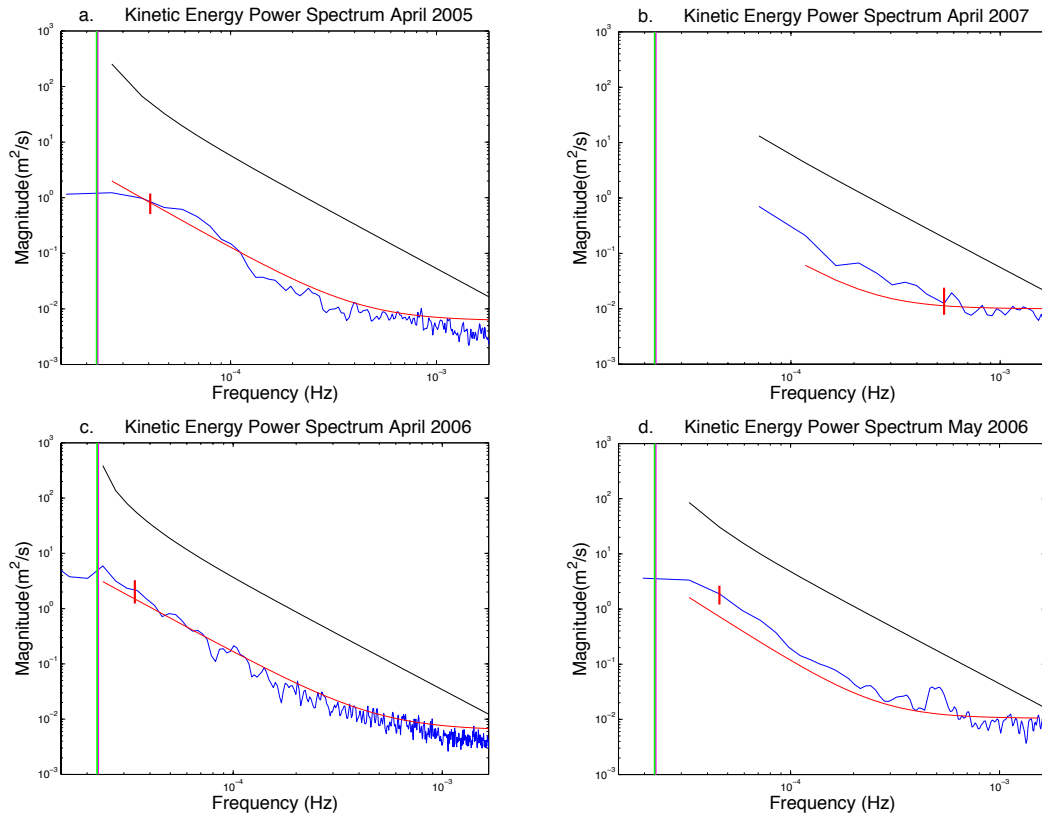
Figure 4.10 – The observed kinetic energy power spectra, the sum of the square of the meridional power spectra and the square of the zonal power spectrum, (blue), and the power law fit to the spectra (red), together with the Garrett-Munk spectra (black) (Garrett & Munk, 1972, 1975). The nearly-collocated semidiurnal frequency (green) and inertial frequency (magenta) are the most energetic components of the power spectra. The red lines represent 95% confidence intervals.

reveal similar results. To save space, just the KE power spectra have been plotted, as can be seen in Figure 4.10

The power spectra have been compared to the Garrett-Munk (GM) spectra (Garrett & Munk, 1972, 1975), which, as can be seen in Figure 4.10, are more energetic than the observed spectra. The total variance for the GM potential energy spectrum, which according to Parseval's Theorem is equivalent to the area under the power spectral curve, is on the order of 10^{-5} m^2/s^2, compared to the total variance in the observed potential energy spectra which are all on the order of 10^{-7} m^2/s^2. The total GM kinetic energy variance is on the order of 10^{-3} m^2/s^2, while the total variance in the observed kinetic energy spectra are all on the order of 10^{-5} m^2/s^2, which indicates a reduction in energy by a factor of about .01. These results are consistent with those of other Arctic experiments, which exhibit lower internal wave energy when compared with that of lower latitudes (i.e. Levine et al., 1985; Levine, 1990; Jardon et al., 2011; Fer et al., 2003, 2004, 2010). Levine et al. (1985) and Levine (1990), who find the Arctic wave field less energetic by an order of .02, attribute this reduced internal wave energy in the Arctic to the ice cover which reduces the wind forcing, increases momentum loss due to internal ice stress, and dampens the internal wave field due to the turbulent boundary layer beneath the ice. Along with the ice cover, Levine et al. (1985) and Levine (1990) also cite the weak circulation of the

Arctic Ocean, as well as the fact that at higher latitudes, the internal tide is evanescent and not able to propagate as free waves, as possible explanations for this reduced internal wave energy.

While the observed power spectra are not as energetic as the GM spectra, by a factor of about .01, the shape and slope of the power spectra are similar to those of Garrett and Munk. To find the slope of the observed spectra, we fit the spectra to a simple power law fit plus constant noise, $A * f^{exp} + noise$, and found the slopes to range from -2.05 for April 2006, to -2.09 for April 2005, to -2.37 for April 2007, and -2.41 for May 2006, which are all comparable to the -2 slope of the GM spectrum.

4.4.3   Vertical Modes

To determine the vertical structure of the internal wave field, we project the measured velocity on the vertical modes. The modal components of the velocity were then used to calculate the KE for each mode. In Figure 4.11, we compare the percentage of KE per mode for the first ten modes for the total baroclinic kinetic energy (KE_{bc}), the semi-diurnal kinetic energy (KE_{sd}), and the baroclinic perturbation kinetic energy (KE'_{bc}) for each time series.
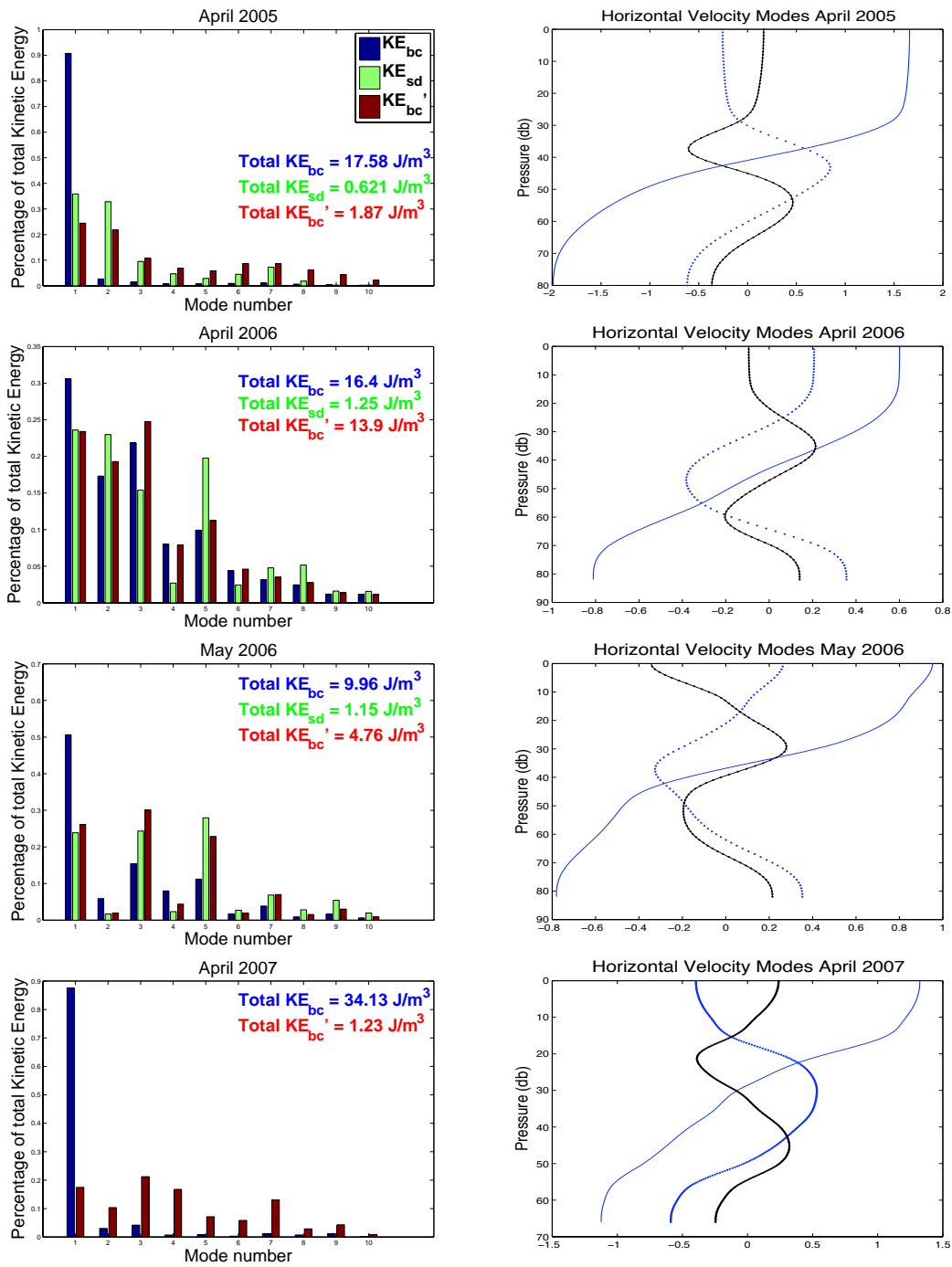
Figure 4.11 – Percentage of kinetic energy in the first 10 modes of the total baroclinic velocity, KE_{bc}, baroclinic perturbation velocity, KE'_{bc}, and the semidiurnal velocity, KE_{sd}, (left), and the first 3 horizontal displacement modes (right).

As can be seen in Figure 4.11, mode 1 is the dominant mode of the total baroclinic kinetic energy (KE_{bc}) for all four time series. During April 2005 and April 2007, however, approximately 90% of the KE_{bc} is in mode 1, which is similar to the response we would expect in a two-layer fluid, where all the energy is in mode 1. This mode-1 response can be attributed to the very strong pycnoclines evident in the April 2005 and April 2007 N^2 profiles (Figure 4.3a and b), and their associated high γ values of 0.62 and 0.65 respectively, which indicate a stratification profile similar to that of a two-layer fluid (see Section 4.3.2). While mode 1 is also the dominant mode for KE_{bc} during April 2006 and May 2006, it accounts for only 50% of KE_{bc} for May 2006 and only 30% for April 2006, which corresponds to their low γ values of 0.32 and 0.16 respectively.

If, however, we break $\mathbf{U}_{bc}$ down, and look at the modal decomposition of the KE of the time-mean currents and that of the baroclinic perturbation velocities (KE'_{bc}) separately, we find that the mode-1 dominance seen in $\mathbf{U}_{bc}$ is due mostly to its time-mean current. The mode-1 dominance of the time-mean KE is particularly strong for April 2005, for which 99% of the time-mean KE is in mode 1, whereas only 88% of the time-mean KE for April 2007 is in mode 1, and less than 70% for May 2006 and April 2006. The KE of just the semidiurnal component of the internal waves, KE_{sd}, shows a similar distribution of energy by mode. For April 2005, while most of KE'_{bc} and KE_{sd} energy is still in mode 1, the energy is spread out over several modes, demonstrating that the energy is not purely mode 1 as it would be in a two-layer fluid, but rather lies on the spectrum between a pure two-layer fluid and a fluid of constant stratification, falling very close to the side of the two-layer fluid, which is consistent with its high γ value of 0.62.

If we look at KE'_{bc} and KE_{sd} for April 2006, we see that the energy is almost evenly distributed among the first five modes. So, on the spectrum between a fluid of constant stratification and that of a two-layer fluid, the stratification profile in April 2006 falls closer to a fluid of constant stratification, which favors an even distribution of energy over all modes. This is consistent with April 2006's low γ value of 0.16. KE'_{bc} and KE_{sd} for May 2006 similarly show peaks in other modes, but in this case, there is strong dominance in three particular modes, modes 1, 3, and 5, indicating that, while the modal response in May 2006 is far from purely mode-1, it is closer than that of April 2006, and thus lies more in the center of the spectrum between a fluid of constant stratification and that of a two-layer fluid, as predicted by its moderate γ value of 0.32.

4.5 Mixing

Turbulent mixing of the water column changes the distribution of physical water properties such as heat and salt. To get an insight into how much turbulent mixing we expect during each of our time series, we calculate the Richardson number, $Ri = N^2/S^2$, where S^2 is the shear squared ($S^2 = [(du/dz)^2 + (dv/dz)^2]$). Ri gives a measure of the likelihood that a stratified water column will undergo shear instability by balancing the stabilizing effects of the stratification, N^2, against the destabilizing effects of the shear, S^2. Smaller Ri reflects, therefore, a less stable water column, with the canonical cut-off for expected shear instability occurring at $Ri < 0.25$.

The Ri values for our time series, as can be seen in Figure 4.12, reveal areas of anticipated instabilities at different points in the water column for each time series. Low Ri values in May 2006 and April 2007 occur at specific depths, occurring on or just above the pycnoclines during these time series (see also Figure 4.3). During both April 2005 and April 2006, the two periods with a surface mixed layer, low Ri values are concentrated in the mixed layer, as expected. Below the mixed layer, low Ri values occur throughout the water column with no specific depth-dependence. The incidence of low Ri values is substantially greater in April 2006 than in April 2005. The greater occurrence of low Ri
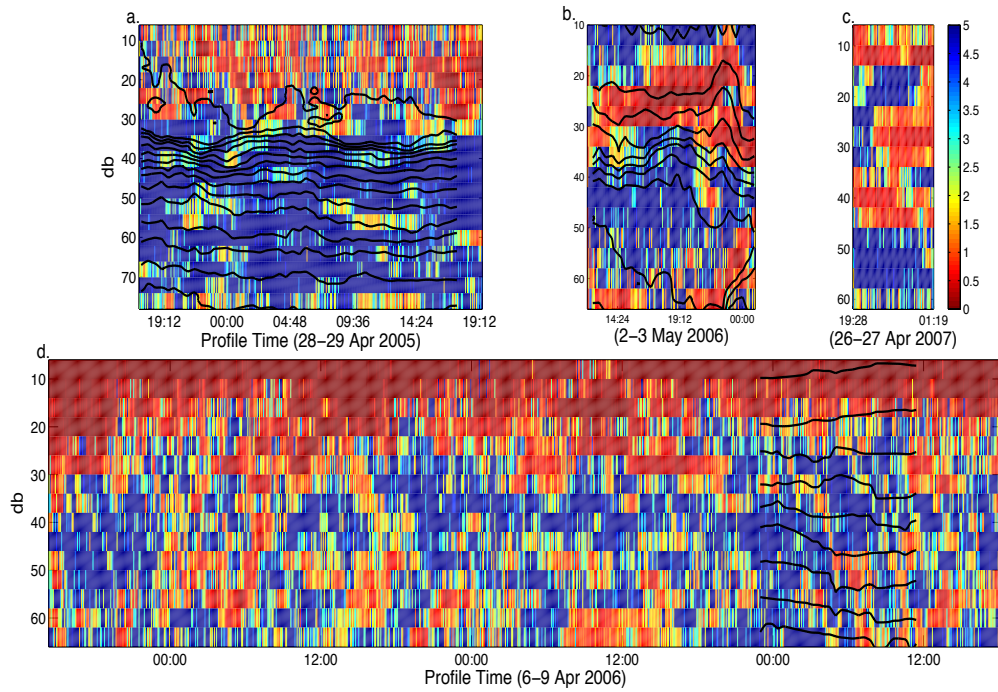
Figure 4.12 – Richardson number ($Ri = N^2/S^2$), based on the average N^2 and the total shear squared ($S^2 = [(d\mathbf{u}/dz)^2 + (d\mathbf{v}/dz)^2]$) for each time series. Contours trace isopycnal surfaces.

values in April 2006 is consistent with its low γ value, which indicates more energy in higher modes and thus a greater tendency for shear instabilities.

Once we have an idea of where we expect the water column to undergo shear instabilities, we determine how much turbulent kinetic energy is dissipating locally at each station. Since we do not have any simultaneous microstructure measurements, we cannot directly quantify the turbulent dissipation rate during the time series. We can, however, look at some larger-scale parameters, including stratification and shear, to get an approximation of the magnitude of the mixing generated by the internal wave field, based on dimensional scaling and fine-scale parameterizations.

4.5.1 Dimensional Scaling and Fine-Scale Parameterizations

Dimensional Scaling

Thorpe scale dimensional analysis (Thorpe, 2005) approximates the overall turbulent mixing based on the RMS length of observed density overturns, the Thorpe length, L_{Th}, and a linear relationship between L_{Th} and outer scale of the turbulence, the Ozmidov length, L_O:

$$L_{Th} = c_1 L_O,$$

where c_1 is a constant that ranges from $.63 - .91$ (Thorpe, 2005). L_O is the length scale of vertical displacements that occur as turbulent kinetic energy is converted into potential energy, which scales like $L_O = (\epsilon N^{-3})^{\frac{1}{2}}$. L_{Th} is determined by comparing the actual density profiles with profiles sorted so the density is ascending with depth. Based on Thorpe-scale analysis, the rate of turbulent dissipation, hereinafter ϵ_{Th}, can be determined by:

$$\epsilon_{Th} = c_1 L_{Th}^2 (N_{ot}^3)[Wkg^{-1}]$$

where N_{ot} is the average sorted stratification within the overturn. To keep our estimate of turbulent dissipation consistent with other estimates in Storfjorden, we have used $c_1 = 0.64$, following Jardon et al. (2011). To isolate overturns due to turbulence from those due to noise in the signal, we determined the noise level by comparing our spectra to an idealized spectrum composed of the GM spectrum plus a noise spectrum, which yields a density noise level on the order of 10^{-4} kg/m^3, and followed the method laid out in Ferron et al. (1998) to eliminate any spurious overturns due to noise.

Fine-Scale Parameterizations

While Thorpe-scale analysis determines the rate of turbulent dissipation by dimensional scaling of larger-scale turbulent overturns, fine-scale parameterizations, such as the the Gregg-Henyey (GH) parameterization (Gregg, 1989) and the MacKinnon-Gregg (MG) parameterization (MacKinnon & Gregg, 2003, 2005), determine the rate of turbulent dissipation based on the eikonal wave-wave interaction model and the assumption that the spectral shape of the internal wave field is in a steady state. GH, the most germaine of these fine-scale parameterizations, is based on comparison between empirical open-ocean data, and the Garrett-Munk (GM) model. The rate of turbulent dissipation determined by GH, hereinafter ϵ_{GH}, scales the fourth power of the observed 10-m shear with that of GM. Since our internal wave power spectra have similar shape and slope to the GM power spectrum, we have used this parameterization to estimate the rate of turbulent dissipation, ϵ_{GH}:

$$\epsilon_{GH} = 1.8 \times 10^{-6}[fcosh^{-1}(N_0/f)](S_{10}^4/S_{GM}^4)(N^2/N_0^2)[Wkg^{-1}],$$

where S_{GM} is the modeled 10-m Garrett-Munk shear, and $S_{GM}^4 = 1.66 \times 10^{-10}(N^2/N_0^2)^2[s^{-2}]$, S_{10} is the shear at 10-m resolution, f is the Coriolis frequency, which at our latitude is approximately $1.426 \times 10^{-4}[s^{-1}]$, and $N_0 = 3$ [cph].

While GH was intended to parameterize waves in the open ocean, MG modifies GH for low-mode dominated coastal regions, as is the case with our Storfjorden stations. As opposed to the GH scaling, which relies on 10-m resolution shear scaled by the GM shear variance, the turbulent rate of dissipation determined by MG, hereinafter ϵ_{MG}, relies on 1-m resolution low-frequency mode-1 shear. For consistency, we have used the same 4-m shear to calculate both ϵ_{MG} and ϵ_{GH}, as opposed to (S_{10}), following MacKinnon & Gregg (2003). To quantify the shear in the most precise manner possible, we have computed the vertical derivative in spectral space by periodizing the 4-m resolution ADCP velocity and taking the inverse Fourier transform. For consistency, the 4-m observed shear, S_4, is scaled by the 4-m GM shear S_{4GM} (Klymak, 2012). Using the 4-m shear of the entire velocity field, we have employed a modified version of MG:

$$\epsilon_{MG} = \epsilon_0(N/N_0)(S_4/S_0)[Wkg^{-1}],$$

where $S_0 = N_0 = 3$ [cph], and ϵ_0 is an adjustable parameter found by fitting ϵ_{MG} to simultaneous microstructure measurements. Since we do not have simultaneous microstructure measurements, however, we cannot use them to adjust our ϵ_0. Working under the assumption that "when overturns are observed, the dissipation rates calculated from (ϵ_{Th}) are roughly the same magnitude as the rates calculated from microstructure," (MacKinnon & Gregg, 2005), we take the time series that has overturns consistently throughout the water column, April 2007, and fit our ϵ_{MG} to our ϵ_{Th} using a least squares fit to find the value of ϵ_0. While there is no defined mixed layer in April 2007, if we fit only the ϵ_{Th} values below the pycnocline depth (defined in Section 4.3.2), we can limit the overturns

due to surface processes. We find $\epsilon_0 = 4.6 \times 10^{-9} W kg^{-1}$, which is the same order of magnitude as MacKinnon & Gregg (2005), whose $\epsilon_0 = 1.1 \times 10^{-9} W kg^{-1}$.

To compare the contributions to mixing due to the baroclinic field perturbations, and those due to the total baroclinic field, we have calculated ϵ_{MG} and ϵ_{GH} using both the $\mathbf{U}'_{bc}$ shear, and the $\mathbf{U}_{bc}$ shear. Since these parameterizations are based on wave-wave interactions in the stratified water column, they have only been applied below the mixed layer for the two time series with mixed layers (April 2005 and April 2006).

Once we have found the rate of turbulent dissipation, ϵ, we use that to find the rate of diapycnal diffusivity, κ_z. Assuming that turbulence is stationary, we can define the relationship between ϵ and κ_z as

$$\kappa_z = \Gamma \epsilon / N^2, \tag{4.1}$$

where Γ is known as the mixing efficiency. Osborn (1980) found that the upper bound for Γ is 0.2 and this value is commonly used to determine κ_z from ϵ. Several recent studies, however, have also shown that the mixing efficiency is not a constant, but rather decreases with the turbulence intensity, I, which is defined as:

$$I = \frac{\epsilon}{\nu N^2},$$

where ν is the kinematic viscosity of water. I can be seen as the ratio of the stabilizing effects of viscosity and stratification against the destabilizing effects of turbulence. Using high-resolution numerical simulations of stratified turbulence, Shih et al. (2005) have proposed empirical laws to parameterize κ_z as a function of I. They define three regimes: In the diffusive range where the turbulent intensity is low, the total diffusivity reverts to the molecular value, $\kappa_T = 1 \times 10^{-7} m^2/s$. If the turbulent intensity is in an intermediate range between 7 and 100, κ_{turb} is defined by the Osborn (1980) relation, $\kappa_{turb} = \frac{\Gamma \epsilon}{N^2}$, with $\Gamma = 0.2$. If, however, the turbulent intensity is elevated above 100, $\kappa_{turb} = 2\nu I^{\frac{1}{2}}$. The turbulent intensities in our data range from $I \approx 1$ to $I \approx 600$, with the majority lying in the intermediate range. The total κ_z is then found by adding $\kappa_{turb} + \kappa_T$.

4.5.2 Mixing Estimates

In order to compare the relative mixing between our four stations with their four distinct stratification profiles, we have calculated both the MG and GH fine-scale parameterizations, and indicated the average values, along with the 95% confidence intervals, in Table 4.1.

MG yields an overall average ϵ_{MG} estimate of $5 \times 10^{-9} W kg^{-1}$ for the $\mathbf{U}_{bc}$ field. The average ϵ_{MG} for each time series varies slightly, ranging from 3 to $7 \times 10^{-9} W kg^{-1}$ for the $\mathbf{U}_{bc}$ field, with the average values dropping slightly to 2 to $5 \times 10^{-9} W kg^{-1}$ for the $\mathbf{U}'_{bc}$ field (Table 4.1). Similarly, GH yields ϵ_{GH} estimates of the same order as ϵ_{MG}, with an overall average value of $6 \times 10^{-9} W kg^{-1}$. The average ϵ_{GH} for each station, however, reveal greater differences between the stations, with values ranging from $1.1 \times 10^{-9} W kg^{-1}$ in April 2005 to $1.1 \times 10^{-8} W kg^{-1}$, an order of magnitude greater, in May 2006, for the $\mathbf{U}_{bc}$ field. If we look at the the average ϵ_{GH} values based on just the $\mathbf{U}'_{bc}$ field, the ranking is consistent with the γ value for each time series (see Section 4.3.2), with the two time series with the greatest γ values, April 2005 and April 2007, having the lowest ϵ_{GH} values of $1.0 \times 10^{-9} W kg^{-1}$, followed by May 2006, and then April 2006, the station with the lowest γ value, having the highest ϵ_{GH} value of $6.3 \times 10^{-9} W kg^{-1}$, as can be seen in Table 4.1.

Figure 4.13 compares the time-mean ϵ_{MG} and ϵ_{GH} calculated from $\mathbf{U}_{bc}$, hereinafter ϵ_{bc}, and $\mathbf{U}'_{bc}$, hereinafter ϵ'_{bc}. The two time series with the biggest drop between ϵ_{bc} and ϵ'_{bc} are April 2007, whose mean ϵ_{GH} drops from $6.1 \times 10^{-9} W kg^{-1}$ for ϵ_{bc} to $1.0 \times 10^{-9} W kg^{-1}$

Table 4.1 – Values of chosen parameters from each time series. Average wind speed and ice cover are shown in rows 2 and 3, respectively. The Gerkema (2001) γ parameter is shown in the fourth row, and the percentage of baroclinic KE in mode 1, in the fifth row. Rows 6-13 represent arithmetic mean values of ϵ and κ_z for both U_{bc} and U'_{bc} based on MG and GH parameterizations, with the 95% confidence intervals indicated in brackets.

time series	April 2005	April 2006	May 2006	April 2007
winds $[m/s]$	.69	7.1	2.6	4.3
% ice cover	90-100%	70-90%	100%	100%
γ	.62	.16	.32	.65
$\%KE_{bc}$ in Mode 1	91%	31%	51%	88%
ϵ_{GH} $[Wkg^{-1}]$	1.2e-9 [1.0 1.3]	6.9e-9 [6.3 7.6]	1.1e-8 [.74 1.5]	6.1e-9 [5.3 6.8]
ϵ'_{GH} $[Wkg^{-1}]$	1.0e-9 [.81 1.2]	6.3e-9[5.7 7.0]	5.6e-9 [2.7 10]	1.0e-9[.84 1.2]
ϵ_{MG} $[Wkg^{-1}]$	5.7e-9 [5.6 5.9]	3.4e-9 [3.4 3.5]	4.8e-9 [4.6 5.0]	7.0e-9 [6.6 7.2]
ϵ'_{MG} $[Wkg^{-1}]$	5.0e-9 [5.5 5.8]	3.4e-9 [3.4 3.5]	2.2e-9 [2.1 2.2]	2.3e-9 [2.3 2.4]
κ_{zGH} $[m^2s^{-1}]$	8.8e-5 [5.2 13]	1.4e-3 [1.2 1.5]	6.2e-4 [3.8 9.2]	2.6e-4 [2.1 3.3]
κ'_{zGH} $[m^2s^{-1}]$	8.4e-5 [5.2 12]	1.2e-3 [1.1 1.4]	3.1e-4 [1.2 5.4]	3.1e-5 [1.6 5.1]
κ_{zMG} $[m^2s^{-1}]$	5.0e-5 [4.7 5.5]	1.6e-4 [1.5 1.6]	1.6e-4 [1.5 1.7]	1.5e-4 [1.4 1.6]
κ'_{zMG} $[m^2s^{-1}]$	4.1e-5 [3.8 4.5]	1.5e-4 [1.4 1.5]	1.5e-5 [1.3 1.8]	6.5e-6 [5.5 8.3]
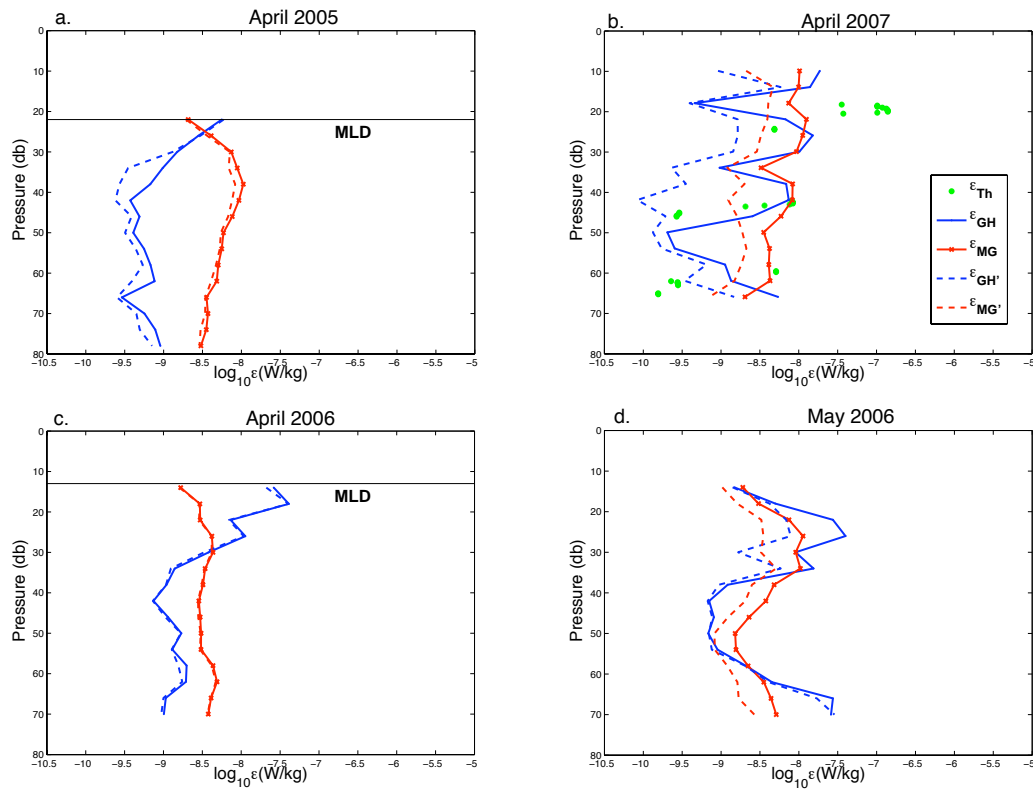
Figure 4.13 – The time-mean dissipation rates, ϵ, based on Thorpe scale approximations, ϵ_{Th}, (green), Gregg-Henyey parameterization, ϵ_{GH}, (blue), and the MacKinnon-Gregg parameterization, ϵ_{MG}, (red). The mixed layer depth (MLD) is indicated for the two time series that exhibit a mixed layer, April 2005 and April 2006. Parameterizations were not calculated above this mixed layer depth.
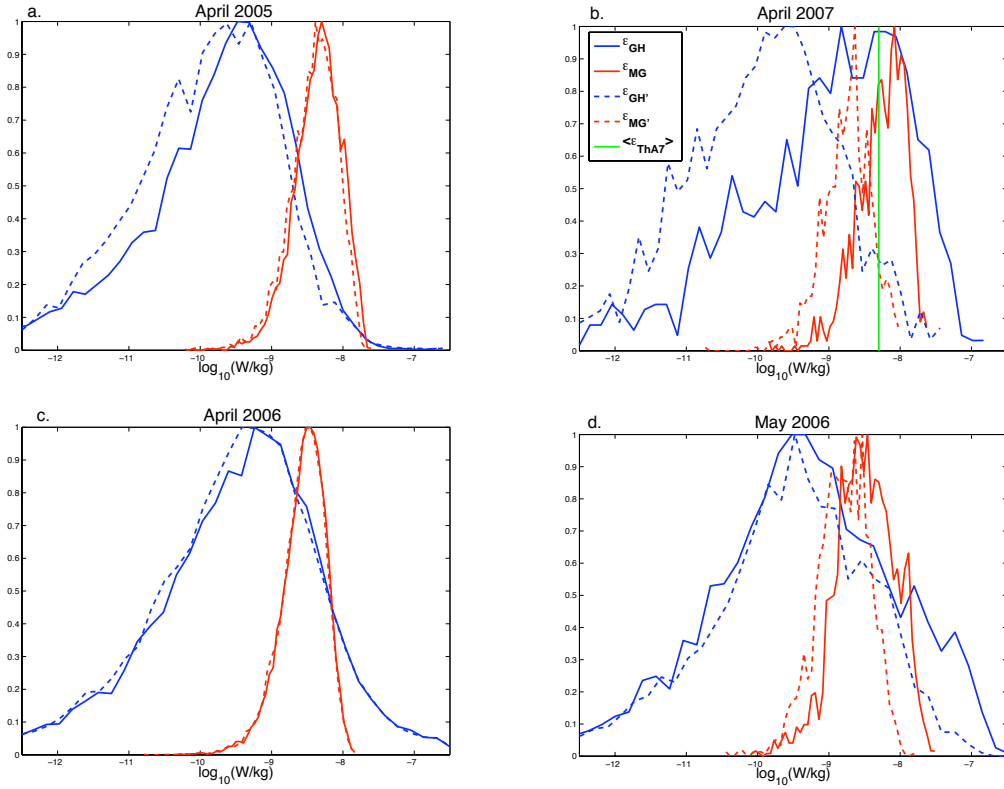
Figure 4.14 – Probability Distribution Function of $log_{10}\epsilon$, based on Thorpe scale approximations, ϵ_{Th}, (green), Gregg-Henyey parameterization, ϵ_{GH}, (blue), and the MacKinnon-Gregg parameterization, ϵ_{MG}, (red). The ϵ derived from the baroclinic perturbation velocities, ϵ'_{GH} and ϵ'_{MG}, are indicated in dashed lines of the same color, respectively.

for ϵ'_{bc}, and whose mean ϵ_{MG} drops from $7.0 \times 10^{-9} Wkg^{-1}$ to $2.3 \times 10^{-9} Wkg^{-1}$. May 2006 shows a similar drop between ϵ_{bc} and ϵ'_{bc}, with a drop in ϵ_{GH} from $1.1 \times 10^{-8} Wkg^{-1}$ to $5.6 \times 10^{-9} Wkg^{-1}$, and a drop in ϵ_{MG} from $4.8 \times 10^{-9} Wkg^{-1}$ to $2.2 \times 10^{-9} Wkg^{-1}$ (Table 4.1). In contrast, April 2005 shows a much smaller drop between ϵ_{bc} and ϵ'_{bc}, with its mean ϵ_{GH} dropping slightly from 1.2 to $1.0 \times 10^{-9} Wkg^{-1}$, and mean ϵ_{MG} from 5.7 to $5.0 \times 10^{-9} Wkg^{-1}$. This small difference corresponds to the fact that while there is a marked drop in energy from the total KE_{bc} to the total KE'_{bc} for April 2005 (see Section 4.4.3), nearly all of the time-mean KE is in mode 1, so there is little loss of shear between $\mathbf{U}_{bc}$ and $\mathbf{U}'_{bc}$. Similarly, the mean ϵ_{GH} for April 2006 drops only slightly from 6.9 to 6.3 $\times 10^{-9} Wkg^{-1}$, and the mean ϵ_{MG} of $3.4 \times 10^{-9} Wkg^{-1}$ remains practically unchanged, as can be clearly seen in Figure 4.13. The fact that these two time series show little to no change between ϵ_{bc} and ϵ'_{bc}, indicates that the shear during these two periods is due almost entirely to internal waves. Note that we have displayed the Thorpe scale estimates in Figure 4.13 as well, but the reader must not look for point-to-point comparison. We expect the Thorpe scale and the finescale parameterizations to have the same range of variation, and that the overall average values are of the same order, as they are, but we do not expect the values to be equivalent, since Thorpe scale estimates are instantaneous values, while the fine-scale parameterized values are averaged over at least twelve hours.

While the average ϵ values in Figure 4.13 allow us to compare the relative strength of the average ϵ in each time series, the probability distribution functions, as represented in Figure 4.14, allow us to compare all the data. The time series with the highest ϵ_{bc}
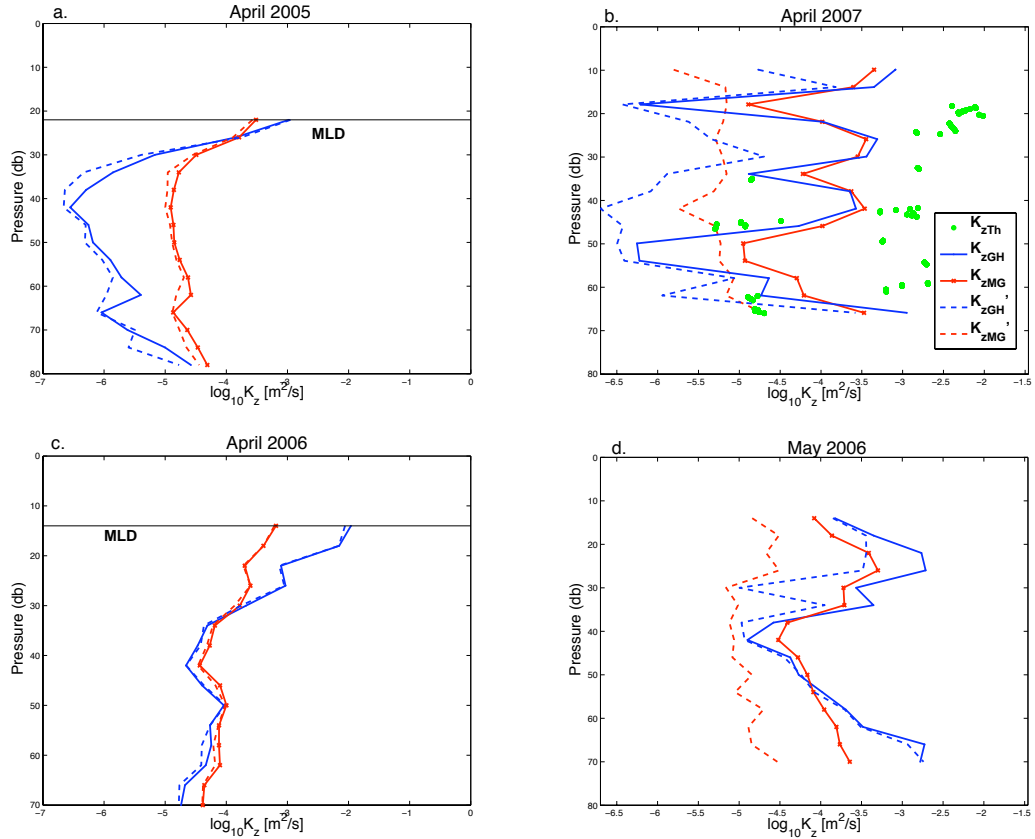
Figure 4.15 – Average diapycnal diffusivities, κ_z, based on Thorpe scale approximations, ϵ_{Th}, (green), Gregg-Henyey parameterization, ϵ_{GH}, (blue), and the MacKinnon-Gregg parameterization, ϵ_{MG}, (red). The κ_z derived from the baroclinic perturbation velocities, $\kappa_z{'}_{GH}$ and $\kappa_z{'}_{MG}$, are indicated in dashed lines of the same color, respectively.

values in Figure 4.14 is April 2007, with mode values an order of magnitude greater than the other time series. When the parameterizations are calculated solely on $\mathbf{U}'_{bc}$, however, April 2007 has the greatest shift in ϵ, indicating that most of the turbulent dissipation in this time series is due to contributions from low-frequency signals, with a period greater than 6 hours. The time series with the smallest difference between ϵ_{bc} and ϵ'_{bc} is April 2006, and in fact the mode values for both ϵ'_{MG} and ϵ'_{GH} are greater than or equal to all the other time series, indicating that while there is much less turbulent dissipation due to low-frequency signals in this time series, there is much greater dissipation due to internal waves.

To understand how these different turbulent rates of dissipation, ϵ, affect the mixing during each time series, we compare the diapycnal diffusivities, κ_z, both those due to $\mathbf{U}_{bc}$, hereinafter κ_z, and those due to $\mathbf{U}'_{bc}$, hereinafter κ'_z, as seen in Figure 4.15. The overall average κ_z for both GH and MG are 5.7×10^{-4} and 1.3×10^{-4} $m^2 s^{-1}$, respectively, dropping to 4.1×10^{-4} and 5.2×10^{-5} $m^2 s^{-1}$ for κ'_z. The relative strength of κ_z and κ'_z for each time series corresponds to their different γ values, with the greatest values occurring in April 2006 and May 2006, and the lowest values occurring in April 2007 and April 2005. The high γ values in April 2005 and April 2007 correspond to lower diapycnal diffusivities, associated with lower rates of turbulent dissipation, whereas the higher estimated mixing in April 2006 is most likely due to its low γ value, and corresponding higher rates of

turbulent dissipation during this time period.

Heat Flux

To get a better idea of the impact of turbulent mixing on the local ocean-ice heat budget, we use the diapycnal diffusivities to calculate the vertical heat flux, $Q = -\rho c_p \kappa_z \delta_z T$. The resultant local change in temperature due to this heat flux, $\delta_t T = -\frac{1}{\rho c_p} \delta_z Q$, is then evaluated. The vertical heat flux, Q, both due to κ_z, and κ'_z, for the three time series with concurrent CTD and ADCP measurements, can be seen in the top three plots of Figure 4.16. During both April 2005 and April 2006, Figure 4.16a and b, there is a net downward heat flux below the mixed layer for both $\mathbf{U}_{bc}$ and $\mathbf{U}'_{bc}$, whereas May 2006, Figure 4.16c, reveals a net upward heat flux.

The three lower plots in Figure 4.16 depict the local heating and cooling associated with these vertical heat fluxes. There is a complex pattern of both heating and cooling occurring throughout the water column for all time series, on the order of 10^{-2} $^oK/month$. The spatial pattern is similar to that of the heat flux with most of the activity occurring near the top the pycnocline for each time series. In April 2006 there is a net cooling in the first half of the time series, followed by a net heating in the second half of the time series. May 2006 reveals the opposite pattern with a net heating followed by a net cooling in the top of the water column and an associated heating in the bottom of the water column. Since our time series are too short to notice any long-term trends, however, further investigation is necessary to explore the possible effects of different stratification profiles on long-term heating or cooling in Storfjorden.

4.6 Summary and Discussion

In this isolated Arctic fjord, we have looked at hydrographic and velocity measurements from three nearly co-located stations during four time periods in three subsequent springs. While the location and seasons are similar, different environmental conditions during the four time series lead to strikingly different stratification (N^2) profiles. Even though the average N^2 is of the same order of magnitude for all time series, the shape of the profiles is remarkably distinct. This unique situation allows us to look at how changing the stratification profile impacts the velocity fields, the shear, the energy, the modal structure, and the eventual turbulent dissipation and associated diapycnal diffusivity, of this high-latitude internal wave field.

To quantify these differences in stratification profiles, we have used the Gerkema (2001) 2c-layer model, which measures how much a stratification profile resembles a two-layer fluid. Two of our time series, April 2005 and April 2007, have high Gerkema (2001) γ values and should behave similarly to a two-layer fluid. April 2006, however, whose stratification profile is nearly constant, has a very low γ value and should behave more like a fluid of constant stratification. In between these two extremes, May 2006 has an intermediate γ value, indicating characteristics of both a two-layer fluid and one of constant stratification.

These different stratification regimes impact the dynamics and energetics of the internal waves during each time series. A strong mode-1 response is clearly distinguishable in the baroclinic current, $\mathbf{U}_{bc}$, as well as the total baroclinic kinetic energy, KE_{bc}, of each time series except the low γ-value time series. When the kinetic energy is broken down into its various modes, the impact of the different stratification profiles can be clearly seen. While mode 1 is the dominant mode of KE_{bc} for all the time series, for the two high γ-value time series, approximately 90% of KE_{bc} is in mode 1, similar to that of a two-layer fluid, where all the energy is in mode 1. For the time series with the smallest γ value, just 30%
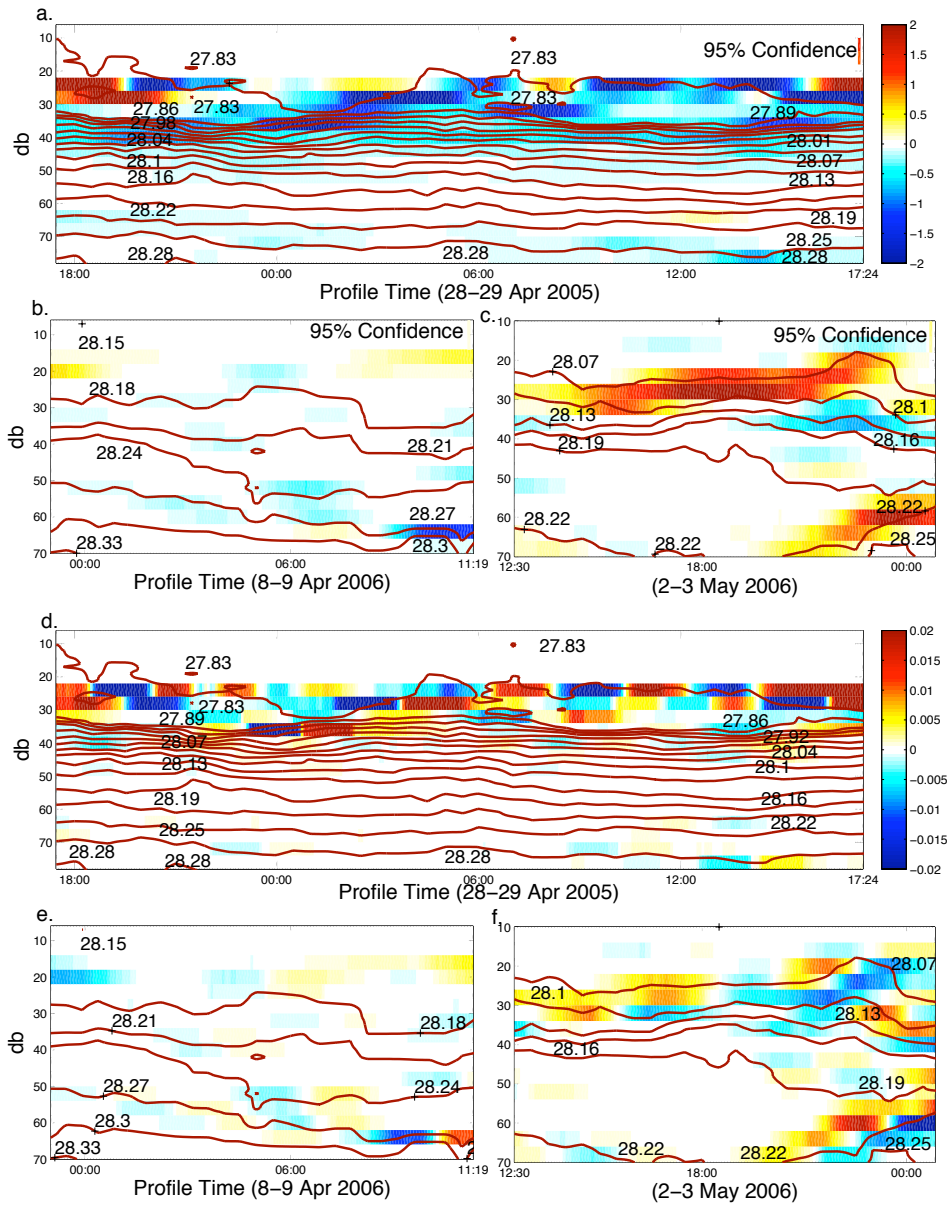
Figure 4.16 – The heat flux, $Q\ [W/m^2]$ (top three plots), and the local heating/cooling rate, $\frac{dT}{dt}[^oK/month]$ (bottom three plots), determined from diapycnal diffusivities, κ_z, based on the MacKinnon-Gregg parameterization rate of turbulent dissipation, ϵ_{MG}. Contours indicate isopycnal surfaces.

of KE_{bc} is in mode 1, similar to that of a fluid of constant stratification, where none of the energy is in mode 1, and for the intermediate γ-value time series, 50% of KE_{bc} is in mode 1, indicating that it lies on the spectrum between a two-layer fluid, and one of constant stratification. The modal distributions for KE'_{bc}, however, are more spread out over several modes for the two time series with high γ values, indicating that the modal response of these time series is not entirely similar to that of a two-layer fluid, but rather lies on the spectrum between a two-layer fluid, and one of constant stratification, falling closest to the side of a two-layer fluid.

The differences in stratification profiles not only impact the dynamics, but also the dissipation of the internal waves at each station. Estimates of the rate of turbulent dissipation (ϵ) were obtained from the Gregg-Henyey (GH) and MacKinnon-Gregg (MG) fine-scale parameterizations, scaled by measured Thorpe-scale overturns (Th). The different parameterizations all yield similar estimates, with an overall average ϵ of $5 - 6 \times 10^{-9} W kg^{-1}$. These values, obtained during ice-covered conditions, are an order of magnitude below microstructure and fine-scale approximations obtained during a period of open water in Storfjorden (Fer, 2006). The relative rate of turbulent dissipation predicted by GH, ϵ_{GH}, varies considerably among the time series in relation to their γ value (Table 4.1). GH predicts much lower turbulent dissipation for the high-γ value time series April 2005, while the highest ϵ_{GH} is seen during the low γ value time series, April 2006. When we look at just the ϵ'_{bc} predicted by GH, the estimates for ϵ_{GH} are consistent with the γ values for the various time series. The two high γ-value time series have the lowest estimated ϵ_{GH}, followed by the intermediate γ-value time series, and the highest estimated ϵ_{GH} occurrs during the low γ-value time series.

The most direct association with the stratification profiles is with the diapycnal diffusivities, or mixing, of the different time series. The two high γ-value time series have the lowest diapycnal diffusivities (κ_z), and the highest diapycnal diffusivities are seen during the period with the low γ-value time series. The intermediate γ-value time series has intermediate mixing values. Mixing due to internal waves at high latitudes is evidently strongly associated with the structure of N^2 profiles. Note that, since the internal wave signal is the dominant signal in our data, we have focused on mixing due to internal waves. There is, however, also a strong subinertial signal, particularly during the higher-γ value time series (see Figure 4.7). While our data set does not allow us to determine the source of this energy, possible sources include surface water run-off induced estuarine circulation, wind forcing, and convection due to brine rejection.

Differences in the estimated heat flux and the associated local heating and cooling do not, however, correspond to differences in stratification profiles. While the heat flux is calculated from the diapycnal diffusivities, it is strongly dependent on the temperature gradient. Since the stratification in Storfjorden is mostly controlled by the salinity, and not the temperature, there is no direct relation between the stratification profiles and the temperature gradients, and thus no direct relation between the turbulent dissipation rate and the turbulent heat flux. In fact, the greatest heat flux occurs during one of the high γ-value time series, and the lowest heat flux occurs during the low γ-value time series, the inverse of what we would expect were the turbulent dissipation rate and the turbulent heat flux directly related.

When averaged over a whole number of inertial periods, the maximum net heat flux intensities resulting from internal wave-induced mixing were found at the tops of the pycnoclines and typically reached $1 W m^{-2}$ in the intermediate γ-value time series, and $-1 W m^{-2}$ in the high γ-value time series, which is about two orders of magnitude smaller than typical heat flux at the air-sea interface of open polynyas, but still comparable to typical heat flux during ice-covered conditions (McPhee et al., 2013). Note that these weak heat fluxes could help explain the persistence of supercooled water several days after its

formation in strongly mixed conditions, as observed by Jardon et al. (2014) and McPhee et al. (2013).

Based on our results, we can infer that the shape of the stratification profile is a controlling factor on the dynamics and dissipation of internal waves. While the magnitude of the average stratification may remain relatively unchanged, the shape and characteristics of the stratification profile can vary rapidly in the Arctic. The more closely an N^2 profile resembles that of a two-layer fluid, as defined by its γ value, the more it is dominated by a mode-1 response. High γ-value time series have more energy in mode 1 of the baroclinic time mean currents, and thus less energy in the higher modes of $\mathbf{U}'_{bc}$. With less energy in the higher modes, these high γ-value time series have lower rates of turbulent dissipation, and lower diapycnal diffusivities. The more closely an N^2 profile resembles that of a fluid of constant stratification, however, the more it is dominated by higher modes and vertical propagation. These low γ-value time series have less energy in the baroclinic time-mean current, and more energy in the higher modes of $\mathbf{U}'_{bc}$. Since more of the energy is found in the higher modes, low γ-value regimes have higher rates of turbulent dissipation, and higher diapycnal diffusivities.

This effect could play an important role in how circulation models parameterize mixing. Since models do not resolve the higher modes, they rely on the assumption that more energy leads to proportionately higher diapycnal diffusivities. This is in fact the opposite of what we have found in Storfjorden. During periods with high γ-value stratification profiles, more of the energy goes into mode 1, than goes into the higher modes, which are responsible for most of the turbulent diffusivity. There will therefore be less mixing than expected based on the energy level. During periods with low γ-value stratification profiles, the energy is more evenly distributed over the different vertical modes, including in the higher modes, resulting in greater mixing than expected based on the energy level. A parameterization that only considers the magnitude of the stratification, will thus tend to overestimate mixing in periods of high γ values, and underestimate it in periods of low γ values. When considering the impact of stratification on high latitude mixing, the magnitude should not be used alone, but rather should be considered in conjunction with the structure of the stratification profile.

Acknowledgments

Chapter 5

Conclusion

Summary and Discussion

Internal waves play a key role in the global climate system. They are the conduits between large-scale winds and tides and the micro-scale turbulence that is necessary to maintain the abyssal stratification and the global overturning circulation. Internal waves are ubiquitous in all ocean basins, but their properties vary greatly from one region to another. These differences make it difficult to find a universal parameterization that encompasses all aspects of internal wave dynamics. This thesis attempts to make a dent in the gargantuan task of parameterizing internal wave dynamics. We analyzed internal waves in two distinct ocean basins, the Indian and Arctic Oceans, to understand how the different environmental conditions affect the life cycle of the internal waves. These two distinct ocean basins provide an interesting insight into how environmental conditions impact the propagation and dissipation of internal waves, and give some insight into how the ocean mixes in different regions around the world.

To understand how different environmental conditions impact the internal wave field in these two ocean basins, we have analyzed velocity and hydrographic data from both a wide, shallow Arctic fjord, as well as from a mid-ocean ridge in the Indian Ocean. In both regions, we have analyzed the internal wave field, and isolated its various frequency components to look more specifically at the internal tide and near-inertial waves. To understand the impact of environmental conditions on the lifecycle of internal waves in both regions, we have analyzed the impacts of the stratification and the mesoscale phenomena, along with region-specific environmental factors such as ice cover in the Arctic fjord, and rough topography in the Indian Ocean, on the propagation of the internal waves.

In the Indian Ocean, our study area encompassed a region of rough topography, where previous studies used finescale parameterizations to estimate mixing as being orders of magnitude above the surroundings, and extending all the way to the surface (Kunze et al., 2006). In this region of rough topography, we found a strong internal tide, characterized by a high-mode vertical structure with energy concentrated at various depths of the water column. Since this elevated turbulent mixing occurs above a mid-ocean ridge in an area of rough corrugated topography, it was presumed to be due to this strong internal tide. While the internal tide is indeed the dominant signal in the velocity spectrum, the inertial signal in fact dominated in the shear spectra. Not only is the shear dominated by the inertial signal, but the small-scale shear, which is responsible for the turbulent mixing, is strongly inertial. While the strong internal tide does indeed contribute to the turbulent mixing, the near-inertial waves are in fact the most important contributors to the turbulent mixing in the region.

On the other side of the globe, in the Arctic Ocean, our study took place inside a large, shallow Arctic fjord, Storfjorden, in the Svalbard archipelago. In this Arctic region,
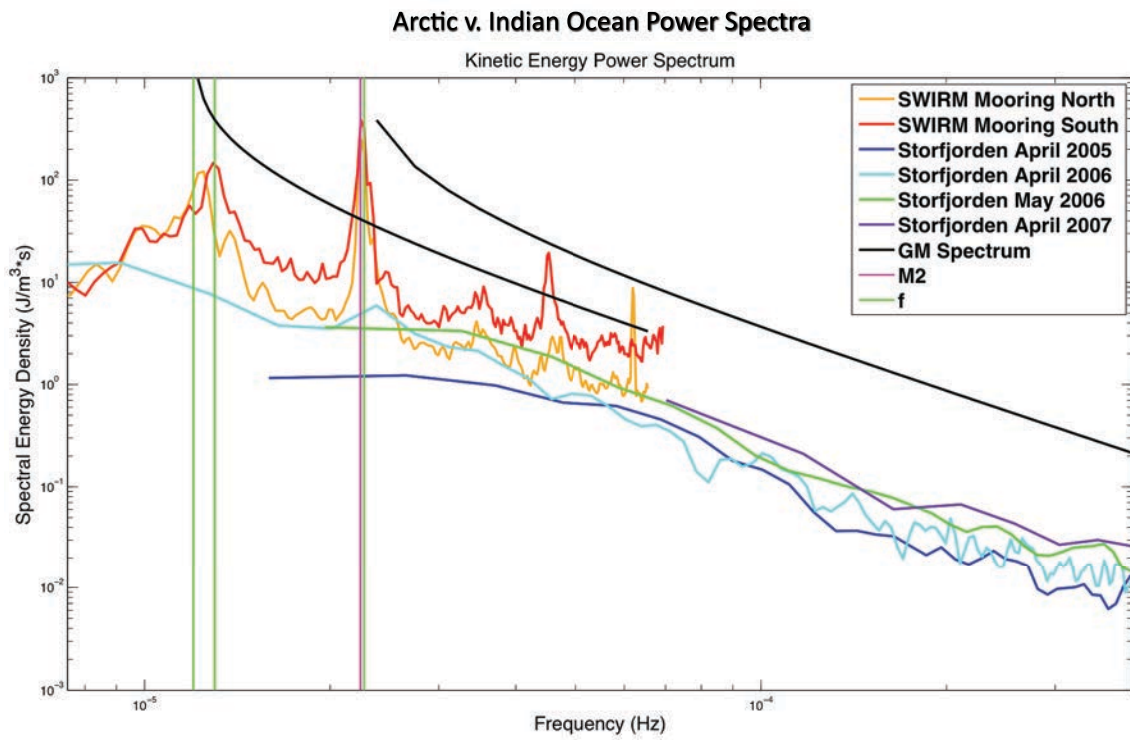
Figure 5.1 – The kinetic energy power spectra of our Arctic and Indian Ocean velocity time series.

ice cover reduces the wind forcing and also, due to its rough underside, creates a turbulent boundary layer that increases dissipation, leading to significantly lower internal wave energy, as compared to lower latitudes (Levine et al., 1985; Levine, 1990). A comparison between the kinetic energy power spectra of the Arctic time series and the kinetic energy power spectra of the Indian Ocean time series reveals that the integrated energy in the Arctic Ocean velocity data is significantly lower than that of the Indian Ocean, as can be seen in Figure 5.1. Another important distinction between the high-latitude Arctic internal wave field and that of the lower-latitude Indian Ocean is the difference in separation between the inertial (f) frequencies and the semidiurnal frequencies in the high-latitude internal wave spectra versus those of the lower-latitudes, which can be seen in Figure 5.1. In the lower latitude Indian internal wave field, there is a clear separation between the inertial frequency (f) peak, and that of the semidiurnal tide. For the high-latitude Arctic internal wave field, on the other hand, the two frequencies are almost indistinguishable. In fact, at the high latitudes of our Arctic study, the main M_2 semidiurnal tide is subinertial and, under linear theory, cannot propagate under the traditional $\beta-plane$ approximation, where the horizontal component of the Coriolis force is neglected, but rather is evanescent.

The propagation of internal waves in the Arctic and Indian Ocean basins was measured in terms of the energy flux, which indicates the direction and magnitude of the internal waves. In the rough topography region of the Indian Ocean, the energy flux of the internal tide reveals dramatic spatial and temporal variability, consistent with changes in the mesoscale. Figures 5.2 and 5.3 show the time- and depth-mean energy flux for the Arctic and Indian Ocean time series respectively. The energy flux vectors are plotted over the theoretical internal tide generation sites based on Baines (1982). Since the M_2 semidiurnal internal tide is evanescent in the Arctic study region, we expect that the semidiurnal energy flux is due to the S_2 internal tide and the locally-generated M_2 internal tide.

The red boxes in Figure 5.2 indicate the probable local generation sites for the semidiurnal internal tide in the Arctic time series, including the minor ridge-like feature just to the northeast of the station, and the rough topography due south of the station. The energy is predominantly propagating towards the shoreline, where the internal waves will most likely shoal and break, dissipating the energy locally.

The theoretical generation sites in the Indian Ocean similarly occur predominantly along the ridges and sharp topographic features. In the Indian Ocean, we have used ray tracing to find the specific sites of generation of the tidal beams observed at our moorings, and compared those with the theoretical sites of generation. In this region of rough topography, where reflection and scattering of waves can lead to wave interference, we remarkably found multiple sites where the observed ray paths intersected the topography in the same location as those predicted by theory. These sites where the theory lined-up with the observations occurred where the slope of the topography was greater than .65 the slope of the M_2 tide. When the slope of the topography was less than .65 the slope of the internal tide, the theory and the observations did not match up, which is presumed to be due to reflection off the rough topography and subsequent interference of the internal tide, as well as interaction with the mesoscale.

While the propagation of the internal tide item Indian Ocean varies with changes in the mesoscale field, the propagation of internal waves in the Arctic is highly dependent on changes in the stratification. Our research finds that the rapidly changing shape and characteristics of the stratification profile is a controlling factor on the propagation and dissipation of high latitude internal waves. The highly variable structure of the Arctic stratification is evident, as our four day-long time series from similar times of year in nearly the same location in Storfjorden change drastically from one to the other (Figure 4.3), while the month-long time series from the Indian Ocean show little to no temporal variability (Figure 2.16). Our research shows that this rapidly changing stratification
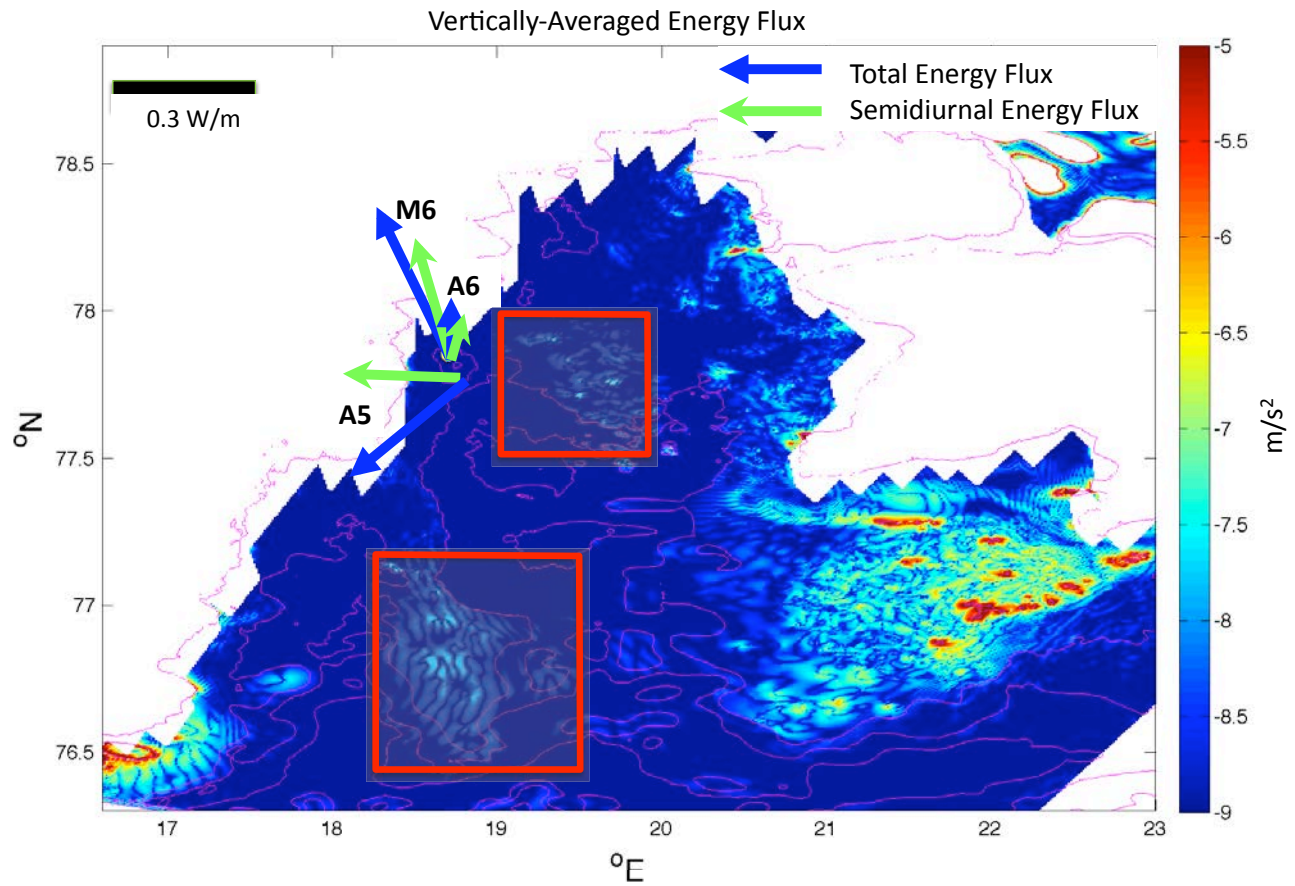
Figure 5.2 – The vertically-integrated energy flux averaged over the length of each CTD time series respectively, is shown emanating from the respective stations. The scale is shown in the upper left-hand corner. The background colors represent the theoretical sites of barotropic to baroclinic conversion of the M_2 tide in m/s^2, plotted over the background topography. Red boxes indicate areas of likely local generation.
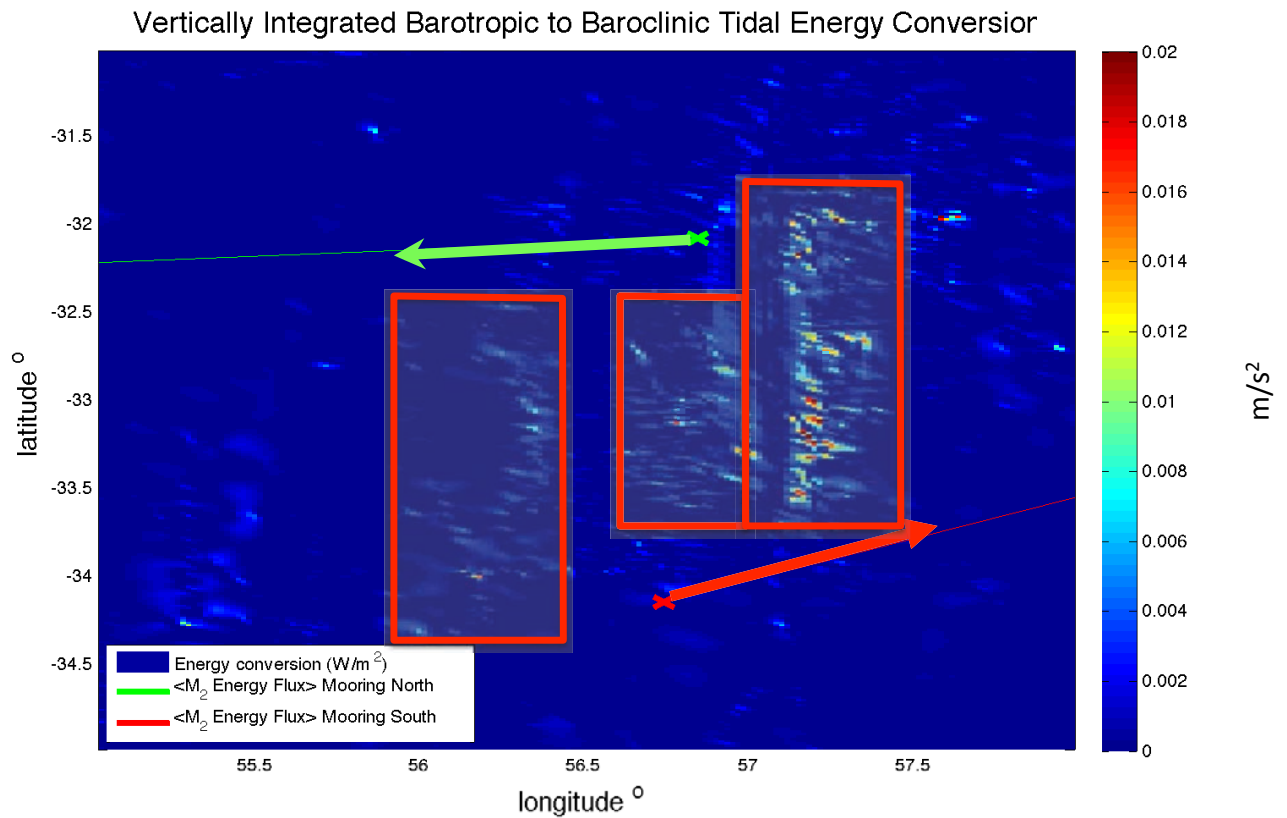
Figure 5.3 – The depth- and time-mean vertically-integrated energy flux averaged over the length of each CTD time series respectively, is shown emanating from the respective stations. The background colors represent the theoretical sites of barotropic to baroclinic conversion of the M_2 tide in m/s^2.

structure in the Arctic data is responsible for changes in the vertical structure of high latitude internal waves. To quantify the differences in the stratification profiles among the time series, a classification of the stratification was made using the simple γ criterion from Gerkema (2001), originally proposed by Baines (1982). γ is the ratio of the phase speed of a wave in a two-layer fluid to that of a wave in a fluid of constant stratification. This parameter serves as an indicator for the modal response of the internal wave field, with higher values indicating a strongly mode-1 response, and lower values, that of higher vertical modes. Since higher vertical modes generate higher shear and enhanced dissipation and mixing, γ also reflects the intensity of the mixing. Thus, in order for general circulation models (GCM's) to correctly parameterize the mixing, they must take into account the vertical structure of the stratification profiles. GCM's must, therefore, be of sufficient spatial resolution to resolve the stratification profiles, as well as the higher modes which are most responsible for the mixing.

Persepectives and Future Work

This thesis finds that environmental factors such as mesoscale activity in the Indian Ocean and stratification in the Arctic, dramatically impact the lifecycle of internal waves. In order for GCM's to properly parameterize internal wave dynamics, their dissipation, and resulting turbulent mixing, they must take into account the impacts of these outside forcings.

To more thoroughly understand the effects of the mesoscale on the internal tide above the Southwest Indian Ridge, a ray-tracing model that takes into account the impacts of the mesoscale on the ray path of the internal tide will be employed. This will enable us to not only understand the effects of the mesoscale on the propagation of the internal tide, but also to test the $.65\alpha$ criterion we found for when the observed and theoretical sites of generation align. If future work confirms this criterion, tidal generation models could use it to more accurately pinpoint sites of internal tide generation based on bottom slope.

Future work in the Arctic entails comparison of simultaneous direct microstructure measurements with different finescale parameterizations in Storfjorden to evaluate the effectiveness of the various parameterizations at estimating the turbulent mixing. We will also evaluate the representation of internal waves in a high resolution regional model (C. Rousset), by testing the numerical resolution against long-term (2-year) velocity measurements recently retrieved from Storfjorden. This will allow us to determine how well the vertical and frequency spectra of the internal waves are resolved in the model, and possibly to adapt existing parameterizations to the actual resolution of the model. The model will also be used to test the γ criteria as an indicator of the vertical mode response and its effect on the turbulent mixing in the model.

Another question in the Arctic is how the internal M_2 semidiurnal tide propagates above the critical latitude when the traditional approximation is not made. Theroretical work by Gerkema shows that propagation of the subinertial tide is possible in the less-stratified part of the water column. This theoretical result will be tested in high-resolution idealized (2D) numerical models.

List of Figures

List of Tables

Bibliography

Alford, M. H. (2003a). Energy available for ocean mixing redistributed though long-range propagation of internal waves. *Nature*, *423*, 159–163.

Alford, M. H. (2003b). Improved global maps and 54-year history of wind-work on ocean inertial motions. *Geophysical Research Letters*, *30*, doi: 10.1029/2002GL016614.

Baines, P. (1982). On internal tide generation models. *Deep-Sea Res.*, *29*, 307–338.

Baines, P. (1986). Internal tides, internal waves and near-inertial motions. *Baroclinic Processes on Continental Shelves, Coastal and Estuarine Sciences*, *3*, 19–31.

CNES (2014). Aviso. URL: `http://www.aviso.oceanobs.com/`.

Cole, S. T., Rudnick, D. L., & Hodges, B. A. (2009). Observations of tidal internal wave beams at Kauai Channel, Hawaii. *J. Phys. Oceanogr.*, *39*, 421–436.

D'Asaro, E. (1985). The energy flux from the wind to near-inertial motions in the mixed layer. *J. Phys. Oceanogr.*, *15*, 943–959.

D'Asaro, E. (1995). A collection of papers on the ocean storms experiment. *J. Phys. Oceanogr.*, *25*, 2817–2818.

Defant, A. (1961). *Physical Oceanography*. New York: Pergamon Press.

Dillon, T. M. (1982). Vertical overturns: A comparison of Thorpe and Ozmidov length scales. *J. Geophys. Res.*, *87*, 9601–9613.

Dovgaya, S., & Cherkesov, L. (1996). Thermohydrodynamics of the ocean. *Phys. Oceanogr.*, *7*, 3–9.

ECMWF (2014). European centre for medium-range weather forecasts ecmwf era-40 re-analysis data. URL: `http://badc.nerc.ac.uk/view/badc.nerc.ac.uk__ATOM_ _dataent_ECMWF-E40`.

Egbert, G. D., Bennett, A., & Foreman, M. (1994). Topex/poseidon tides estimated using a global inverse model. *J. Geophys. Res.*, *99*, 24,821 – 24, 852.

Fer, I. (2006). Scaling turbulent dissipation in an arctic fjord. *Deep-Sea Res II*, *53*, 77–95.

Fer, I., & Drinkwater, K. (2014). Mixing in the Barents Sea Polar Front near Hopen in spring. *Journal of Marine Systems*, *130*, 206–218.

Fer, I., Skogseth, R., & Geyer, F. (2010). Internal waves and mixing in the marginal ice zone near the yermak plateau. *J. Phys. Oceanogr.*, *40*, 1613–1630.

Fer, I., Skogseth, R., & Haugan, P. M. (2004). Mixing of the storfjorden overflow (svalbard archipelago) inferred from density overturns. *J. Geophys. Res.*, *109*.

Fer, I., Skogseth, R., Haugan, P. M., & Jaccard, P. (2003). Observations of the Storfjorden overflow. *Deep-Sea Res. I*, *50*, 1283–1303, doi: 10.1016/S0967–0637(03)00124–9.

Ferron, B., Mercier, H., Speer, K., Gargett, A., & Polzin, K. (1998). Mixing in the Romanche Fracture Zone. *J. Phys. Oceanogr.*, *28*, 1929–1945.

Furuichi, N., Hibiya, T., & Niwa, Y. (2008). Model predicted distribution of wind-induced internal wave energy in the world's oceans. *J. Geophys. Res.*, *submitted*.

Garrett, C., & Munk, W. (1972). Space-time scales of internal waves. *Geophys. Fluid Dyn.*, *2*, 225–264.

Garrett, C., & Munk, W. (1979). Internal waves in the ocean. *Ann. Rev. Fluid Mech.*, *11*, 339–369.

Garrett, C. J. R., & Munk, W. H. (1975). Space-time scales of internal waves: A progress report. *J. Geophys. Res.*, *80*, 291–297.

Gerkema, T. (2001). Internal and interfacial tides: Beam scattering and local generation of solitary waves. *J. Mar. Res.*, *59*, 227–255.

Gerkema, T., & van Haren, H. (2007). Internal tides and energy fluxes over great meteor seamount. *Ocean Sci.*, *3*, 441–449.

Gerkema, T., & Shrira, V. I. (2005a). Near-inertial waves in the ocean: beyong the 'traditional approximation'. *J. Fluid Mech.*, *529*, 195–219, doi:10.1017/S0022112005003411.

Gerkema, T., & Shrira, V. I. (2005b). Near-inertial waves on the "nontraditional" β plane. *J. Geophys. Res.*, *110*, doi:10.1029/2004JC002519.

Gill, A. E. (1982). *Atmosphere-Ocean Dynamics*. Academic.

Gregg, M. (1989). Scaling turbulent dissipation in the thermocline. *J. Geophys. Res.*, *94*, 9686–9698.

Gregg, M. C., Sanford, T. B., & Winkel, D. P. (2003). Reduced mixing from the breaking of internal waves in equatorial waters. *Nature*, *422*, 513–515.

Guthrie, J. D., Morrison, J. H., & Fer, I. (2013). Revisiting internal waves and mixing in the arctic ocean. *J. Geophys. Res.*, *118*, 1–12.

Henyey, F. S., Wright, J., & Flatté, S. M. (1986). Energy and action flow through the internal wave field. *J. Geophys. Res.*, *91*, 8487–8495.

Jardon, F., Bouruet-Aubertot, P., Cuypers, Y., Vivier, F., & Laurenço, A. (2011). Internal waves and vertical mixing in the storfjorden polynya, svalbard. *J. Geophys. Res.*, *116*, doi:10.1029/2010JC006918.

Jardon, F., Vivier, F., Bouruet-Aubertot, P., Laurenço, A., Cuypers, Y., & Willmes, S. (2014). Ice production in Storfjorden (Svalbard) estimated from a model based on AMSR-E observations: impact on water masses properties. *J. Geophys. Res.*, *119*, 377–393, doi:10.1002/2013JC009322.

Jayne, S., & St. Laurent, L. C. (2001). Parameterizing tidal dissipation over rough topography. *Geophys. Res. Lett.*, *28*, 811–814.

Jeffreys, H. (1925). On fluid motions produced by differences of temperature and humidity. *Quart. J. Roy. Meteor. Soc.*, *51*, 347–356.

Jiang, J., Lu, Y., & Perrie, W. (2005). Estimating the energy flux from the wind to ocean inertial motions: The sensitivity to surface wind fields. *Geophys. Res. Lett.*, *32*, doi:10.1029/2005GL023289.

Kalnay (1996). The NCEP/NCAR 40-year reanalysis project. *Bulletin of the American Meteorological Society*, *77*, 437–470.

Klymak, J. (2012). The garrett and munk internal wave spectra matlab toolbox. URL: `http://hornby.seos.uvic.ca/~jklymak/GarrettMunkMatlab/`.

Klymak, J. M., Pinkel, R., & Rainville, L. (2008). Direct breaking of the internal tide near topography: Kaena Ridge, Hawaii. *J. Phys. Oceanogr.*, *38*, 380–399.

Kuhlbrodt, T., Griesel, A., Montoya, M., Levermann, A., Hofmann, M., & Rahmstorf, S. (2007). On the driving processes of the atlantic meridional overturning circulation. *Rev. Geophys*, *45*, doi:10.1029/2004RG000166.

Kundu, P. K. (1990). *Fluid Mechanics*. Academic Press.

Kunze, E., Firing, E., Hummon, J. M., Chereskin, T. K., & Thurnherr, A. M. (2006). Global abyssal mixing inferred from lowered ADCP shear and CTD strain profiles. *J. Phys. Oceanogr.*, *36*, 1553–1576.

Levine, M. D. (1990). Internal waves under the arctic pack ice during the arctic internal wave experiment: The coherence structure. *J. Geophys. Res.*, *95*, 7347–7357.

Levine, M. D., Paulson, C. A., & Morison, J. H. (1985). Internal waves in the arctic ocean: Comparison with lower-latitude observations. *J. Phys. Ocean.*, *15*, 800–809.

Loeng, H. (1991). Features of the physical oceanographic conditions of the barents sea. *Polar Research*, *10*, 5:18.

MacKinnon, J., & Gregg, M. (2003). Mixing on the late-summer New England shelf − solibores, shear and stratification. *JPO*, *33*, 1476–1492.

MacKinnon, J., & Gregg, M. (2005). Spring mixing: tubulence and internal waves during restratification on the New England shelf. *J. Phys. Oceanogr.*, *35*, 2425–2443.

McPhee, M. G., Skogseth, R., Nilsen, F., & Smedsrud, L. H. (2013). Creation and tidal advection of a cold salinity front in storfjorden: 2. supercooling induced by turbulent mixing of cold water. *J. Geophys. Res.*, *118*, 3737–3751, doi:10.1002/jgrc.20261.

Melet, A., Nikurashin, M., Muller, C., Falahat, S., Nycander, J., Timko, P. G., Arbic, B. K., & Goff, J. A. (2013). Internal tide generation by abyssal hills using analytical theory. *J. Geophys. Res.*, *118*, 6303–6318 doi:10.1002/2013JC009212.

Mercier, M. J., Mathur, M., Gostiaux, L., Gerkema, T., Magalhães, J. M., Silva, J. C. D., & Dauxois, T. (2012). Soliton generation by internal tidal beams impinging on a pycnocline: laboratory experiments. *J. Fluid Mech.*, *704*, 37–60.

Merrifield, M. A., & Holloway, P. E. (2002). Model estimates of M_2 internal tide energetics at the Hawaiian Ridge. *J. Geophys. Res.*, *107*.

Morrison, A., Billings, J., & Doherty, K. (2000). The mclane moored profiler: An autonomous platform for oceanographic measurements. (pp. 353–358). MTS/IEE/OES Proceedings of OCEANS volume I.

Munk, W., & Wunsch, C. (1998). Abyssal recipes II: Energetics of tidal and wind mixing. *Deep-Sea Res. Part I*, *45*, 1977–2010.

Munk, W. H. (1981). Internal waves and small-scale processes. In B. A. Warren, & C. Wunsch (Eds.), *Evolution of Physical Oceanography* (pp. 264–291). Cambridge, MA: MIT Press.

Nash, J. D., Alford, M. H., & Kunze, E. (2005). Estimating internal-wave energy fluxes in the ocean. *J. Atmos. Ocean. Tech.*, *22*, 1551–1570.

Nash, J. D., Kunze, E., Lee, C. M., & Sanford, T. B. (2006). Structure of the baroclinic tide generated at Kaena Ridge, Hawaii. *J. Phys. Oceanogr.*, *36*, 1123–1135.

Nycander, J. (2005). Generation of internal waves in the deep ocean by tides. *J. Geophys. Res.*, *110*, doi:10.1029/2004JC002487.

Osborn, T. R. (1980). Estimates of the local rate of vertical diffusion from dissipation measurements. *J. Phys. Oceanogr.*, *10*, 83–89.

Padman, L., & Erofeeva, L. (2004). A barortropic inverse tidal model for the arctic ocean. *Geophys. Res. Lett.*, *31(2)*, doi:10.1029/2003GL019003.

PolarView (2012). Polar view – european arctic node. URL: `http://polarview.met.no/`.

Polzin, K., Toole, J., Ledwell, J., & Schmitt, R. (1997). Spatial variability of turbulent mixing in the abyssal ocean. *Science*, *276*, 93–96.

Quadfasel, D., Rudels, B., & Kurz, K. (1988). Outflow of dense water from a svalbard fjord into the fram straight. *Deep-Sea Res.*, *35*, 1143–1150.

Rainville, L., & Pinkel, R. (2006). Propagation of low-mode internal waves through the ocean. *J. Phys. Oceanogr.*, *36*, 1220–1236. Submitted.

Rudnick, D., Boyd, T., Brainerd, R., Carter, G., Egbert, G., Gregg, M., Holloway, P., Klymak, J., Kunze, E., Lee, C., Levine, M., Luther, D., Martin, J., Merrifield, M., Moum, J., Nash, J., Pinkel, R., Rainville, L., & Sanford, T. (2003). From tides to mixing along the Hawaiian Ridge. *Science*, *301*, 355–357.

Sandstrom, J. W. (1908). Dynamische versuche mit meerwasser. *Annals in Hydrodynamis Marine Meteorology*, (p. 6).

Schauer, U. (1995). The release of brine-enriched shelf water from Storfjord into the Norwegian sea. *J. Geophys. Res.*, *100*.

Shih, L., Koseff, J., Ivey, G. N., & Ferziger, J. H. (2005). Parameterization of turbulent fluxes and scales using homogeneous sheared stably statified turbulence simulations. *J. Fluid Mech.*, *525*, 193–214.

Simmons, H. L., Hallberg, R. W., & Arbic, B. K. (2004). Internal wave generation in a global baroclinic tide model. *Deep-Sea Res II*, *51*, 3043–3068.

Skogseth, R., Haugan, P., , & Jakobsson, M. (2005). Watermass transformations in Storfjorden. *Continental Shelf Research*, *25*, 667–695.

Skogseth, R., McPhee, M. G., Nilsen, F., & Smedsrud, L. H. (2013). Creation and tidal advection of a cold salinity front in Storfjorden: 1. Polynya dynamics. *J. Geophys. Res.*, *118*, 1–14, doi: 10.1002/jgrc.20231.

Smith, W. H. F., & Sandwell, D. T. (1997). Global seafloor topography from satellite altimetry and ship depth soundings. *Science*, *277*, 1957–1962.

Sundfjord, A., Fer, I., Kasajima, Y., & Svendsen, H. (2007). Observations of turbulent mixing and hydrography in the marginal ice zone of the barents sea. *J. Geophys. Res.*, *112*.

Thorpe, S. (1977). Turbulence and mixing in a Scottish Loch. *Philos. Trans. R. Soc. London Ser. A*, *286*, 125–181.

Thorpe, S. A. (2005). *The Turbulent Ocean*. Cambridge Univ. Press.

Thurnherr, A. M., Richards, K. J., German, C. R., Lane-Serff, G. F., & Speer, K. (2002). Flow and mixing in the rift valley of the Mid-Atlantic Ridge. *J. Phys. Oceanogr.*, *32*, 1763–1778.

Vlasenko, V., Stashchuk, N., Hutter, K., & Sabinin, K. (2003). Nonlinear internal waves forced by tides near the critical latitude. *Deep-Sea Res. I*, *50*, 317–338.

Watanabe, M., & Hibiya, T. (2002). Global estimates of the wind-induced energy flux to inertial motions in the surface mixed layer. *Geophys. Res. Lett.*, *29*, 10.1029/2001GL014422.

Waterhouse, A. F., MacKinnon, J. A., Nash, J. D., Alford, M. H., Kunze, E., Simmons, H. L., Polzin, K. L., St. Laurent, L. C., Sun, O. M., Pinkel, R., Talley, L. D., Whalen, C. B., Huussen, T. N., Carter, G. S., Fer, I., Waterman, S., Garabato, A. C. N., Sanford, T. B., & Lee, C. M. (2014). Global patterns of diapycnal mixing from measurements of the turbulent dissipation rate. *J. Phys. Oceanogr.*, *44*, 1854–1872.

Whalen, C. B., Talley, L. D., & MacKinnon, J. A. (2012). Spatial and temporal variability of global ocean mixing inferred from Argo profiles. *Nature Geosciences*, *submitted*.

Winters, K. B., Bouruet-Aubertot, P., & Gerkema, T. (2011). Critical reflection and abyssal trapping of near-inertial waves on a β plane. *J. Fluid Mech.*, *684*, 111–136, doi: 10.1017/jfm.2011.280.

Wunsch, C., & Ferrari, R. (2004). Vertical mixing, energy and the general circulation of the oceans. *Ann. Rev. Fluid Mech.*, *36*, 281–412.

Zilberman, N., Becker, J., Merrifield, M., & Carter, G. (2009). Model estimates of M_2 internal tide generation over mid-atlantic ridge topography. *J. Phys. Oceanogr.*, *39*, 2635–2651.